An Experiment to Search for Galactic Axions

by

Walter Wuensch

Submitted in Partial Fulfillment of the

Requirements of the Degree of

DOCTOR OF PHILOSOPHY

Supervised by Professor A. C. Melissinos

Department of Physics and Astronomy

University of Rochester

Rochester, New York

1988

Abstract

Results are presented from a search for axions in the mass range of $.51 \times 10^{-5}$ to 1×10^{-5} eV, which may make up the dark matter halo of our galaxy. The detector used in the search consists of a microwave cavity placed in the strong magnetic field of a superconducting solenoid magnet. The energy in the TM_{010} mode of the cavity is monitored by a sensitive microwave receiver as the frequency of the mode is swept. The predicted experimental signature of galactic halo axions is a narrow signal, with a $Q_a - f/\Delta f \approx 3 \times 10^6$, which is expected when the resonant frequency of the cavity corresponds to the mass of the axion. An experimental limit on the coupling times the density of $(g_{a\gamma\gamma}/m_a)^2 \rho_a \leq 2 \times 10^{-40}$ for an axion linewidth ≤ 400 Hz with a 97% confidence level has been obtained. The theoretical prediction is $(g_{a\gamma\gamma}/m_a)^2 \rho_a \approx 3.9 \times 10^{-44}$ with $\rho_a - 300$ MeV/cm^3. The corresponding limit in $g_{a\gamma\gamma}$ is $g_{a\gamma\gamma} \leq 7 \times 10^{-14}$ GeV^{-1} at an axion frequency $f - 2$ GeV and depends linearly on axion mass.

Acknowledgments

I would like to express my sincere thanks to everyone who has made this experiment so entertaining; Charlie Anderson, Audrey Blake, Pat Borelli, Jim Briggs, Ernie Buchanan, David Cattaneo, Betty Cook, Frank Cullen, Bill De Jong, Norman Franklin, George Ganetis, Henry Halama*, Ron Hauser, Harold Hicks, Herb Hildebrand, Richard Hogue, Connie Jones, Dave Kipp, Judy Mack, John Mazzeo, Bruce Moskowitz*, Frank Nezrick*, Gary Nitzel, Ron Picinich, Al Prodell*, Paul Ribaudo, The Riggers, Joe Rogers*, Ritchie Savoy, Carl Schultheiss, Yanis Semertzidis*, John Sheedy, John Skaritka, Dan Wilson, Susanna De Panfilis Wuensch*, and my advisor Professor Adrian Melissinos*.

* denotes people who bear particular responsibility.

Curriculum Vitae

Walter Wuensch was born on July 24, 1961. He attended the California Institute of Technology from 1979 to 1983, where received a Bachelor of Science degree in Physics. In 1983 he began graduate studies at the University of Rochester. His research work has included Fermilab experiment 723, a search for anomalous forces at highly relativistic velocities, from the fall of 1983 to the summer of 1985. Subsequently he has worked on Brookhaven experiment 805, a search for galactic axions, from the summer of 1985 to the present. The latter work, supervised by Dr. Adrian Melissinos, is summarized in this thesis.

Table of Contents

List of Figures

Appendix A:

List of Tables

Chapter 1: Axions and the Dark Matter Problem

1.1 The Dark Matter Problem

There are a number of indications that there may be more mass present in the universe than has been directly observed so far. As early as 1933, Zwickey pointed out that stars at large distances from the center of galaxies have higher than expected orbital velocities based on the estimated masses of the galaxies[1]. This discrepancy implies the existence of an unseen mass, and has subsequently been well established by the measurement of the rotation curves (orbital velocity as a function of radius) of numerous galaxies. Measurement of the motions of galaxies themselves within clusters also indicates the presence of mass in excess of what is observed. Finally, cosmological arguments indicate that the universe should be flat, $\Omega = 1$, however, observed mass densities yield a value of $\Omega \approx .01$ to $.1$. Together, these considerations imply the existence of "dark matter" on a number of scales.

The rotation curves of virtually all spiral galaxies which have been measured are similar to the one shown in figure 1.1[2]. The feature that the rotation curve remains flat to the limits of the measurement implies the existence of galactic dark matter. In particular, the velocity of an object in a circular orbit as a
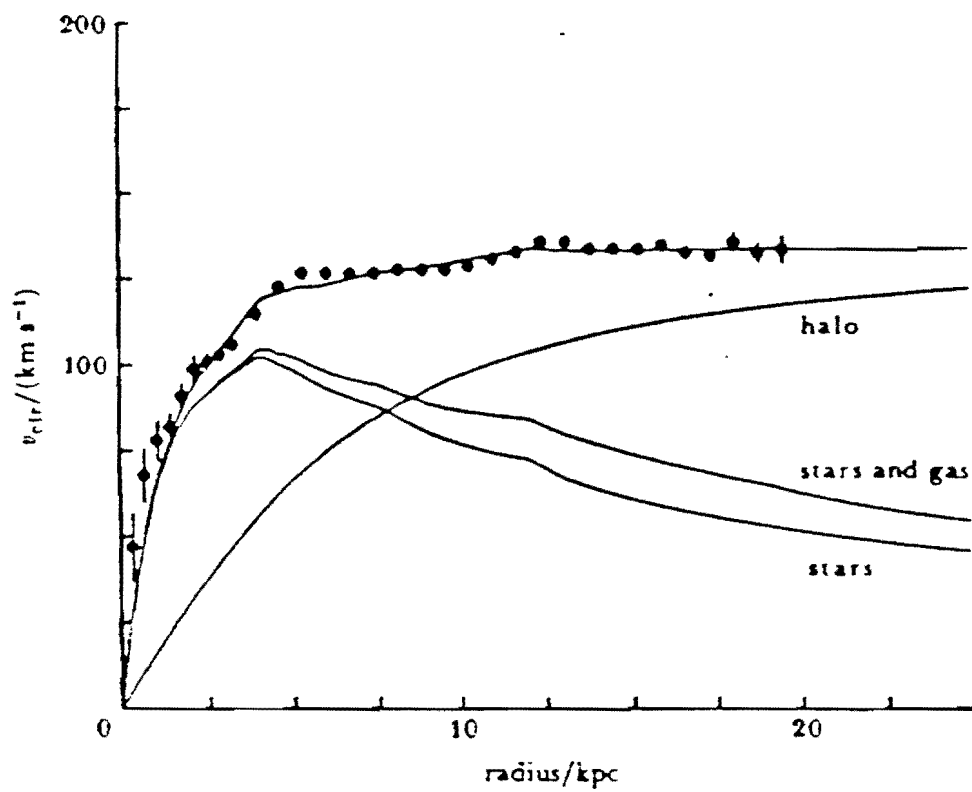
Figure 1.1: Rotation curve of NGC 2403. The relative mass densities of stars, gas, and halo are also shown.

function of the mass inside the orbit is given by,

$$v = \left[\frac{G \ M(r)}{r} \right]^{1/2}$$ (1.1)

where $M(r)$ is the total mass contained inside the radius r. A flat rotation curve is produced when $M(r) \ \alpha \ r$, or alternatively, when the mass density $\rho(r) \ \alpha \ r^{-2}$ (assuming spherical symmetry). If one estimates the distribution of mass in the galaxy based on the observed distribution of luminosity, the light profile, one finds that the mass density at large radii decreases much more quickly than r^{-2}. Consequently, there must be nonluminous mass at large radii in order to reconcile the light profiles with the rotation curves. Various investigators[3] have modeled galactic mass distributions to determine the contribution of dark matter. From these calculations the halo is believed to be well represented by an isothermal sphere model,

$$\rho_{halo}(r) = \frac{\rho_0}{r^2 + a^2}$$ (1.2)

where ρ_0 and $\underline{a}$ are parameters to fit the model to particular galaxies. This model, applied to our galaxy, results in a mass density of the dark matter halo at the radius of the sun of 5×10^{-25} g cm^{-3}, or equivalently 300 MeV/cm^3. The isothermal sphere model also places a lower limit on the total mass of halos to be typically at least a factor ten larger than the mass of the luminous part of the galaxies. The diameters to which the halos extend are not known

3

because the measurement of rotation curves is limited by the size of the luminous part of galaxies. The assumption that the halo is spherically symmetric seems to be supported by measurements of the velocity distribution of stars which lie outside of the galactic plane[4]. In particular, it is expected that the ratio of the minor to major axis of the halo density distribution is ≥ 0.8.

The existence of dark matter in clusters of galaxies is implied by an imbalance of potential and kinetic energy within clusters[5]. The virial theorem states that

$$2\langle T \rangle + \langle V \rangle = 0 \qquad\qquad (1.3)$$

for a system about its center of mass. Based on estimates of mass from luminosity and velocity from red-shifts, it appears that $\langle T \rangle \gg \langle V \rangle$ within clusters of galaxies. This contradiction with the virial theorem can be reconciled by the presence of dark matter. Because $\langle V \rangle$ is proportional to the square of the total mass of a system while $\langle T \rangle$ is linearly proportional to the mass, omission of part of a virial system will result in $\langle T \rangle > \langle V \rangle$.

The cosmological argument that the universe is flat results in a mass density of the universe 10 to 100 times larger that which is observed. In the standard model of cosmology the universe is expanding and, at any time t after the big-bang, is characterized by

4

a scale factor R(t). The Einstein equations governing R(t) are,

$$\ddot{R} = -\frac{4\pi}{3} G \left[\rho + \frac{3k}{c^2}\right] R, \qquad (1.4)$$

$$(\dot{R}/R)^2 = \frac{8\pi}{3} G\rho - k \frac{c^2}{R^2}, \qquad (1.5)$$

where k is the curvature of space. There are three possible conditions: k is equal to -1, 0, +1. k=-1 corresponds to a geometry of space which is that of a saddle and the universe is open, k=0 where the geometry of space is flat, and k=1 where the geometry of space is that of the surface of the sphere and the universe is closed.

The rate of expansion of the universe is given in terms of the Hubble constant

$$H = \dot{R} / R. \qquad (1.6)$$

The current value of H is established to within a factor 2 and is

$$H_0 = \frac{50 \text{ km/sec}}{\text{Mpc}} \approx \frac{1}{20 \times 10^9 \text{ years}}. \qquad (1.7)$$

Using this value we can evaluate the current mean density required

5

for a flat (k=0) universe: the critical density,

$$(\rho_c)_0 = \frac{3\ H_0{}^2}{8\pi G} = 4.7 \times 10^{-30}\ \text{g/cm}^3 = 10^4\ \text{eV/cm}^3. \qquad (1.8)$$

It is convenient to introduce the ratio of a density to the critical density,

$$\Omega = \rho\ /\ \rho_c. \qquad (1.9)$$

Measurement of the observable density of the universe results in $\Omega \approx$ 0.01 to 0.1. Extrapolation of the current value of Ω back to the value it had in the early universe, $t=10^{-6}$ sec, using equations 1.4 and 1.5, indicates that $(\Omega-1) \approx 10^{-48}$. The fact that Ω was so close to 1 leads one to believe that it was in fact equal to 1. This would mean that the current value of Ω would still be 1. In addition, inflationary models of the evolution of the universe directly result in $\Omega=1$, eliminating the fine tuning problem altogether. In either case, the implication is that only a small fraction of the universe has been seen so far.

Having established that there may very well be dark matter in the universe, the question emerges; what is it made of and why is it so dark? Consideration of primordial nucleosynthesis constrains the amount of the dark matter which could be baryonic. It is expected that the density of baryons at the time of nucleosynthesis determines the relative abundances of the elements D, ^{3}He, ^{4}He, and ^{7}Li which

6

have been formed. This can be used to place a limit on the total density of baryons when the current relative abundances of the previously mentioned elements are considered. One finds

$$\Omega_b \sim 3 \times 10^{-7} \ (T_\gamma \ / \ 2.7 \ ^\circ K)(n_b \ / \ n_\gamma) \approx 0.03 \qquad (1.10)$$

where Ω_b is the fraction of the current closure density which is composed of baryons, T_γ is the current temperature of the microwave background, and n_b/n_γ is the current ratio of the number of baryons to the number of photons[6]. Since Ω_b is of the order of what we see and less than 1, this argument indicates that the vast majority of mass is of some more exotic type of matter than baryons. Of course it is still possible that any of the smaller scale dark matter problems, galactic halos for example, could be solved with a form of dark baryonic matter without contradicting the limit on the total amount of baryonic matter. There are observational constraints on this, but baryonic dark matter could be in the form of non-luminous "Jupiters". The pervasiveness of dark matter, however, suggests that its composition could be similar on all scales, and that a non-baryonic halo is a distinct possibility.

Since dark matter should not be baryonic, it may be composed of weakly interacting fundamental particles. Among the known stable particles only the neutrino interacts weakly enough to be a dark matter candidate, but it must have a finite rest mass to provide closure, i.e. make $\Omega=1$. One finds that the contribution to Ω for

7

three species of neutrinos is [7],

$$\Omega_\upsilon = 0.4 \ (m_\upsilon/10 \ eV)(T_\gamma/2.7 \ {}^\bullet K)^3. \qquad (1.11)$$

The upper limit for the mass of the electron neutrino is in the range of 10 eV while the limits on the μ and τ neutrino are much higher. Dark matter neutrinos would have very high energy and are classified as "hot" dark matter[8]. However, theories of the formation of structure in the universe have difficulties when most of the mass is in the form of hot dark matter. Density perturbations are smoothed out too quickly and observed structures do not form. Neutrinos may therefore not be a suitable dark matter candidate. In addition, neutrinos cannot make up galactic halos because they are low mass fermions. It is not possible to fill the gravitational potential of galaxies with enough neutrinos to produce the observed rotation curves.

However, recent theories of particle physics predict a rich selection of weakly interacting particles which could constitute dark matter. A partial list of candidates is given in table 1.1. A highly favored candidate is the axion, which is described in detail below. The extremely weak interactions of the axion make it a prime candidate for both the dark matter to provide closure of the universe and the dark matter of galactic halos.

SPECIES	MASS	ORIGIN	ABUNDANCE
Invisible Axion	10^{-5} eV	10^{-30} sec	10^{9} cm^{-3}
Neutrino	30 eV	1 sec	100 cm^{-3}
Photino/Gravitino	keV −	10^{-4} sec	10^{-3} cm^{-3}
	− GeV	10^{-3} sec	10^{-5} cm^{-3}
Superheavy Magnetic Monopole	10^{16} GeV	10^{-34} sec	10^{-23} cm^{-3}
Black Holes	$> 10^{15}$ g	10^{-12} sec	$< 10^{-44}$ cm^{-3}

Table 1.1: A list of fundamental particles which may make up dark matter.

1.2 Axions

The axion is a consequence of a solution to a problem with quantum-chromo-dynamics. The QCD Lagrangian contains a term

$$L_\theta = \theta G^{\mu\nu} G_{\mu\nu} \qquad (1.12)$$

which violates CP in analogy with $\mathbf{E} \cdot \mathbf{B}$ in electromagnetism (which is even under C and odd under P). The $G^{\mu\nu}$ are the gluon field tensors and θ is a coefficient. However, CP violation in the strong interaction has not been observed. In particular, an experimental upper bound $\theta < 10^{-9}$ on strong interaction CP violation has been placed by measurements of the electric dipole moment of the neutron[9]. To explain naturally why θ should be so small, Peccei and Quinn[10] introduced an approximate global symmetry into the QCD Lagrangian making θ a dynamical variable with possible values $[0, 2\pi]$. The Peccei Quinn (PQ) symmetry is not observed in nature because it was spontaneously broken already at very high temperatures. The breaking of the PQ symmetry results in a potential for θ which has its minimum at $\theta=0$. θ is observed to be so small because it oscillates around the minimum of this potential. As pointed out independently by Weinberg and Wilczek[11], a necessary consequence of the spontaneous breaking of the approximate PQ symmetry is the generation of a nearly massless pseudoscalar particle, dubbed the axion. The axion is a pseudo-Goldstone boson which would be massless if the PQ symmetry had been exact before spontaneous symmetry

breaking had occurred. The axion has a mass which is related to the symmetry breaking scale f_a, which is not specified by the theory,

$$m_a = \frac{\sqrt{2} \ f_\pi m_\pi}{f_a} \qquad (1.13)$$

where $f_\pi = 93$ MeV and $m_\pi = 135$ MeV. The π^0 mass and symmetry breaking scale enter because the π^0 is also a Goldstone boson. From another perspective, the shape of the potential determines the oscillation frequency of θ which in turn determines the mass of the axion. In particular,

$$m_a = \frac{h\nu}{c^2} \qquad (1.14)$$

where ν is the frequency of the oscillation of θ.

In general, axions couple to fermions with a strength $g_a \sim 1/f_a$. The details of the coupling are not a fixed feature of the theory, and various models for the coupling have been developed depending on f_a. f_a was originally thought to equal the weak symmetry breaking scale, $f_{weak} = 100$ GeV, which corresponds to an axion mass of 10^5 eV. However, accelerator experiments have excluded the existence of axions with mass greater than 200 KeV [12]. There are a variety of experiments which contribute to this limit. If the axion mass exceeds 1 MeV then the axion would decay $a \rightarrow e^+e^-$. Axions in this mass range have been searched for with electron accelerators, where axions could be produced in a bremsstrahlung process and decay into

11

$a \rightarrow e^+e^-$ as shown in figure 1.2. In this case the interaction cross section is proportional to the square of the nuclear charge of the target material. Because of their weak interaction, axions pass through an absorber placed behind the target while other particles do not: the signature of an axion would be provided by the e^+e^- pair. Such experiments have set limits excluding axions in the mass range 1 < m_a < 15 MeV provided that the lifetime of the axion lie between 10^{-14} < τ < 10^{-10} sec. Similar experiments which search for axions produced in nuclear reactors which decay into $a \rightarrow \gamma\gamma$ have not produced any positive results[13].

Subsequently, other models have been developed to describe the coupling of lower mass, higher f_a, axions[14]. The two most prominent models are the DFS axion (Dine, Fischler, and Sredniki) and the hadronic axion (Kim). In both models the axion couples to two fermions and, through a triangle graph, to two photons, as shown in figure 1.3. The axion has a different coupling to fermions in the two models. The Lagrangian for interaction between the axion field and the electromagnetic field is given by

$$L_{int} = -(g_{a\gamma\gamma}/4\pi)\mathbf{E}\cdot\mathbf{B}\varphi_a(t) \qquad (1.15)$$

where $\mathbf{E}$ and $\mathbf{B}$ are the electric and magnetic fields, respectively, and
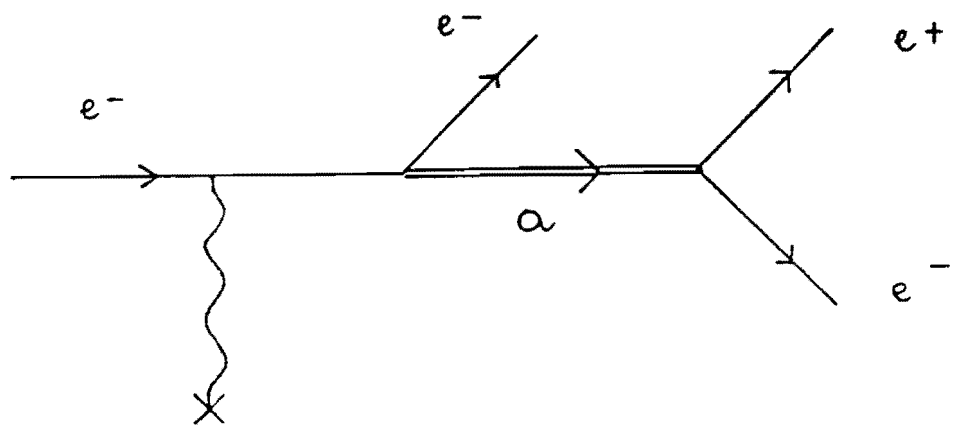
Figure 1.2: Creation of axions through electron bremsstrahlung.
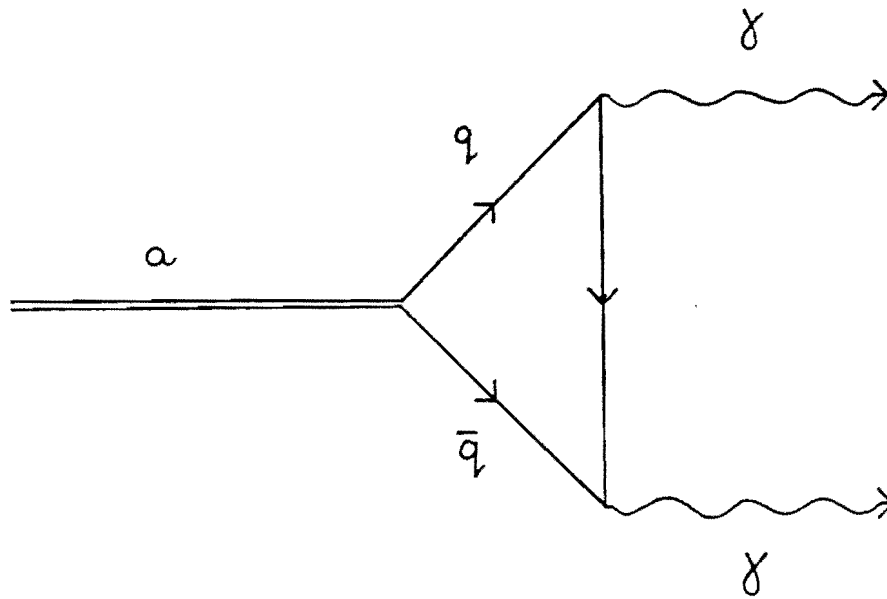
Figure 1.3: The coupling of the axion to two photons through a fermion triangle graph.

$\varphi_a(t)$ is the axion field. The coupling strength of DFS axions is given by,

$$g_{a\gamma\gamma} = m_a \frac{e^2}{\hbar c} \frac{(\hbar c)^{3/2}}{f_\pi m_\pi} (\sqrt{2} \, \pi)^{-1} \qquad (1.16)$$

$$= (1.1 \times 10^{-34} \text{ MeV}^{1/2} \text{ cm}^{3/2}) \frac{m_a}{10^{-5} \text{eV}} . \qquad (1.17)$$

The coupling strength of such axions is so small that they were originally called "invisible" axions. However, they have been found to have important astrophysical and cosmological effects. The existence of axions in certain mass ranges would have effects on helium burning in stars[15]. Because of their weak coupling, axions produced in bremsstrahlung processes in stars would leave without interacting. This would carry energy out of stars, cooling them in conflict with observation and theories of stellar evolution. In addition, the energy carried away from supernova 1987a by neutrinos places a limit on axion production which in turn places a limit on their mass and coupling[16]. These arguments have been used to restrict the possible mass of the axion to masses below accelerator limits. The current limits on the mass of the axion are summarized in figured 1.4 [17] and indicate that $m_a \leq 10^{-3}$ eV. The lower limit on the mass is discussed in the next section.

f_α

(GeV)

10^{-10}

10^{15}

10^{-5}

10^{10}

1

10^5

10^5

m (ev)

axion
overdominate
the universe

supernova
1987A

stellar
evolution

accelerator
experiments
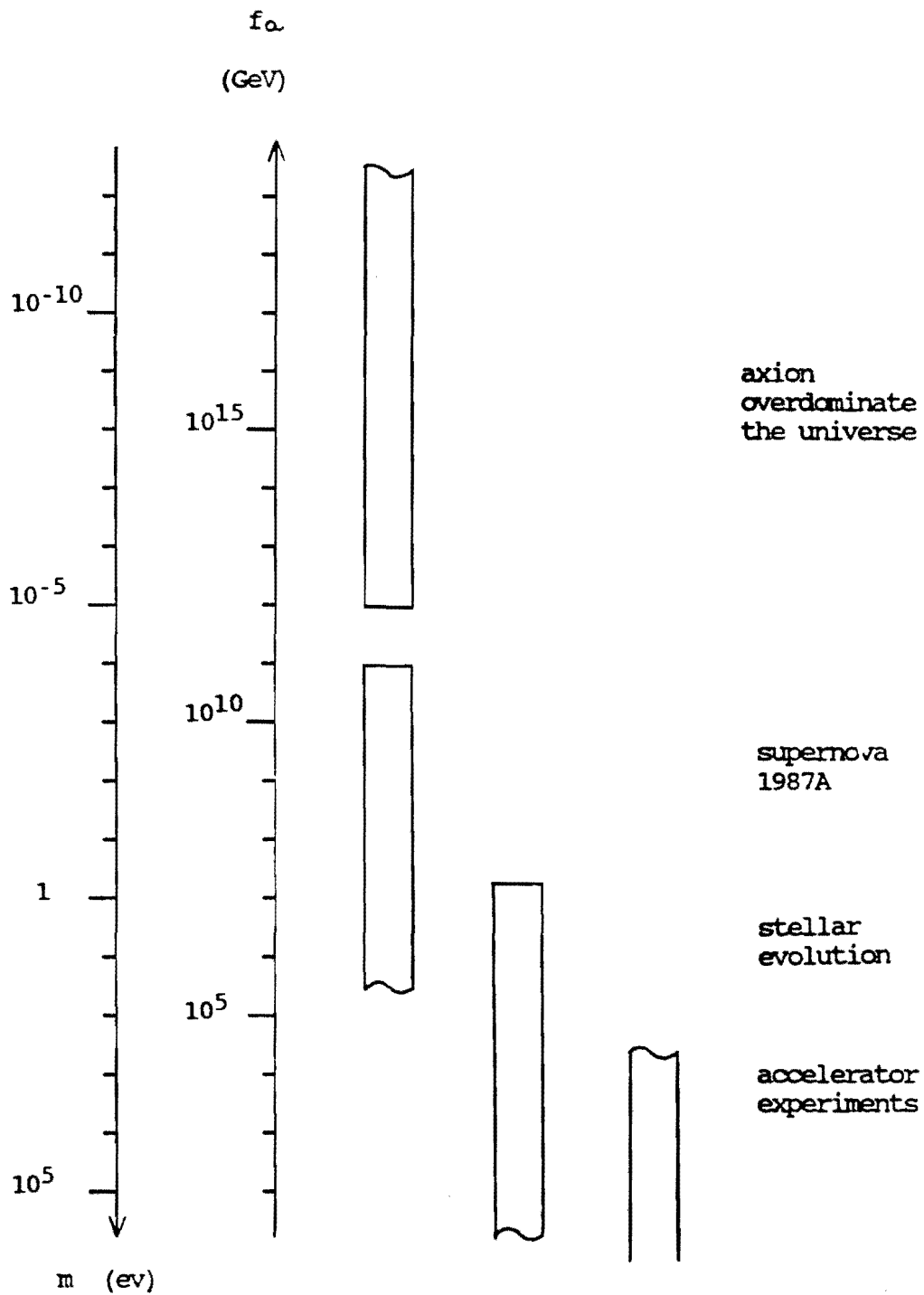
Figure 1.4: A summary of the limits on the mass, and consequently symmetry breaking scale, of axions.

1.3 Formation of Axions in the Early Universe

It is expected that axions were produced in the early universe as
it cooled due to misalignment of θ with the minimum of the potential
caused by the breaking of the PQ symmetry. The shape of the
potential for θ, and consequently the axion mass, is a function of
temperature. In particular, when the temperature of the universe was
above the symmetry breaking scale of the axion, f_a, the PQ symmetry
was intact and the potential for θ was flat. All values of θ were
equally likely, and the axion had zero mass because θ was not
oscillating. At temperatures below the quark hadron transition, on
the order of a GeV, the axion develops a mass because the potential
for θ begins to have a minimum due to instanton effects. This occurs
in analogy with ferromagnetism, where there is no net magnetization
for temperatures above the Curie point but where there is a
spontaneously preferred direction of magnetization below it. As the
universe cooled further below a GeV, coherent field oscillations
began as θ began to roll around in its potential. Today, these
coherent field oscillations represent a condensate of very cold
axions.

It is possible to estimate the energy density in these
oscillations and consequently the mass density of axions. The energy
density depends on how far off from the potential minimum θ was when
the potential formed, on the symmetry breaking scale, and on the
finite temperature dependence of the axion mass. The universe has

expanded since axion formation so that the density of axions has decreased, but it is possible to extrapolate the original density to the current one. The decrease in the axion density due to particle decay is negligible because the lifetime of the axion is so long, in particular,

$$\tau(a \rightarrow \gamma\gamma) \sim 10^7 \ (1 \ eV/m_a)^5 \ \tau_{universe}. \qquad (1.18)$$

The energy density created when axions were formed increases with increasing f_a, so it is possible to place a lower limit on the mass of the axion since there is an observational limit on $\Omega \leq 10$. The limits are,

$$f_a \geq 4.3 \ ^{+5.0}_{-2.3} \times 10^{12} \ GeV, \qquad (1.19)$$

$$m_a \leq 0.8 \ ^{+1.0}_{-0.4} \times 10^{-5} \ eV. \qquad (1.20)$$

The assumption that axions do, in fact, provide the closure density of the universe transforms this limit into a prediction of mass.

The formation of structure in the universe is explained by the fact that different areas of the universe passed through the symmetry breaking scale at different times. One expects certain fluctuations to exist in the radiation dominated energy spectrum of the universe and that these fluctuations will be transferred to the axion field during cooling. These fluctuations eventually lead to the formation of galaxies, clusters, and superclusters. Axions form a

18

collisionless gas and therefore cannot dissipate energy after they are formed. The initial nonuniformities in the axion mass distribution are essential to the formation structures as they cannot be formed later.

Axions in the allowed mass range of figure 1.4 are thus prime candidates for the dark matter of galactic halos. An experiment which seeks to directly observe such galactic axions is described in this thesis. Axions which form a gravitationally bound galactic halo are expected to move with velocities approximately equal to those of luminous objects if the orbits are similar: $\beta = v/c \sim 10^{-3}$. The energy spectrum of the axions is therefore the rest mass spread slightly by the kinetic energy. A more detailed calculation of the energy distribution, based on a Maxwellian velocity distribution, yields an axion "quality factor", Q (energy, E_a, divided by energy width, ΔE_a) of[18],

$$Q_a = \frac{E_a}{\Delta E_a} \approx 3 \times 10^6. \qquad (1.21)$$

A narrow signal from the axions decay photons is part of the experimental signature of galactic halo axions. The direct detection of halo axions would yield a wealth of new information about galaxies, formation of structure in the universe, and cosmology, and a signature from a very early time.

References

1. F. Zwickey, Helv. Phys. Acta. **6**, 110 (1933).

2. T.S. Van Albada and R. Sancisi, Phil. Trans. R. Soc. Lond. **A320**, 447 (1986).

3. J. Bahcall and R. M. Soneira, Astrophys. J. Suppl. **44**, 73 (1980); J. Bahcall, M. Schmidt, R.M. Soneira, Astrophys. J. **265**, 730 (1983); M. Turner, Phys. Rev. **D33**, 889 (1986).

4. Proceedings of IAU Symposium 117: Dark Matter in the Universe, eds. J. Kormandy and E. Turner (1985).

5. R. Tayler, Phil. Trans. R. Soc. Lond. **A 320**, 435 (1986).

6. $n_\gamma = 400$ cm^{-3} and $n_b = 10^{-7}$.

7. M. Turner, *Techniques of High Energy Physics, Volume 3*, ed. T Ferbel (Plenum, NY 1985).

8. Hot dark matter is a generic term which refers to highly relativistic dark matter. Cold dark matter has very low velocities.

9. The limit on the electron dipole moment is $(edm)_n \le 10^{-25}$ ecm, D. Dubbers, Nucl. Instr. Meth. **A264**, 120 (1988).

10. R. Peccei and H. Quinn, Phys. Rev. Lett. **38**, 1440 (1977).

11. S. Weinberg, Phys. Rev. Lett. **40**, 223 (1978); F. Wilczek, Phys. Rev. Lett. **40**, 279 (1978).

12. K. B. Luk, Proceedings of the XXIII International Conference on High Energy Physics, p. 632, ed. S. C. Loken (World Scientific, Singapore 1987); E. M. Riordan et. al., p. 635.

13. J.-L. Vuilleumier, F. Boehm, A.A. Hahn, H, Know, F.v. Feilitzsch, and R. L. Mossbauer, Phys. Lett. **101B**, 341 (1981).

14. M. Dine, W. Fishcler, and M. Sredniki, Phys. Lett. **104B**, 199 (1981); J. Kim, Phys. Rev. Lett. **43**,103 (1979).

15. J. A. Frieman, S. Dimopoulos, M. S. Turner, Phys. Rev. D, **36**, 2201 (1987); D. S. Dearborn, D. N. Schramm, G. Steigman, Phys. Rev. Lett. **56**, 26 (1986).

16. M. S. Turner, Phys. Rev. Lett. **60**, 1797 (1988).

17. Thanks to G. Raffelt for the idea of graphing the limits in this way.

18. L. Krauss, J. Moody, F. Wilczek, and D. E. Morris, Phys. Rev. Lett. 55, 1797 (1985); J. Rogers, UR-1021 (1987).

Chapter 2: The Detection Scheme and Experimental Configuration

2.1 Detection of a → γγ

In spite of the weak coupling of axions in the non-excluded mass range, it is possible to enhance the decay a → γγ with a technique originally proposed by Sikivie[1]. A detector based on this technique can be built to try to directly determine if axions make up the dark matter halo. There are two basic steps enhancing a → γγ. First, one of the two photons of the decay is provided by a virtual photon supplied from an externally applied magnetic field. This enhances the rate for the transition a → γγ in analogy to the Primakoff effect[2] for the production of π^0's. The virtual photon from the magnetic field provides the momentum balance and one observes a single photon from the decay which carries the full energy of the axion. The reaction is shown in figure 2.1. Secondly, if the decay occurs in a high Q electromagnetic cavity tuned to the frequency of the emitted photon the decay will be enhanced because of the increased density of final states (which is proportional to the Q of the cavity). The frequencies of photons produced in the decay of allowed mass axions lie in the microwave range: for example, 10^{-5} eV = 2.4 GHz. The expected signal strength from such a detector depends on the coupling of halo axions, the local halo density, and on the various parameters of the detector. In the following section we calculate the conversion of halo axions into microwave photons in a
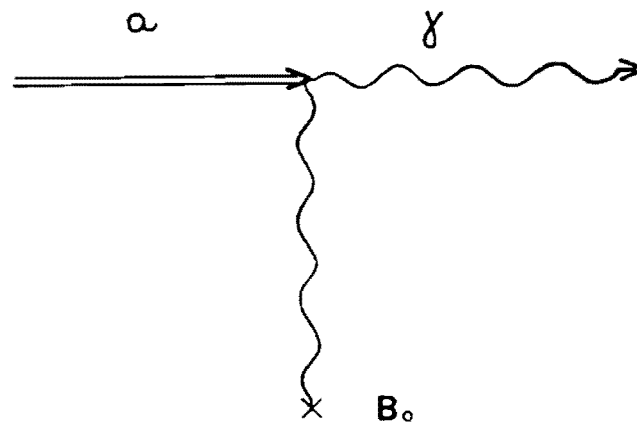
Figure 2.1: Axion to photon conversion via the Primakoff effect.

cavity in a magnetic field, which gives the expected sensitivity of such a detector to galactic halo axions.

As we have seen in section 1.3, it is expected that halo axions are moving very slowly, $\beta \approx 10^{-3}$. It is therefore possible to describe their interaction with the electromagnetic field classically[3],

$$L_{int} = - \frac{g_{a\gamma\gamma}}{4\pi} \mathbf{E} \cdot \mathbf{B} \; \varphi_a(t). \qquad (2.1)$$

The coupling strength, $g_{a\gamma\gamma}$, is dependent on the axion model as discussed in section 1.2. We will assume a coupling according to the DFS model,

$$g_{a\gamma\gamma} = m_a \frac{e^2}{\hbar c} \frac{(\hbar c)^{3/2}}{f_\pi m_\pi} \; (\sqrt{2}\pi)^{-1}. \qquad (2.2)$$

The functional form of $\varphi_a(t)$ is determined by the velocity distribution of the halo axions. The relationship is more clear if one considers the Fourier transform of $\varphi_a(t)$,

$$\varphi_a(\omega) = \int_{-\infty}^{\infty} \varphi_a(t) \; e^{i\omega t} \; dt \qquad (2.3)$$

and consequently,

$$\varphi_a(t) = \frac{1}{2\pi} \int_{-\infty}^{\infty} \varphi_a(\omega) \; e^{-i\omega t} \; d\omega. \qquad (2.4)$$

24

$\varphi_a(\omega)$ is related to the energy distribution of the axion halo by $\left|\varphi_a(\omega)\right|^2$ $d\omega \sim P(\omega)$ $d\omega$, where $P(\omega)$ is the total energy spectrum of the halo axions at energy $\hbar\omega$. If, for example, all of the halo axions happened to be at rest relative to the laboratory, then $\varphi_a(\omega)$ would have the form of a delta function centered on $\omega = m_a c^2/\hbar$. However, as described in section 1.3, it is expected that halo axions have a Maxwellian velocity distribution and move with velocities typical of luminous galactic objects. This velocity distribution results in a slightly broadened energy spectrum: i.e. makes $P(\omega)$ wider. In addition, the local axion mass density is related to $\varphi_a(\omega)$ by,

$$\langle \rho \rangle_{halo} = m_a^2 \int_{-\infty}^{\infty} \left|\varphi_a(\omega)\right|^2 \, d\omega/2\pi. \qquad (2.5)$$

and to $\varphi_a(t)$ by Parseval's theorem,

$$\langle \rho \rangle_{halo} = m_a^2 \int_{-\infty}^{\infty} \left|\varphi_a(t)\right|^2 \, dt. \qquad (2.6)$$

In the presence of an applied magnetic field, B_{ext}, the complete Lagrangian describing the electromagnetic field and direct axion to two photon coupling becomes (in Gaussian units),

$$L = \frac{1}{8\pi}(\epsilon E^2 - 1/\mu B^2) - \frac{g_{a\gamma\gamma}}{4\pi} E \cdot B_{ext} \, \varphi_a(t). \qquad (2.7)$$

This corresponds to an equation of motion,

$$\nabla^2 E - \frac{1}{c^2} \frac{\partial^2 E}{\partial t^2} - \frac{g_{a\gamma\gamma}}{c^2} B_{ext} \frac{\partial^2 \varphi_a(t)}{\partial t^2} \quad . \qquad (2.8)$$

The axion field becomes an electric field driving term in the presence of an external magnetic field. Equation 2.8 can be solved inside a resonant cavity with finite Q by first taking its Fourier transform,

$$\nabla^2 E(x,\omega) + \frac{\omega^2}{c^2} E(x,\omega) = - g_{a\gamma\gamma} B_{ext} \frac{\omega^2}{c^2} \varphi_a(\omega) . \qquad (2.9)$$

The boundary conditions of the cavity and energy dissipation caused by finite Q result in a steady state energy, U_j, in the cavity for the jth mode,

$$U_j = g_{a\gamma\gamma}{}^2 G_j{}^2 V B_0{}^2 \int \frac{|\varphi_a(\omega)|^2 \omega^4}{(\omega-\omega_j)^2 + \omega^4 / Q^2} \frac{d\omega}{4\pi} \qquad (2.10)$$

where $B_0{}^2$ is the average of the square of the magnetic field inside the cavity,

$$B_0{}^2 = \frac{1}{V} \int |B_{ext}(x)|^2 d^3x \qquad (2.11)$$

26

and $G_j{}^2$ is defined by the integral,

$$G_j = \frac{1}{B_0} \frac{\int B_{ext} \cdot E_j \; d^3x}{\int E_j \cdot E_j \; d^3x} \qquad (2.12)$$

for the jth mode of the cavity. All integrations are over the cavity volume, V. The quantity $G_j{}^2$ is a factor which indicates how well the electric field in the cavity lines up with the applied magnetic field. This quantity severely limits which resonant modes of the cavity can be used, as symmetries in most resonant modes result in cancellations which make $G_j{}^2$ equal to zero.

It is expected that the axion power spectrum is narrower than the bandwidths of the copper microwave cavities which are used in the experiment (see chapter 3 for cavity bandwidths). In particular, $Q_{cavity} \approx 10^5$ and $Q_{axion} \approx 3 \times 10^6$. In order that the integral in equation 2.10 be non-zero, the maximum of $|\varphi_a(\omega)|^2$ must lie within the bandwidth of the cavity mode under consideration, i.e. the cavity must be tuned to the axion frequency to within the cavity resonance width. Since the mass of the axion is not known, the tune of the microwave cavity must be swept until the cavity resonance coincides in frequency with the peak of the axion power spectrum in order to see the axion signal. When this is the case, the energy in the cavity due to the conversion of axions is given by,

$$U_j = \left(\frac{g_{a\gamma\gamma}}{m_a} \right)^2 \langle \rho \rangle_{halo} \; Q_L{}^2 \; [\epsilon_0 (cB_0)^2] \; V \; G_j{}^2 \qquad (2.13)$$

27

where Q_L [4] is the loaded Q of the cavity. When the cavity is coupled to an external receiver with a coupling strength Q_{ext} the power available to the receiver is,

$$P = \frac{\omega U}{Q_{ext}} .$$ (2.14)

Thus the available axion signal strength becomes,

$$P_a = \left(\frac{g_{a\gamma\gamma}}{m_a} \right)^2 \langle \rho \rangle_{halo} \ \omega \ \frac{Q_L^2}{Q_{ext}} \ [\epsilon_0 (cB_0)^2] \ V \ G_j^2$$ (2.15)

when the cavity is tuned to the frequency of the axion. One can rewrite equation 2.15, the expected signal power, in terms of typical experimental parameters,

$$P_a = (3.44 \times 10^{-24} \text{ W}) \left(\frac{f}{1 \text{ GHz}} \right) \left(\frac{V}{10^4 \text{ cm}^3} \right) \left(\frac{Q_L}{10^5} \right) \left(\frac{G_j^2}{0.7} \right) \left(\frac{B}{8.5 \text{ T}} \right)^2$$ (2.16)

where $f = \omega/2\pi$, the frequency of the axion. Equation 2.16 is valid for critical coupling. Not all of these experimental parameters are constant across the range of the axion masses covered by this experiment, however, this gives an idea of the magnitude of the signal one is searching for.

28

2.2 An Overview of the Experimental Configuration

Searching for axions thus consists of monitoring the output of a microwave cavity in a magnetic field at the resonant frequency of an appropriate mode. The resonant frequency is swept, and when it equals the axion frequency, a signal with a power given by equation 2.15 and width f/Q_{axion}, will be seen. The apparatus for such an experiment consists of a magnet, a microwave cavity, and a receiver system. The expected signal strength is proportional to the square of the applied magnetic field, so we have chosen to use a superconducting solenoid magnet which has a peak field of 8.5 Tesla. The magnet has a 6 inch diameter by 16 inch long bore and is suspended near the bottom of a large liquid helium dewar. Details about the magnet and the cryostat system are given in appendix B. The microwave cavity is placed inside the bore of the magnet. The cavity has a right circular cylindrical geometry and is constructed from high purity copper in order to achieve as high a Q as possible. Unloaded Q's on the order of 1.8×10^5 in the range of 1 to 6 GHz have been measured when the cavities have been cooled in the liquid helium bath. The resonant frequency of the cavity is tuned by varying the insertion of a dielectric rod along the central axis of the cavity and microwave power is coupled out of the cavity by an inductive coupling loop. The microwave cavities are discussed in detail in chapter 3. The output of the cavity is continuously monitored by a microwave receiver whose first stage consists of a cryogenic preamplifier. This is followed by a superheterodyne

section, and finally, a 64 channel filter-detector system. As the resonant frequency of the cavity is swept the output of the receiver is recorded by a computer, and from this data, a power vs. frequency spectrum is produced. The data has a background power level which is due to thermally generated noise from the microwave receiver and from the cavity itself; against this background the axion signal should appear as a narrow peak. The fluctuations in the background power level are proportional to the noise temperature and the square root of the averaging time, and mimic the expected signal peak thus limiting the sensitivity of the experiment. The receiver electronics and data taking process are described in chapter 4.

2.3 The Expected Sensitivity of the Experiment

The sensitivity of the detector is limited by the thermally generated noise of the microwave cavity and the cryogenic preamplifier. The noise power generated by a device of noise temperature T, in a bandwidth B, in an impedance matched system is given by,

$$P = kTB \qquad (2.17)$$

where k is Boltzmann's constant. The noise temperature corresponds to the physical temperature in the case of a resistor but may be different, higher or lower, in the case of an active device. Typical

30

noise temperatures of the axion detector are 15 °K (4.2 °K from the cavity and 11 °K from the amplifier), thus the noise power level which one expects within the axion signal width is

$$P_{noise} = 2.07 \times 10^{-22} \frac{f_{axion}}{Q_{axion}} \quad W. \tag{2.18}$$

In the frequency range covered by this experiment the ratio f_{axion}/Q_{axion} lies between 200 and 400 Hz. The individual noise generating components are not entirely impedance matched, due mainly to the presence of the microwave cavity, however the resultant noise spectrum is flat and can be treated as if its source were impedance matched. A more detailed discussion of the individual contributions to the noise spectrum can be found in section 4.3.

The distribution of measured thermal noise power for individual measurements $\rho_P(x)$, has a standard deviation equal to its mean, and is given explicitly by,

$$\rho_P(x) = \frac{1}{\sigma} e^{-x/\sigma} \tag{2.19}$$

where σ is the mean and the standard deviation and x is the measured noise power. Thus the fluctuations in the noise spectrum are equal to P_{noise}. One must therefore average the output of the receiver to bring these fluctuations below the level of the expected signal. If N successive power spectra are averaged, the resulting spectrum will have the same average power level but the standard deviation will be

31

reduced by $\sqrt{N}$. In particular, the distribution of power levels in N averaged spectra is given by,

$$\rho_P(x) = \frac{1}{\sigma^N} \frac{N^N}{(N-1)!} x^{N-1} e^{-Nx/\sigma}. \qquad (2.20)$$

This means the limiting sensitivity with respect to the power of the axion signal improves as $\sqrt{N}$, and with respect to $g_{a\gamma\gamma}$ improves by $N^{1/4}$, since $P_a \propto g_{a\gamma\gamma}^2$.

The expected axion signal power from equation 2.16 is $P_a \approx 3 \times 10^{-24}$ W, much smaller than P_{noise} by a factor on the order of 10^4. 10^8 averaged measurements of a section of power spectrum would therefore be needed in crder to see the axion signal at expected signal levels. But since the detector must be swept over a wide range of frequencies, the number of averages which can be taken is limited. The rate at which the active band of the detector, the cavity resonance, can be swept is limited by the time that a given frequency is being sampled, which in turn limits the number of averages, N. This is given by the relation,

$$N = \frac{\text{Active width of detector}}{\text{sweep rate}} \times \frac{1}{\text{time per average}}. \qquad (2.21)$$

Typical sweep rates during data taking are 200 to 800 Hz/sec which results in 5×10^5 averages. A detailed discussion of the experimental sensitivity which has been achieved with this experiment can be found in chapter 5.

This experiment has covered the frequency range 1.09 to 2.46 GHz, or corresponding masses of $.45 \times 10^{-5}$ to 10^{-5} eV. The frequency range of 1.22 to 2.46 GHz is covered in this thesis. Previous publications by our group have discussed the range of 1.09 to 1.22 GHz [5].

References

1. P. Sikivie, Phys. Rev. Lett. 51,1415 (1983), and 52,695 (1984).

2. H. Primakoff, Phys. Rev. 81, 899 (1951).

3. L. Krauss, J. Moody, F. Wilczek, and D. Morris, Phys. Rev. Lett. 55, 1797 (1985).

4. Section 3.2 describes the relationships between Q_0, Q_L, and Q_{ext}.

5. S. De Panfilis, A. C. Melissinos, B. E. Moskowitz, J. T. Rogers, Y. K. Semertzidis, W. Wuensch, H. J. Halama, A. G. Prodell, W. B. Fowler, and F. A. Nezrick, Phys. Rev. Lett. 59, 839 (1987); J. Rogers, University of Rochester publication UR-1021 (1987).

Chapter 3: The Microwave Cavities

3.1 Introduction to Cavity Modes

The resonant frequencies of the right circular cylindrical cavities used in this experiment are given by[1],

$$f = \frac{c}{2} \left[\left(\frac{2x_{\ell m}}{\pi D} \right)^2 + \left(\frac{n}{L} \right)^2 \right]^{1/2} \tag{3.1}$$

where D is the diameter and L is the length of the cavity. ℓ, m, and n are the mode numbers which indicate the number of variations in the field relative to φ, r, and z respectively[2]. The values of $x_{\ell m}$ are the roots of the Bessel function $J_\ell(x)$ for TM modes, and of the derivative of the Bessel function $J_\ell'(x)$ for TE modes. The lowest roots are summarized in table 3.1. The resonant frequencies can also be given graphically in a very convenient form, a mode chart, as shown in figure 3.1. The equations which give the field configurations of the modes are listed in table 3.2.

Because of the dependance of the signal power on G_j^2, equation 2.12 which is related to the integral of $\mathbf{E} \cdot \mathbf{B}_{ext}$ over the cavity volume, most of the cavity resonances can not be used. The microwave cavity is placed in the bore of the superconducting solenoid magnet with the cavity axis along the axis of the magnet. Thus the applied magnetic field has primarily a z component. As a consequence, the resonant mode which is used must have a net z component of the

34

TE-mode	x_{lm}	TM-mode	x_{lm}
11n	1.841	01n	2.405
21n	3.054	11n	3.832
01n	3.832	21n	5.136
31n	4.201	02n	5.520
41n	5.318	31n	6.380
12n	5.332	12n	7.016
51n	6.415	41n	7.588
22n	6.706	22n	8.415
02n	7.016	03n	8.654
61n	7.501	51n	8.772
32n	8.016	32n	9.761
13n	8.536	61n	9.936
71n	8.578	13n	10.174
42n	9.283		
81n	9.648		
23n	9.970		
03n	10.174		

Table 3.1: The mth roots of $J_{\ell}(r)$ and $J_{\ell}'(r)$.
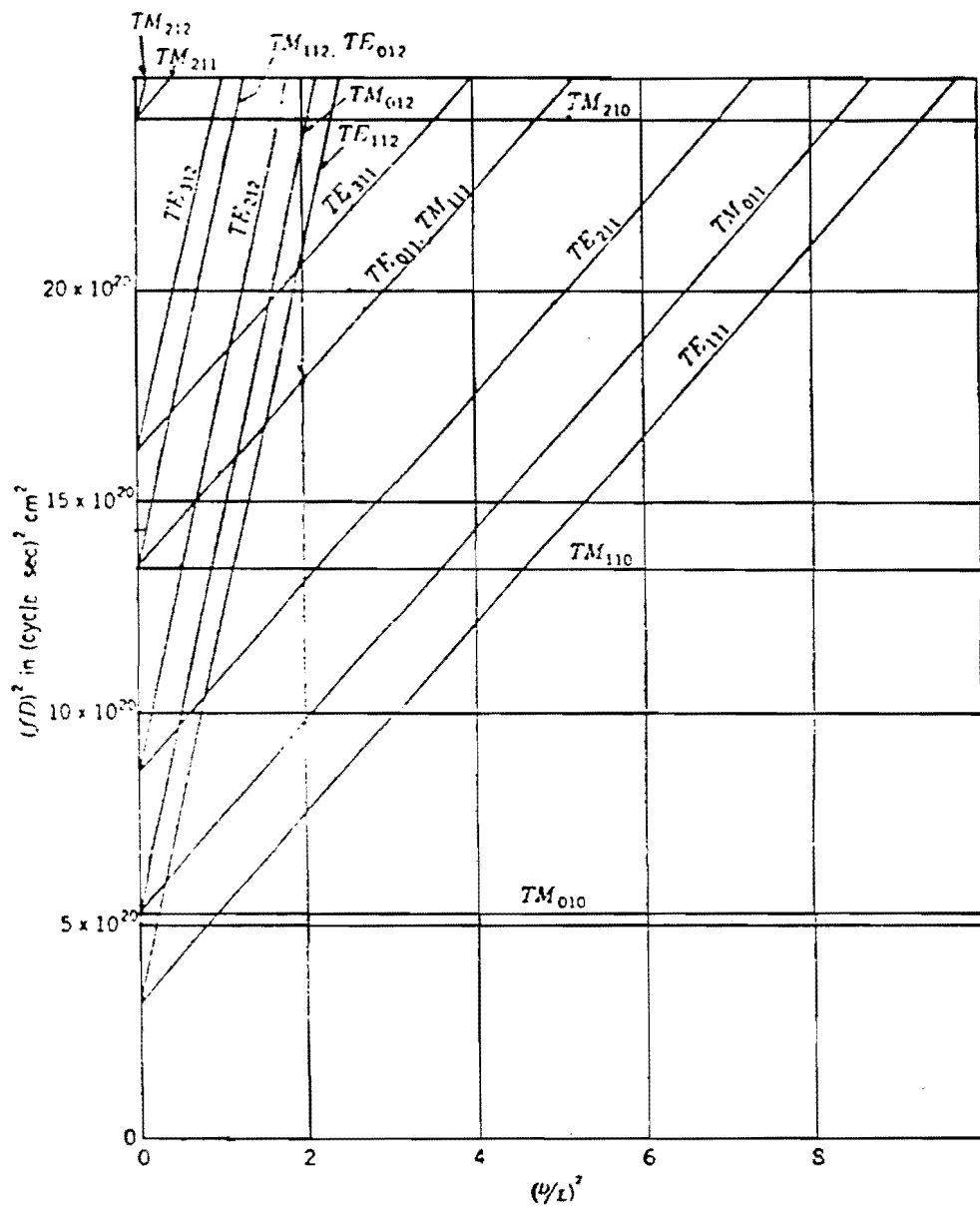
Figure 3.1: Resonant modes of right circular cylindrical cavities.

For TM modes,

$$E_r = -\frac{k_3}{k} J_\ell{}'(k_1) \cos(\ell\varphi)\ \sin(k_3 z)$$

$$E_\varphi = \ell\ \frac{k_3}{k}\ \frac{J_\ell(k_1 r)}{k_1 r}\ \sin(\ell\varphi)\ \sin(k_3 z)$$

$$E_z = \frac{k_1}{k} J_\ell(k_1 r)\ \cos(\ell\varphi)\ \cos(k_3 z)$$

$$H_r = -\ell\ \frac{J_\ell(k_1 r)}{k_1 r}\ \sin(\ell\varphi)\ \cos(k_3 z)$$

$$H_\varphi = -J_\ell{}'(k_1 r)\ \cos(\ell\varphi)\ \cos(k_3 z)$$

$$H_z = 0 \hspace{6cm} m > 0$$

For TE modes,

$$E_r = -\ell\ \frac{J_\ell(k_1 r)}{k_1 r}\ \sin(\ell\varphi)\ \sin(k_3 z)$$

$$E_\varphi = -J_\ell{}'(k_1 r)\ \cos(\ell\varphi)\ \sin(k_3 z)$$

$$E_z = 0$$

$$H_r = \frac{k_3}{k}\ J_\ell{}'(k_1 r)\ \cos(\ell\varphi)\ \cos(k_3 z)$$

$$H_\varphi = -\ell\ \frac{k_3}{k}\ \frac{J_\ell(k_1 r)}{k_1 r}\ \sin(\ell\varphi)\ \cos(k_3 z)$$

$$H_z = \frac{k_1}{k}\ J_1(k_1 r)\ \cos(\ell\varphi)\ \sin(k_3 z) \hspace{2cm} m > 0,\ n > 0$$

where $k_1 = 2x_{\ell m}/D$, $k_3 = n\pi/L$, $k^2 = k_1{}^2 + k_3{}^2$, where D is the diamter and L is the length of the cavity.

Table 3.2: Field equations for the resonant modes of a right circular cylindrical cavity.

electric field in order that $G_j^2 \neq 0$. Since $E_z = 0$ for all TE modes, $G_j^2 = 0$ and no TE modes can be used. Of the TM modes, only the TM_{0m0} modes have non-zero G_j^2. Variations of the fields in φ or z are full wave variations and result in a net E_z which is equal to zero. For TM_{0m0} modes,

$$G_j^2 = \frac{4}{x_{0m}^2} . \qquad\qquad (3.2)$$

The question emerges of which of the TM_{0m0} modes it is most advantageous to use. We consider the value of the product $G_j^2 V$, where V is the volume of the cavity, because the expected axion signal strength is proportional to it. The frequency of the TM_{0m0} mode is given by $f = cx_{0m}/\pi D$, and is independent of the length of the cavity. For a fixed cavity length, the volume of a cavity designed to have a particular frequency will depend on the mode chosen and will be proportional to x_{0m}^2. Consequently, $G_j^2 V$ is equal to a constant for a *particular* frequency. In other words, it is possible to use a larger cavity in a higher mode or a smaller cavity in a lower mode to the same effectiveness. However, it is best to use the lowest mode, the TM_{010}, because of the increased density of modes at higher frequencies, as shown in the mode chart. When the relevant resonant frequency of the cavity is swept during data taking, it crosses other modes. These "mode crossings" result in lost frequency coverage and make tracking the correct mode difficult. Mode crossings shall be discussed in detail in section 3.3.

38

3.2 Coupling to Cavity Modes

In order to couple to the resonant modes, the cavities have two inductive loop coupling ports. The ports consist of 50 Ω coax probes with loops on the end which lie inside closely fitting circular cross section tubes projecting up from the top-plate of the cavity, figure 3.2. The tube diameters are well below the cutoff diameter for circular wave-guide mode propagation of the resonant frequency of the cavity. One coax probe and tube assembly, the major port, is used to pick up the microwave signal inside the cavity. The other, the minor port, is used to inject power into the cavity for cavity transmission measurements and to inject test signals into the cavity during data taking. The planes of the loops are fixed to lie along the radius of the cavity in order to intercept the magnetic flux lines of the TM_{010} mode. The major and minor ports are mounted radially opposite each other at radii of $.64 \times r_{cavity}$ and $.8 \times r_{cavity}$ respectively. Since the magnetic field of the TM_{010} mode varies as the derivative of the Bessel function as a function of radius, the major port is in a region of high magnetic field of the TM_{010} mode while the minor port is in a region of low magnetic field. The vertical position of the probe of the major port inside the tube can be changed to allow adjustment of the coupling strength. The coupling strength is given by

$$\beta = \frac{Q_0}{Q_{ext}} . \qquad (3.3)$$
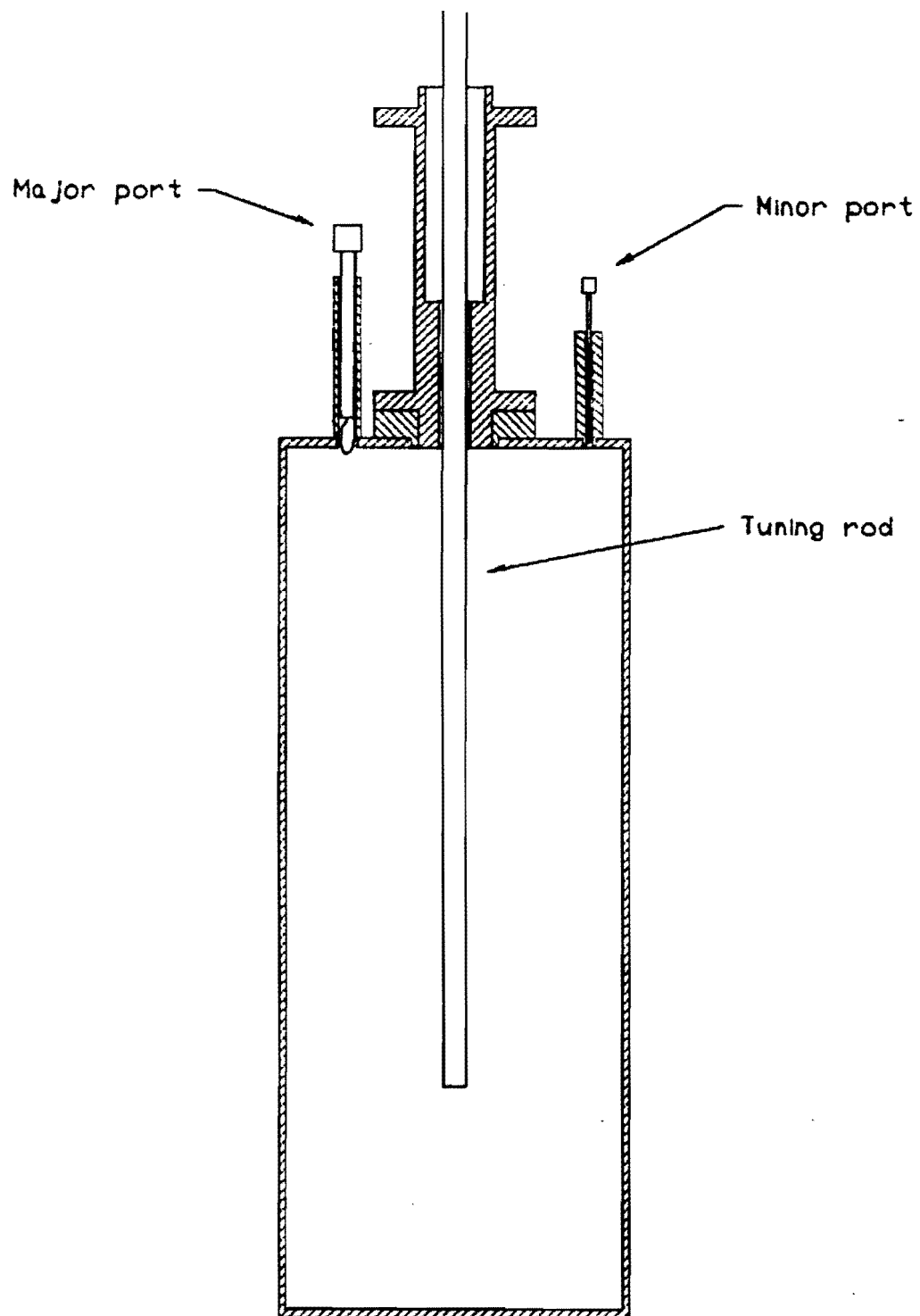
Figure 3.2: Cross section of one of the microwave cavities.

Q_{ext} is given by the equation,

$$\frac{1}{Q_L} = \frac{1}{Q_0} + \frac{1}{Q_{ext}}$$
(3.4)

where Q_L is the loaded Q of the cavity, and Q_0 is the unloaded Q of the cavity. The coupling strength of the major port is adjustable from undercoupling, $\beta < 1$, to overcoupling, $\beta > 1$, but is kept near critical coupling, $\beta = 1$, during data taking. This is done to keep the center of the cavity resonance impedance matched to the rest of the microwave system. The minor port is fixed to a low coupling strength, typically $\beta \leq 3 \times 10^{-4}$. By observing the transmission of the cavity from the minor port to the major port as a function of frequency, the resonant frequency and the resonance width of the cavity modes can be measured to determine the cavity Q. This is accomplished by using an HP8341A synthesized sweeper and an HP8757A Scalar Network Analyzer which are connected through a dedicated HP-IB interface. The network analyzer, by controlling the synthesizer, measures and displays the transmission curve, and then calculates the central frequency and bandwidth of a cavity mode by internally defined functions. A transmission curve of the TM_{010} mode of cavity II is shown is figure 3.3. Figure 3.4 shows transmission through the cavity on a broader scale where one can see a number of resonances. The synthesizer and network analyzer are also used to measure the reflection coefficient of the major port as a function of frequency to determine the coupling strength.

41

CH1: A   —   .00 dB
  2.0 dB/   REF   +   2.00 dBm

1 >BW   −03.00 dB
         +8.4480kHz

STRT   +1.4147GHz   CRSRd +8.4480kHz   STOP   +1.4147GHz
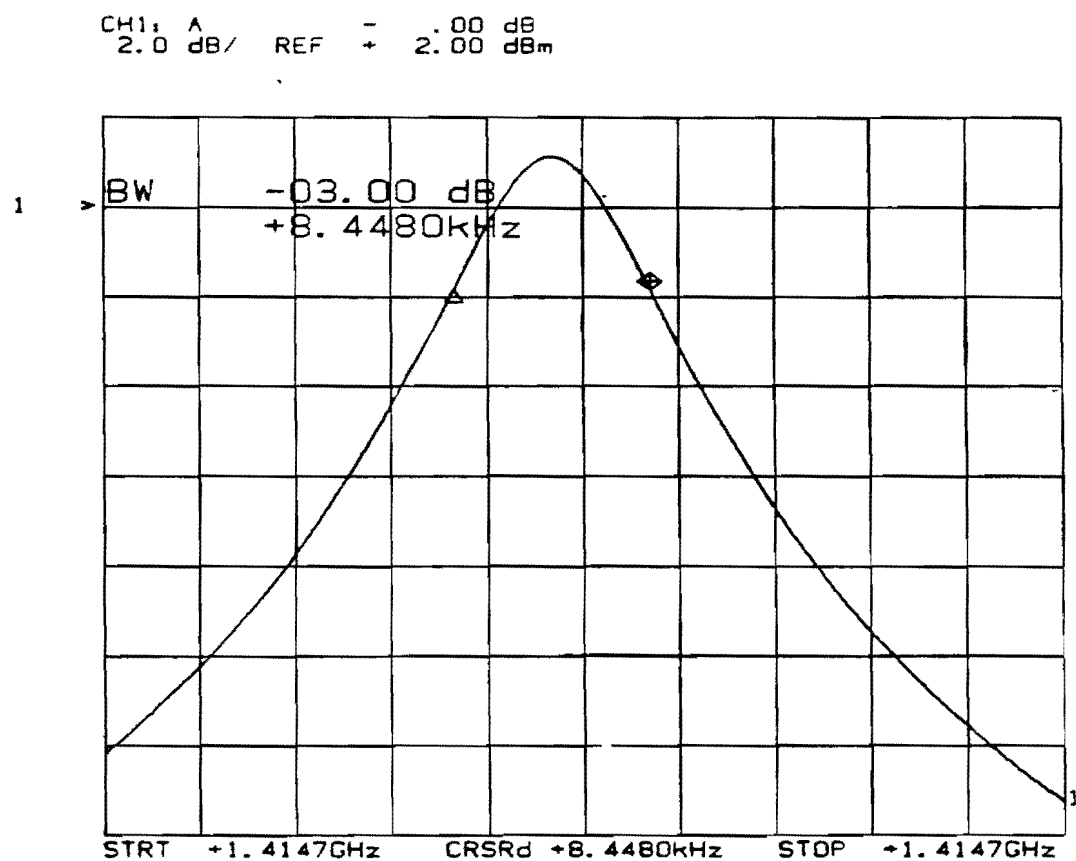
Figure 3.3: Transmission curve of cavity II at 4.2 °K, TM_{010} under-coupled.

42

STRT +1.2288GHz   STOP +1.6005GHz
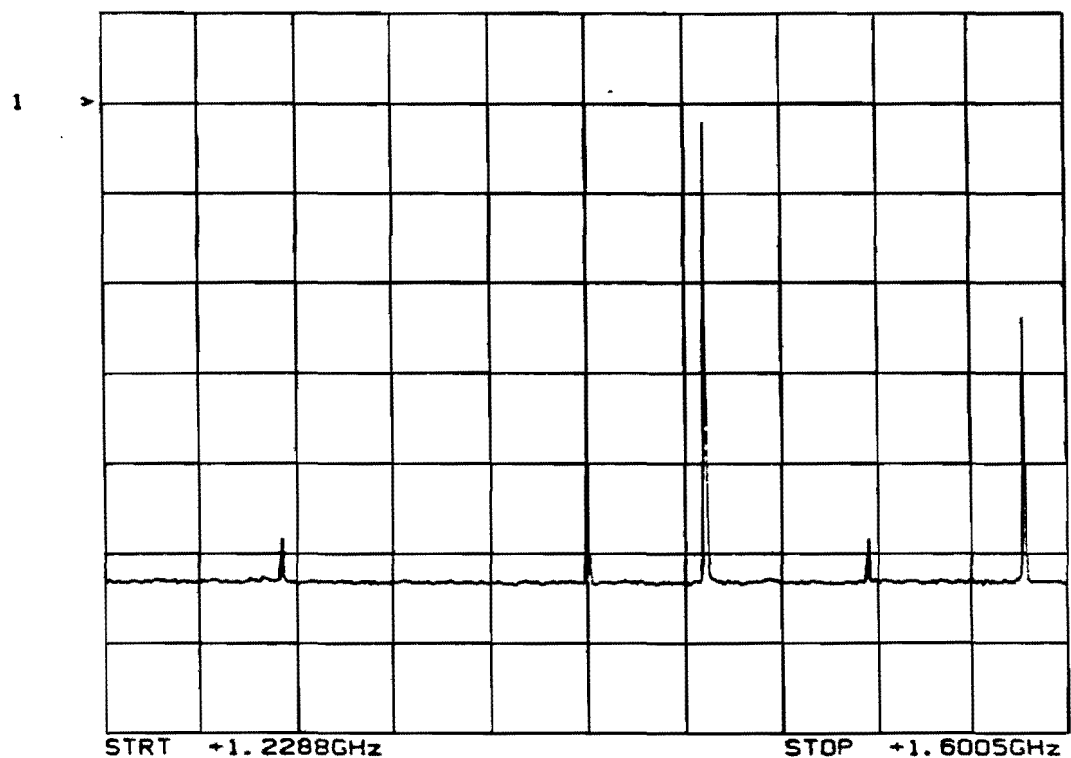
Figure 3.4: Transmission through cavity II on a wide scale.
The modes, from left to right, are the TE_{112}, TM_{010}, TM_{011},
TE_{113}, TM_{012}.

43

3.3 Cavity Q and the Resistivity of Copper

The cavities used in this experiment have been manufactured from a high purity (nominally 99.996%) oxygen free copper alloy 101 OFE-HIT [3] in the interest of high Q. The bulk resistivity of copper decreases dramatically upon cooling to an extent dependent on the level of impurities and the crystal structure. A standard measure of this is the RRR (residual resistivity ratio), the ratio of the DC resistivity at 273 °K to the resistivity at 4.2 °K,

$$RRR = \frac{\rho_{273 \ °K}}{\rho_{4.2 \ °K}} . \qquad (3.5)$$

The manufacturer claims an RRR = 210 for 101 OFE-HIT copper , and we have measured an RRR = 180[4]. The cavity Q at high frequencies, however, is not directly proportional to conductivity because conduction is limited to a surface layer of finite thickness which possesses a surface resistance.

The Q of a cavity mode is defined by[5],

$$Q = \frac{\omega W}{P} \qquad (3.6)$$

where W is the stored energy, P is the power dissipated within the cavity and ω is the angular frequency of the cavity mode. W, in mks units, can be expressed as,

$$W = \frac{1}{2 \mu} \int \mathbf{B} \cdot \mathbf{B} \ dV \qquad (3.7)$$

where the integration is over the cavity volume and μ is the permeability inside the cavity. If one assumes that all losses in the cavity are due to the finite conductivity of the cavity walls then the power dissipated is

$$P = \frac{R_s}{2\mu_{wall}^2} \int B_t \cdot B_t \, dS \qquad (3.8)$$

where the integral is over the surface of the cavity, μ_{wall} is the permeability of the cavity wall, R_s is the surface resistance, and B_t is the tangential magnetic field at the cavity surface. Consequently, the expression for the cavity Q can be written,

$$Q = \frac{\omega A}{R_s} \qquad (3.9)$$

where A is a calculable constant dependent on the cavity geometry and the mode under consideration.

Calculating the expected Q of a cavity is therefore a problem of determining the surface resistance of a material, given the cavity dimensions and mode under consideration. At room temperature, the surface resistance of copper is determined by the classical skin effect[6]. The surface resistance can be related to the DC resistivity and the skin depth through,

$$R_s = \frac{\rho}{\delta} \qquad (3.10)$$

where ρ is the DC resistivity, and δ is the skin depth, the distance fields and induced currents penetrate into a conductor (at a particular frequency). The classical skin depth is given by,

$$\delta = \frac{\sqrt{2\rho}}{(\omega \; \mu_{wall})^{1/2}} \; .$$

(3.11)

The $f^{-1/2}$ dependance of the skin depth results in an $f^{1/2}$ dependance of surface resistance at room temperature. This can be seen in figure 3.5. Using $\rho(273) = 1.55 \times 10^{-8}$ Ωm for copper we find that $R_s = 7.6 \times 10^{-3}$ Ω (f/1 GHz)$^{1/2}$, which is in reasonable agreement with the data.

As the temperature decreases so does the resistivity, but for sufficiently low temperatures, the skin depth is no longer described by the classical skin effect. In this anomalous skin effect limit, the mean free path, ℓ, of the conduction electrons becomes longer than the classical skin depth and the classical assumption of diffusive electron flow (equation 3.11) is no longer valid. The departure of the resistivity from the classical model can be characterized by the dimensionless parameter,

$$\alpha = \frac{3}{4} \; \mu_0 \; \omega \; (\ell\rho)^2 \; \rho^{-3}.$$

(3.12)

For $\alpha < 0.02$ equation 3.11 is valid and for $\alpha > 3$ the surface

Surface Resistance vs. Frequency
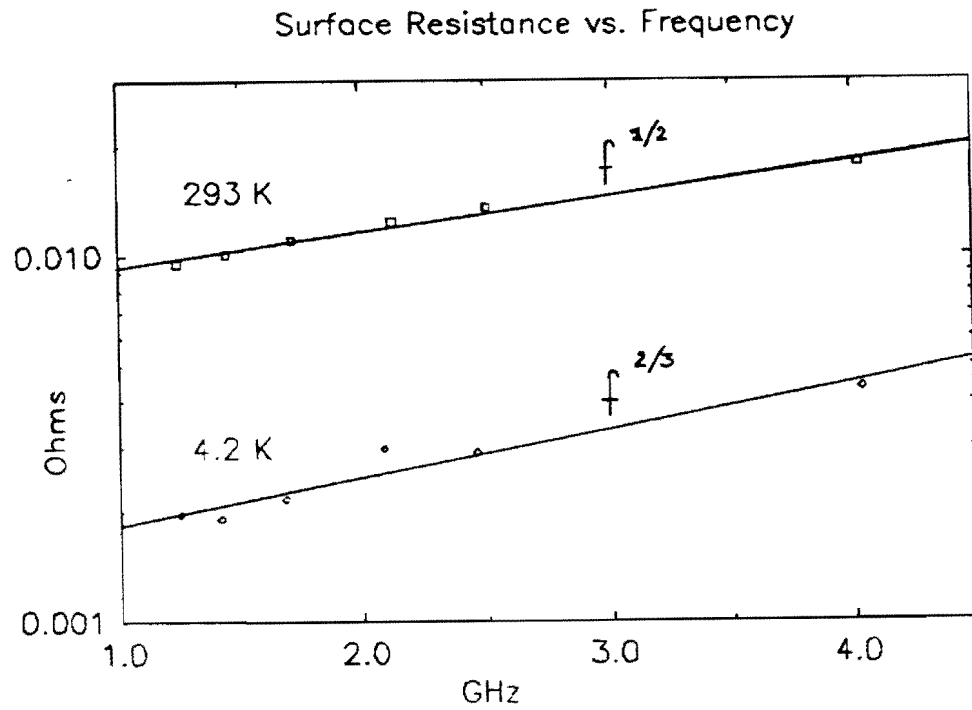
Figure 3.5: R_S for a number of cavities of different resonant frequencies. R_S is calculated from a measured Q of the TM_{010} mode. The upper trace shows the room temperature $f^{1/2}$ dependence and the lower trace shows the 4.2 °K $f^{2/3}$ dependence.

resistance is well represented by

$$R_S = R_\infty (1 + 1.157 \, \alpha^{-0.276}) \qquad (3.13)$$

where

$$R_\infty = \left[\sqrt{3}\pi \left[\frac{\mu_0}{4\pi} \right]^2 (\ell\rho) \, \omega^2 \right]^{1/3} . \qquad (3.14)$$

$(\ell\rho)$ is a property of the material, independent of purity, temperature or frequency; for Copper $\ell\rho = 6.6 \times 10^{-16}$ Ωm^2. On the other hand, α is temperature and impurity dependent through the ρ^{-3} term. It follows that R_S is temperature and impurity dependent. Figures 3.6a and b show the temperature dependance of R_S from measurements of cavity Q for two different cavities. In addition, from equations 3.13 and 3.14 one can see that $R_S \sim f^{2/3}$ in the anomalous skin effect limit. This can also be seen in the lower trace of figure 3.5.

3.4 Tuning

To search for axions of an unknown frequency requires that the resonant frequency of the cavity be tuneable. As can be seen from equation 3.1 and figure 3.1, the frequencies of most resonant modes in a right circular cylindrical cavity depend on both the length and the diameter of the cavity. However, the resonant frequency of the TM_{010} mode, the mode of interest, depends only on the cavity

48

Surface Resistance vs. Temperature
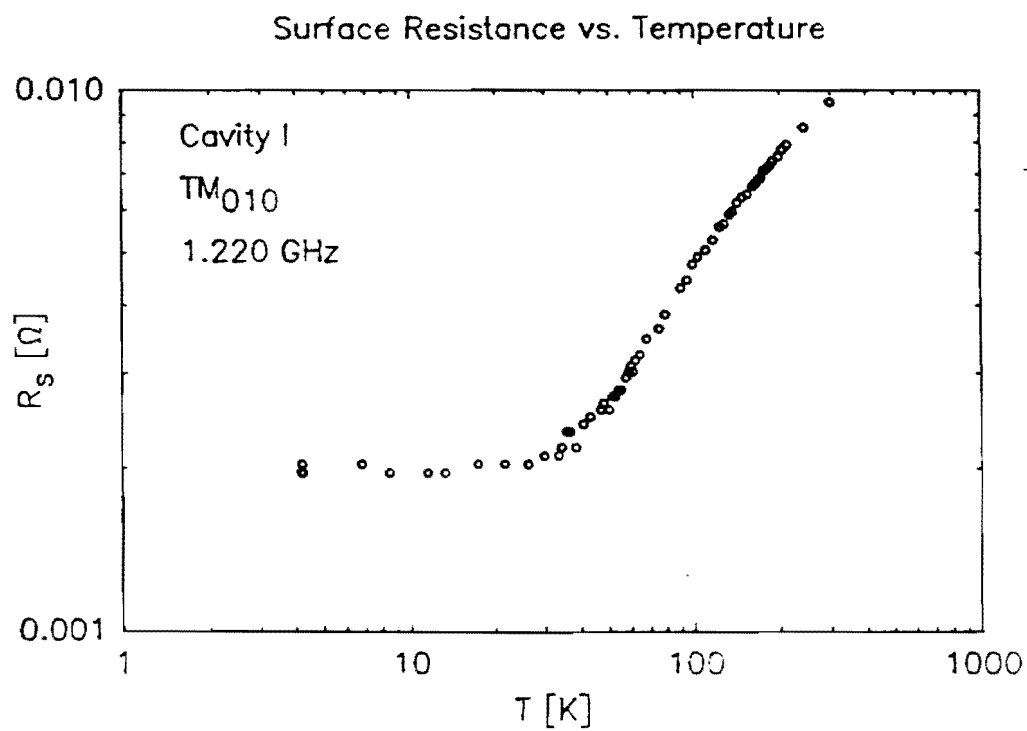
Figure 3.6a: R_S vs. temperature for cavity I, TM_{010} mode.

Surface Resistance vs. Temperature
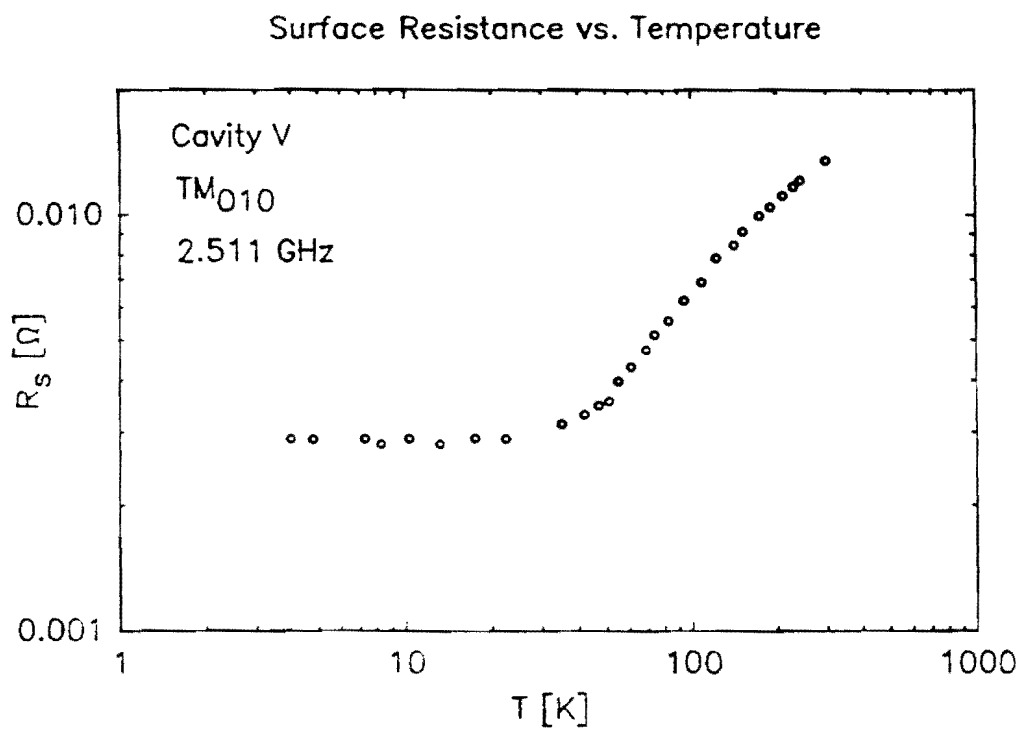
Figure 3.6b: R_S vs. temperature for cavity V, TM_{010} mode.

diameter, not length. Changing the resonant frequency of the TM_{010}
mode by mechanically changing the cavity diameter (while maintaining
a high Q) seems not to be practical. We have instead decided to tune
the TM_{010} mode by introducing a circular cylindrical dielectric rod
along the central axis of the cavity, as shown in figure 3.2.
Introducing a dielectric into an empty cavity effectively increases
the volume of the cavity, decreasing the resonant frequencies. If,
for example, the cavity were completely filled with a material of
dielectric constant ϵ all resonant frequencies would decrease by a
factor $\epsilon^{1/2}$. Partially filling the cavity is more complicated, of
course, and the exact amount the cavity tunes depends on the rod
diameter, the distance the rod has been inserted, the dielectric
constant of the rod, and the mode field geometry. The high electric
fields of the TM_{010} along the central axis produce a large tuning of
the mode. Continuous frequency tuning is accomplished with the
dielectric rod by varying the insertion of the rod into the cavity.
High rod to cavity diameter ratios and increased rod dielectric
constant result in increased tuning ranges. We have used sapphire
because it has a high dielectric constant, $\epsilon = 10$, and extremely low
microwave losses, with a loss tangent of less than 10^{-9} at 4 °K [7].
The rods were manufactured by Sapphicon Inc.[8].

Figure 3.7 is an example of the measured change in frequency
produced by inserting a .585 inch diameter sapphire rod into a
cavity II. We have compared the experimental results with the
results of a computer calculation using the program URMEL-T written

51

FREQUENCY vs ROD POSITION
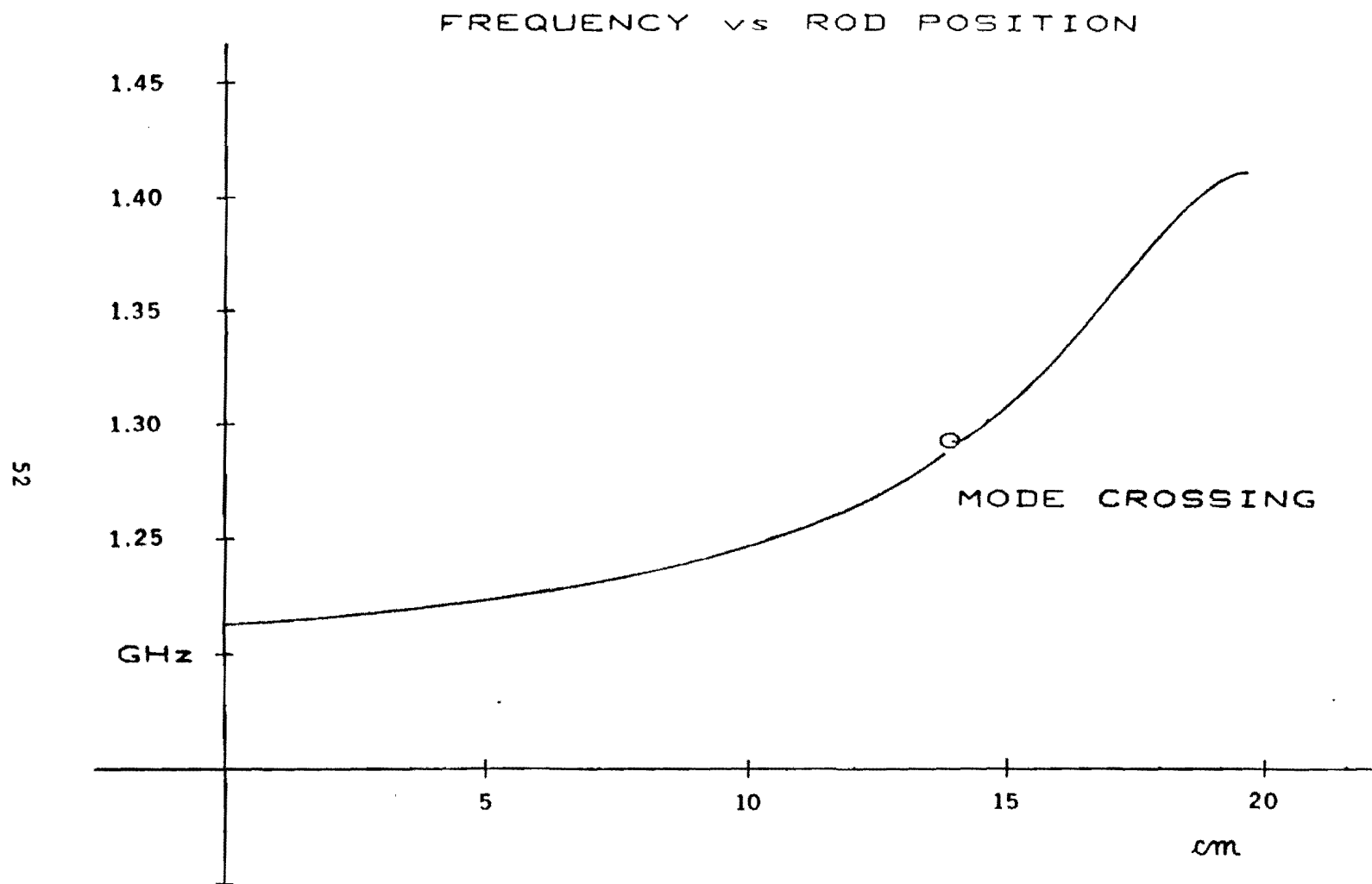
Figure 3.7: Frequency vs. rod position for cavity II, .585 rod.

by T. Weiland et. al. of DESY Laboratory[9]. URMEL-T calculates the frequencies and field configurations of resonant modes in systems with azimuthal symmetry. The results of URMEL-T for the dielectric rod tuning are generally in good agreement with the observed data as shown in figure 3.8. Field configurations generated by URMEL-T are also used for determining G_j^2 as a function of dielectric rod insertion and the calculation is performed for each cavity/rod combination. Figure 3.9 shows the results of the calculation for cavity II, .585 rod.

Despite the need for large tuning ranges, an arbitrarily large diameter sapphire rod cannot be used because it is important not to introduce microwave losses by coupling power out of the cavity through the sapphire rod. The tuning rod is introduced into the cavity through a 2.75 inch long copper tube with an inside diameter approximately .030 inches larger than the rod itself. Rods of .250, .385 , and .585 inch diameters have been used. The tube, and consequently the rod as well, must have a diameter such that the cutoff wavelength of the lowest circular wave guide mode is sufficiently below the free-space wavelength of the cavity mode. The lowest mode in a circular waveguide is the TE_{11} mode which, when filled with a material of dielectric constant ϵ, has a (free space) cutoff wavelength equal to,

$$\lambda_c = \sqrt{\epsilon} \; \frac{\pi \; d}{1.841} \qquad (3.14)$$

53

URMEL-T for cavity #2 with 0.6" rod
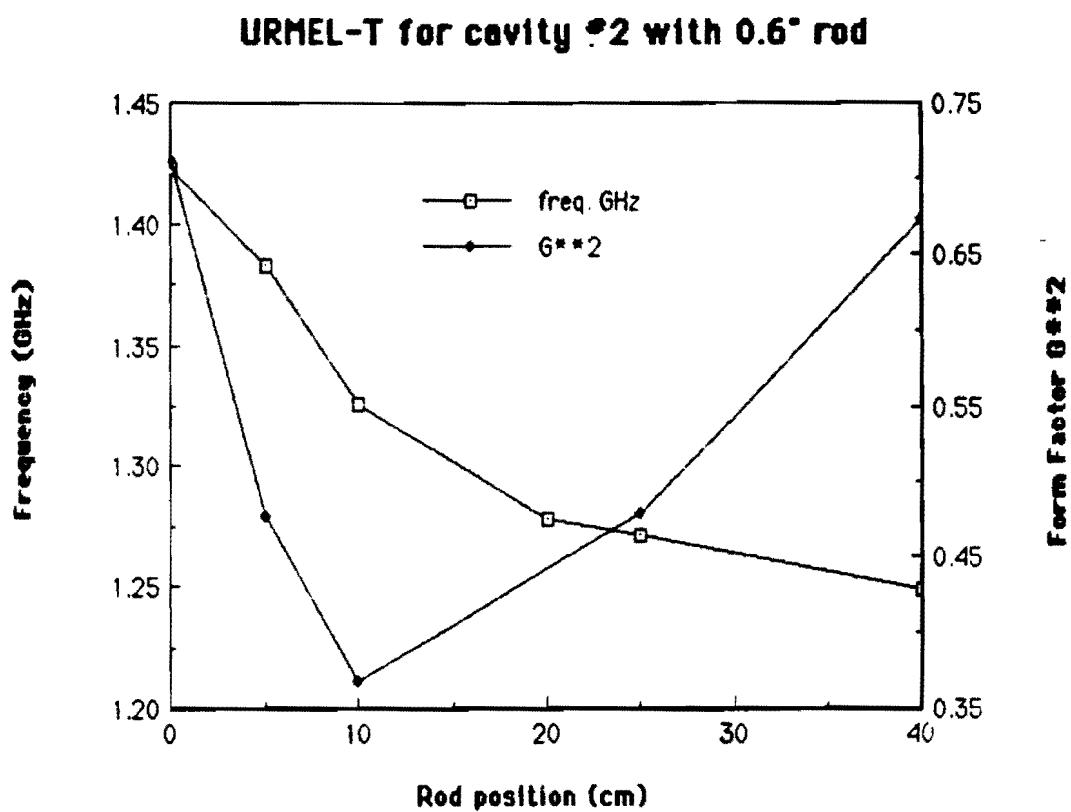
Figure 3.8: Frequency and G_j^2 vs. rod position for cavity II, .585 rod, as calculated by URMEL-T.

54

URMEL-T for cavity #2 with 0.6" rod
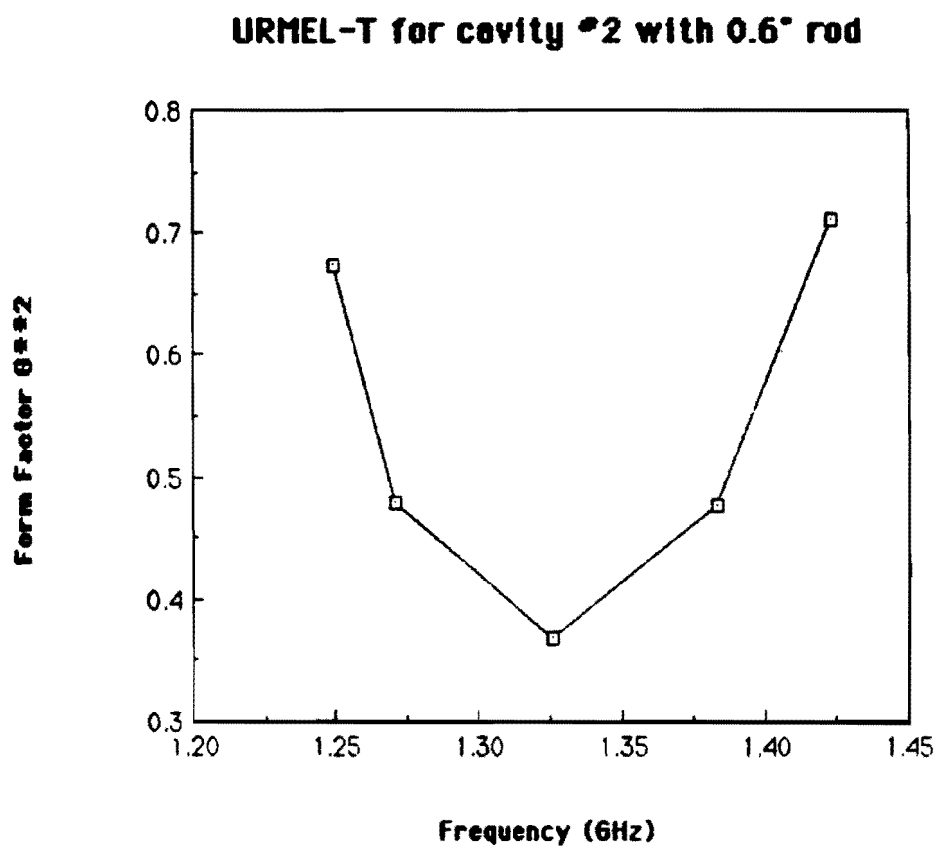
Figure 3.9: G_j^2 vs. frequency for cavity II, .585 rod, as calculated by URMEL-T.

where d is the diameter of the wave guide. The attenuation of the electric field is given by[10],

$$\alpha = 8.69 \ \epsilon \left[\left(\frac{2\pi}{\lambda_c} \right)^2 - \left(\frac{2\pi}{\lambda} \right)^2 \right]^{1/2} dB/cm. \qquad (3.15)$$

Where λ_c is the cutoff wavelength, and λ is the wavelength (in cm) in free space at the frequency of excitation, and ϵ is dielectric constant of the rod. Written in terms of frequencies,

$$\alpha = 1.82 \times 10^{-9} \ \epsilon \ (f_{cut}^2 - f^2)^{1/2} \ dB/cm \qquad (3.16)$$

where f_{cut} is the cutoff frequency of the empty wave guide.

From practical experience, however, one sees a deterioration in the cavity Q when the rod is partially inserted which is not related to α in any simple way. The effect depends on the rod insertion, is largest when the rod is inserted only about 1/5 of the length of the cavity, and disappears when the rod is completely inserted. We have not been able to explain the deterioration in Q quantitatively. However it may be that the increased asymmetry in the z-axis and consequent introduction of radial components of the electric fields increases the coupling of the cavity modes to the waveguide modes. Figure 3.10 shows the change in Q as a function of frequency for cavity IV with the .400 inch diameter sapphire rod (the graph is also a plot of Q vs. rod position but the relationship between frequency and position is not linear). Figure 3.11 shows the degradation in Q as a function of α for a variety of different rod cavity

56
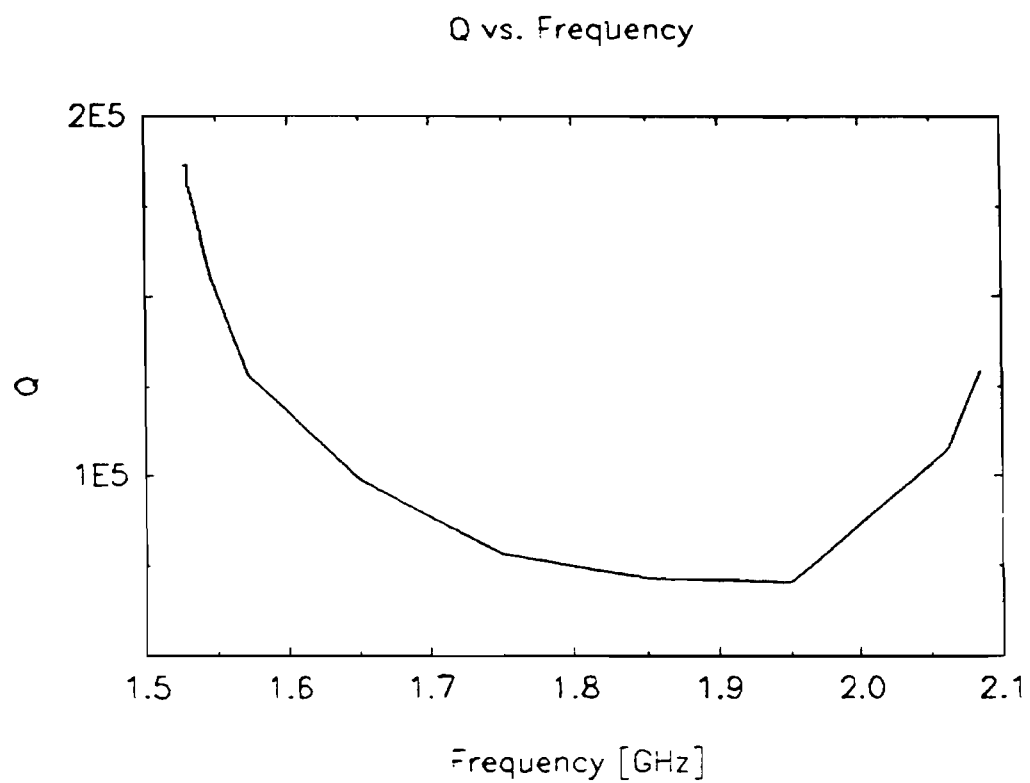
Q vs. Frequency

Figure 3.10: Q as a function of frequency for cavity III, .400 inch rod.

ΔQ vs. α
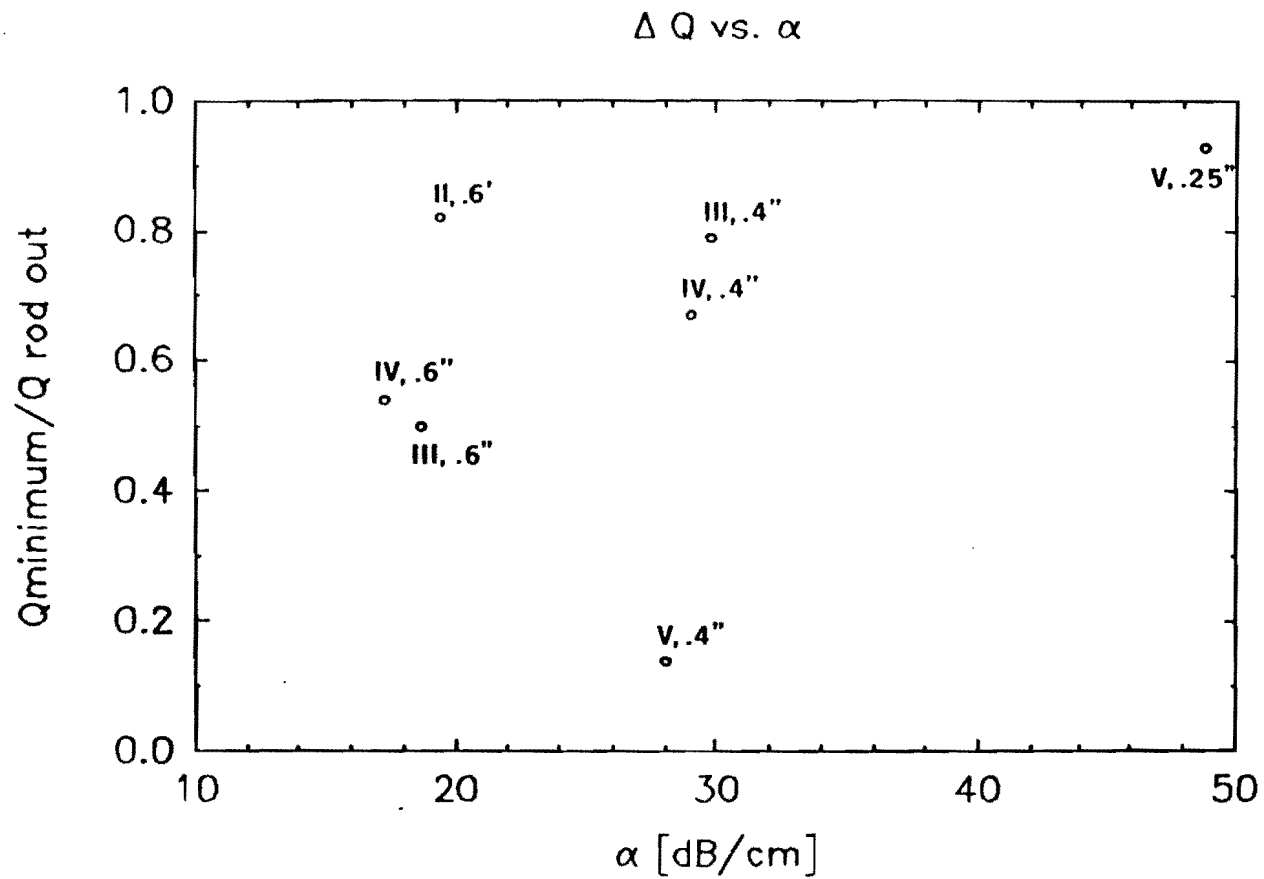
Figure 3.11: Minimum Q divided by Q with the rod out as a function of α. The labels on the data points represent cavity number and rod diameter.

combinations. Because of the deterioration in Q we have used different diameter sapphire rods with the different cavities. A rod diameter is chosen which gives an acceptable decrease in Q for each cavity. Table 3.3 shows all of the cavity rod combinations which have been used and their full tuning ranges. The tuning range is typically limited to 10 - 15% of the untuned frequency.

Although the TM_{010} mode tunes significantly because the electric field of the mode is high in the region of the dielectric rod, other modes with different electric field configurations tune very little. This causes the TM_{010} mode to tune through other modes as the rod is withdrawn from the cavity. As a mode becomes degenerate with another mode a mixing between the two modes occurs. As a result, the frequencies of the modes never actually cross. Instead each resonance takes on the characteristics of the other mode through the crossing. This occurs in direct analogy with energy level crossings in quantum mechanics. A plot of the resonant frequencies of the crossing of two modes is shown in figure 3.12. Because the resonances do not cross, a section of frequency is not covered. The TM_{010} mode in our cavities crosses between one and three other modes, depending on the aspect ratio of the cavity, within its tuning range. The TM_{020} crosses many more modes in its tuning range because of the increased density of modes at the higher frequencies. The cumulative effect of the missed frequencies and the complication of keeping track of the correct mode during data taking have convinced us that the TM_{020} mode is not usable for the axion search.

Cavity Number	Diameter [inches]	Sapphire Rod Diameter [inches]	Frequency Max/Min [Ghz]
I	7.250	.585	1.218 1.090
II	6.250	.585	1.415 1.218
III	5.250	.400	1.685 1.513
		.585	1.685 1.333
IV	4.250	.400	2.087 1.761
		.585	2.087 1.528
V	3.600	.250	2.460 2.239
		.400	2.460 1.952
VII	2.250	.187	3.932 3.361
		.250	3.932 3.048

Table 3.3:   The tuning ranges of the TM_{010} mode for various cavity-rod combinations
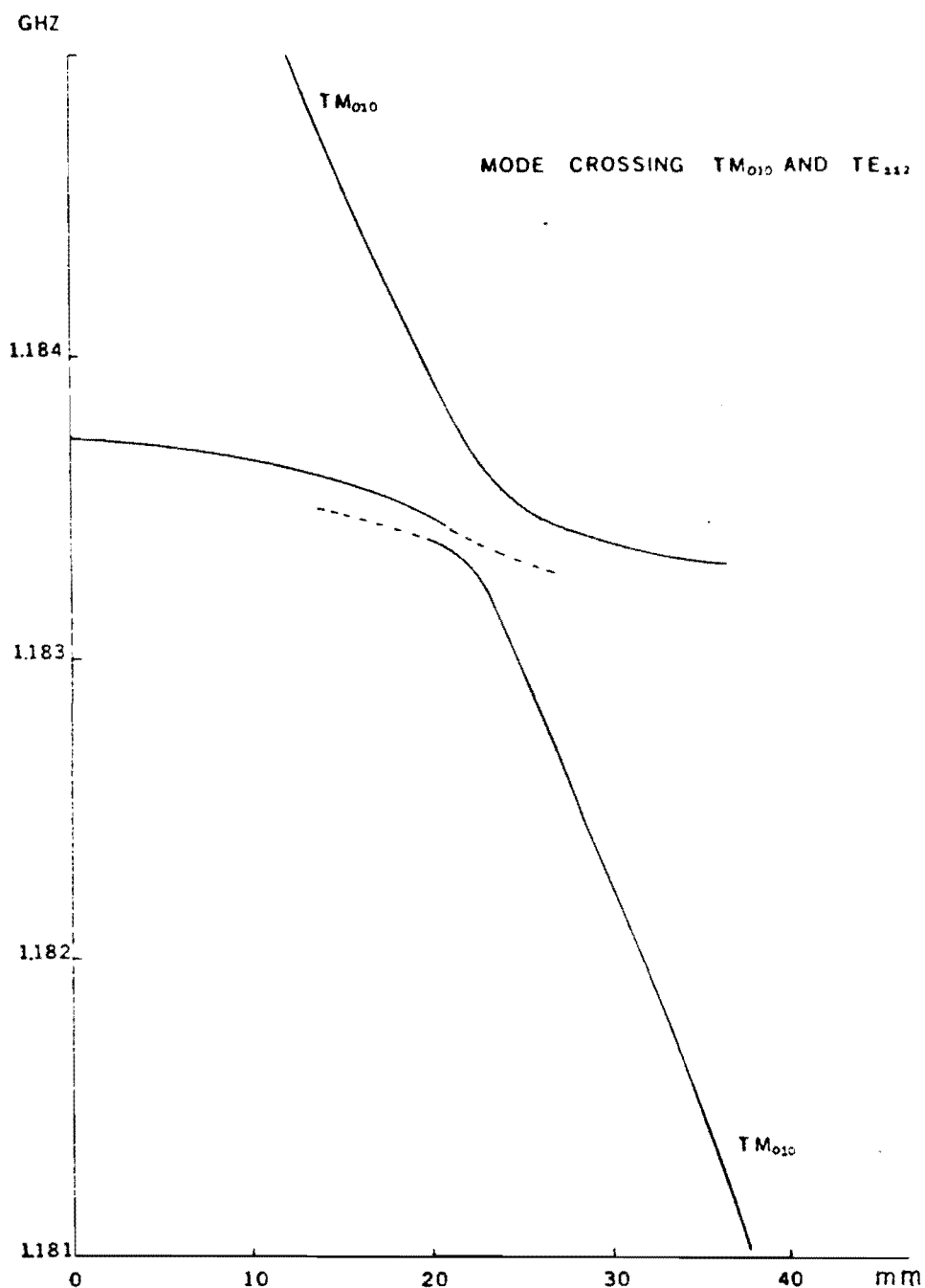
Figure 3.12: The frequency crossing of the TM_{010} mode with the TE_{112} mode when tuning with the sapphire rod. The break in the lower trace is caused by the appearance of both polarizations of the TE_{112} mode split in frequency by the presence of the coupling ports.

61

3.5 Manufacture

The right circular cylindrical geometry of the cavities results in a rather simple design. The cavity is constructed from three main pieces: a tube with inner diameter given by equation 3.1, and two end plates which are attached to either end of the tube with low resistance joints. The method of end plate attachment, the tuning rod holding mechanism, and the coupling probe positions and sizes are the only features which must be specified. For reference, figure 3.2 shows the basic cavity design.

In order to maximize the Q it is important to create as smooth an inside cavity surface during manufacture as possible. The finish left in copper by standard machining processes, including honing, is not satisfactory. A very nice finish can be achieved by electropolishing the copper using a commercially available product, called Electroglo[11]. The cavity tube and end plates are electropolished before assembly. Electroglo is mixed with phosphoric acid in a ratio of 1:3 by volume. A copper cathode is manufactured to be as large as possible and everywhere equidistant from the piece which is being polished. Current passes from the work (the anode, + on the power supply) through the electropolishing solution to the cathode. The current densities are typically on the order of 2×10^{-2} A/cm^2 with voltage drops of approximately 3 to 5 volts, depending on anode and cathode size. This results in material removal rates of 10^{-4}

inches/10 minutes. Electropolishing is quite effective in making the surface smooth, as it preferentially removes material from sharp corners: areas where the applied electric field is strongest.

The configuration of the magnetic fields of the TM_{010} mode results in induced currents in the cavity walls which are vertical in the cavity cylinder, cross to the end plate and flow radially in the end plate. Because the currents pass from the cavity tube to the end plates, a separate piece of copper, it is important for good Q that this joint have as low a resistance as possible. We have used two different designs for this joint. The first is based on electron beam welding and is shown graphically in figure 3.13[12]. We have chosen to use electron beam welding rather than a more conventional form of welding because it is quite reproducible, results in relatively little material deformation due to heating (a problem in a high heat conductivity material like copper), and because electron-beam welding produces no noticeable oxidation of the copper surface. This feature is important as it is much simpler to prepare the cavity surfaces before welding.

We have also successfully tested a second joint design whose underlying idea is very simple; firmly pushing two very clean pieces of copper together results in a joint of very low resistance. Figure 3.14 shows the basic design. Cavity VII has been manufactured in this way and has yielded results equivalent to the welded design. This

.125

Cavity wall

Interference fit

.031

E-Beam

.187

.156

End plate

Figure 3.13: Cross section of the cavity tube/end-plate electron beam weld.

Figure 3.14: End-plate attachment method with flanges.

can be seen in figure 3.5 where cavity VII is the right most data point. Losses in the joint between the cavity tube and the end-plates would be seen as increased surface resistance above the changes caused by the skin effect. The data are consistent with the other cavities at both 293 °K and 4.2 °K. The obvious advantages of this design is its simplicity of manufacture and the access to the inside of the cavity after assembly. The primary disadvantage of this end plate attachment technique is that the flanges increase the outside diameter of the cavity. This becomes a problem at lower frequencies when such cavities become to large to fit inside the magnet.

Connected to one end plate of the cavity is the copper tube through which the tuning rod is introduced into the cavity. The tube diameter is maintained for 2.75 inches at which point the tube expands into an area which contains a bearing assembly as shown in figure 3.15. The purpose of this bearing assembly is to capture the sapphire rod and keep it aligned with the axis of the cavity while allowing the rod to be inserted and withdrawn smoothly from the cavity. Any vibrations which can cause angular deflections of the rod result in an instability of the cavity frequency as the end of the rod moves from the highest field along the central axis of the cavity to the slightly lower fields off to the side. The bearing cannot be of arbitrary length because this would require the use of longer tuning rods. The bearing assembly must also allow a smooth retraction of the rod during data taking. A cavity width of tuning

cavity top-plate

wavey washer

teflon bearings

positioners

sapphire rod

2.75

rod bearing housing

Figure 3.15: Rod bearing mechanism.

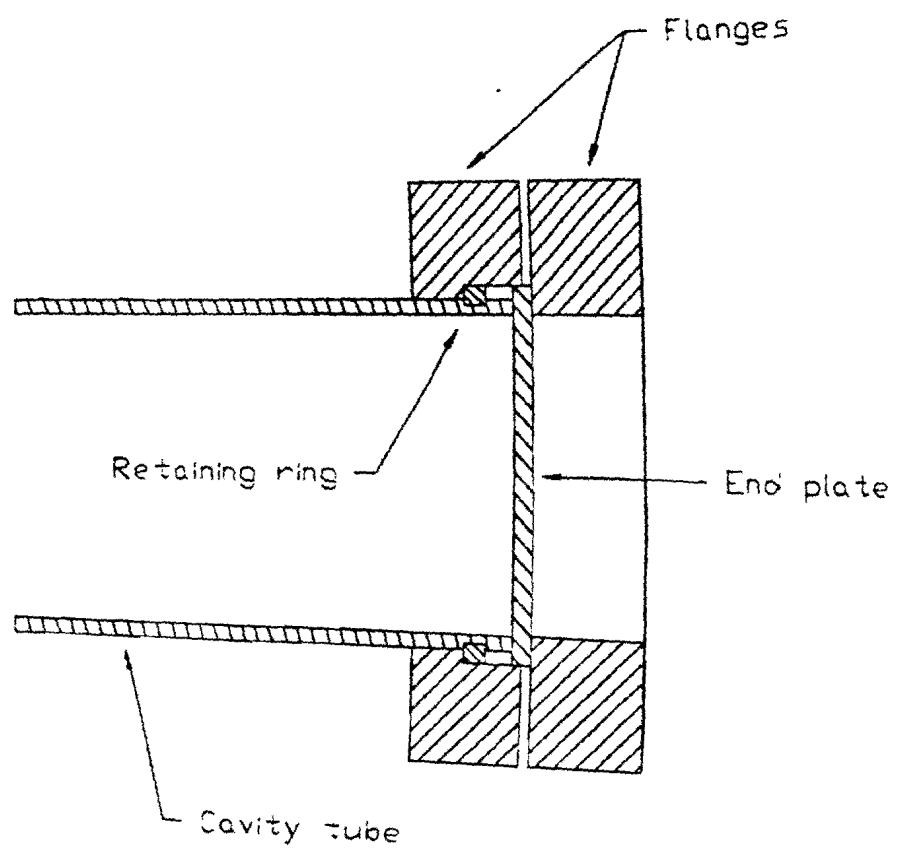**Figure 3.13:** Cross section of the cavity tube/end-plate electron beam weld.

Figure 3.14: End-plate attachment method with flanges.

can be seen in figure 3.5 where cavity VII is the right most data point. Losses in the joint between the cavity tube and the end-plates would be seen as increased surface resistance above the changes caused by the skin effect. The data are consistent with the other cavities at both 293 °K and 4.2 °K. The obvious advantages of this design is its simplicity of manufacture and the access to the inside of the cavity after assembly. The primary disadvantage of this end plate attachment technique is that the flanges increase the outside diameter of the cavity. This becomes a problem at lower frequencies when such cavities become to large to fit inside the magnet.

Connected to one end plate of the cavity is the copper tube through which the tuning rod is introduced into the cavity. The tube diameter is maintained for 2.75 inches at which point the tube expands into an area which contains a bearing assembly as shown in figure 3.15. The purpose of this bearing assembly is to capture the sapphire rod and keep it aligned with the axis of the cavity while allowing the rod to be inserted and withdrawn smoothly from the cavity. Any vibrations which can cause angular deflections of the rod result in an instability of the cavity frequency as the end of the rod moves from the highest field along the central axis of the cavity to the slightly lower fields off to the side. The bearing cannot be of arbitrary length because this would require the use of longer tuning rods. The bearing assembly must also allow a smooth retraction of the rod during data taking. A cavity width of tuning
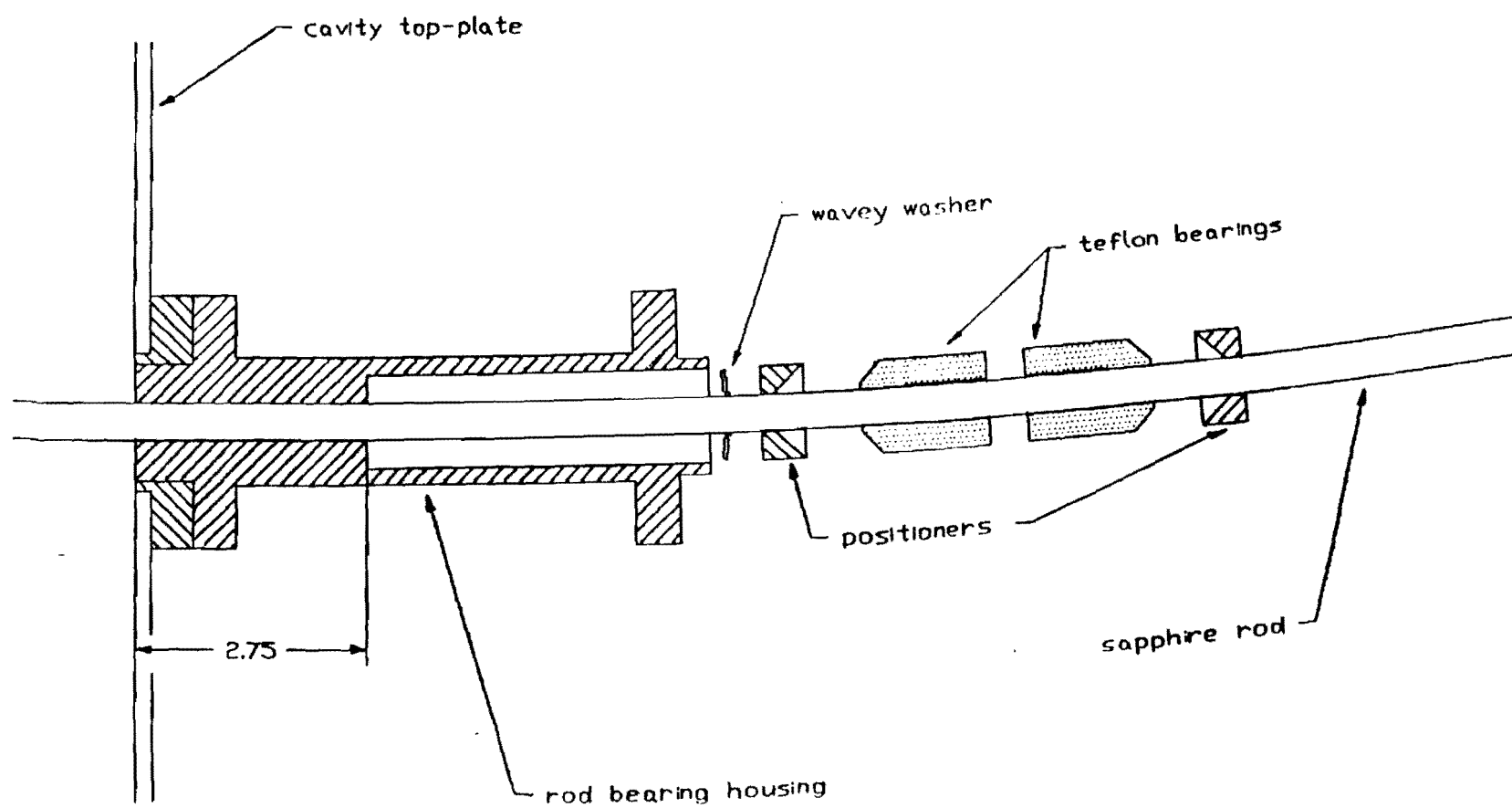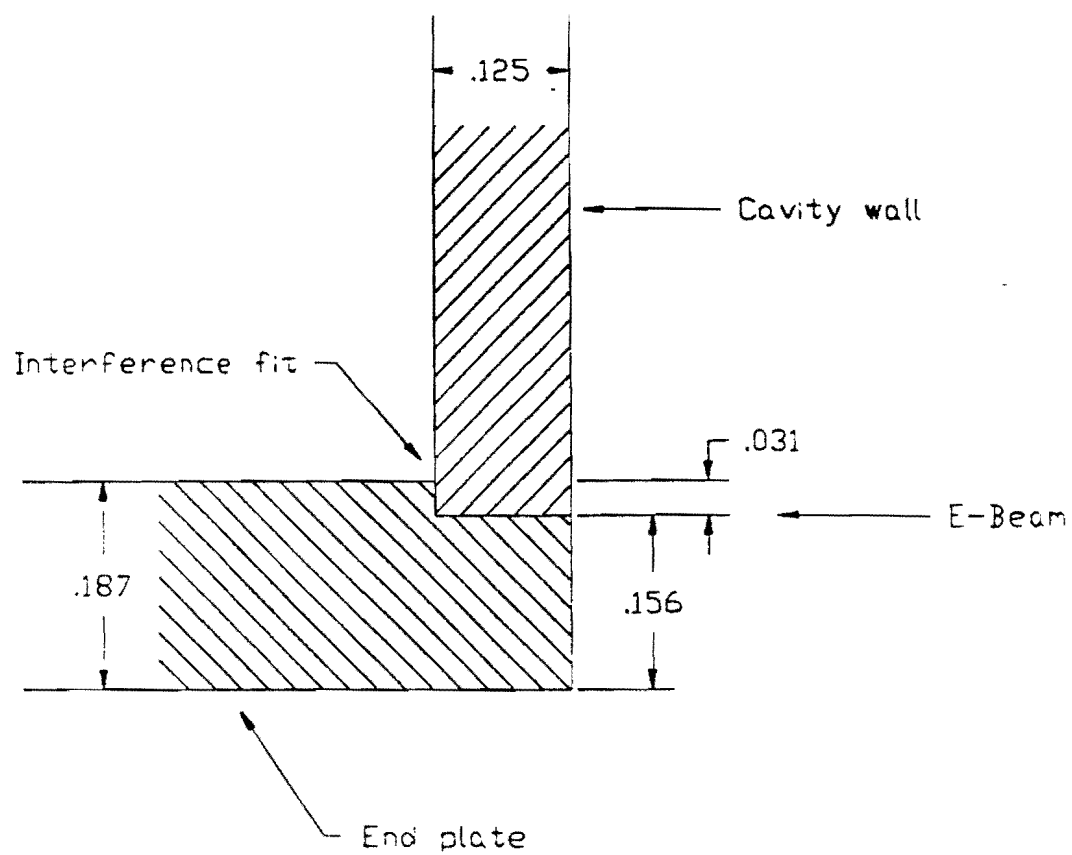
cavity top-plate

wavey washer

teflon bearings

positioners

sapphire rod

rod bearing housing

2.75

67

Figure 3.15: Rod bearing mechanism.

is typically caused by a motion of the order of .001 inches (this number, of course, depends on the tuning curve of the particular cavity and rod combination and the point on the tuning curve). Finally, the bearing assembly is spring loaded to absorb the large contraction of the teflon upon cooling.

The rod is pulled out of the cavity during data taking by a motor drive mechanism which is mounted on the top of the dewar. The heart of the motor drive mechanism is a highly precise machine screw with a thread pitch of 2 mm per turn and a pre-loaded roller nut assembly. The machine screw is turned by a variable speed electric motor whose motion has been geared down by a factor 2,400:1. The motion of the drive mechanism is transferred to the tuning rod by a section of stainless steel tubing. A picture of the motor drive mechanism can be found in figure 3.16. A picture of a cavity mounted on the cryostat insert assembly is shown in figure 3.17.
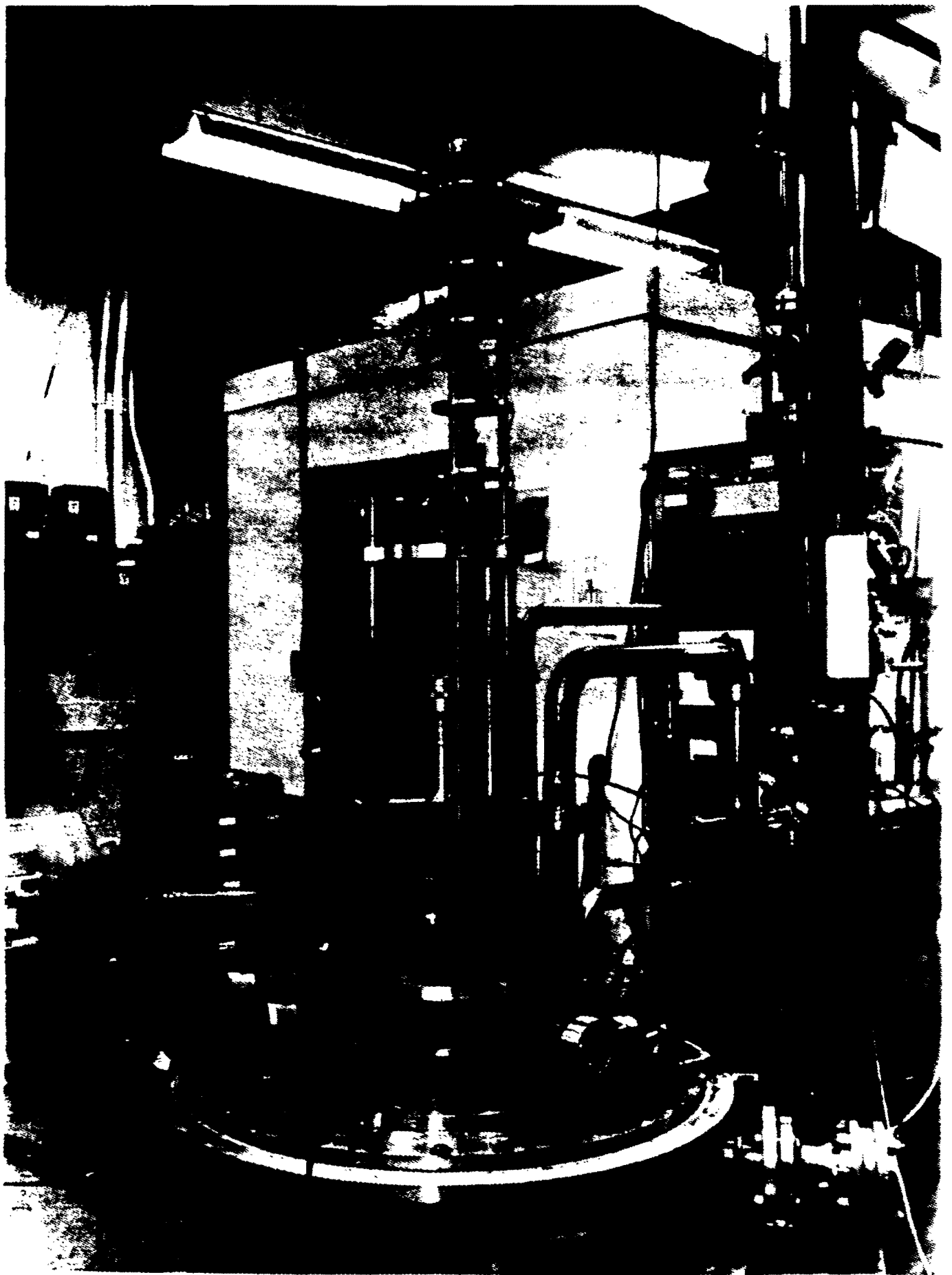
Figure 3.16: Rod drive mechanism.
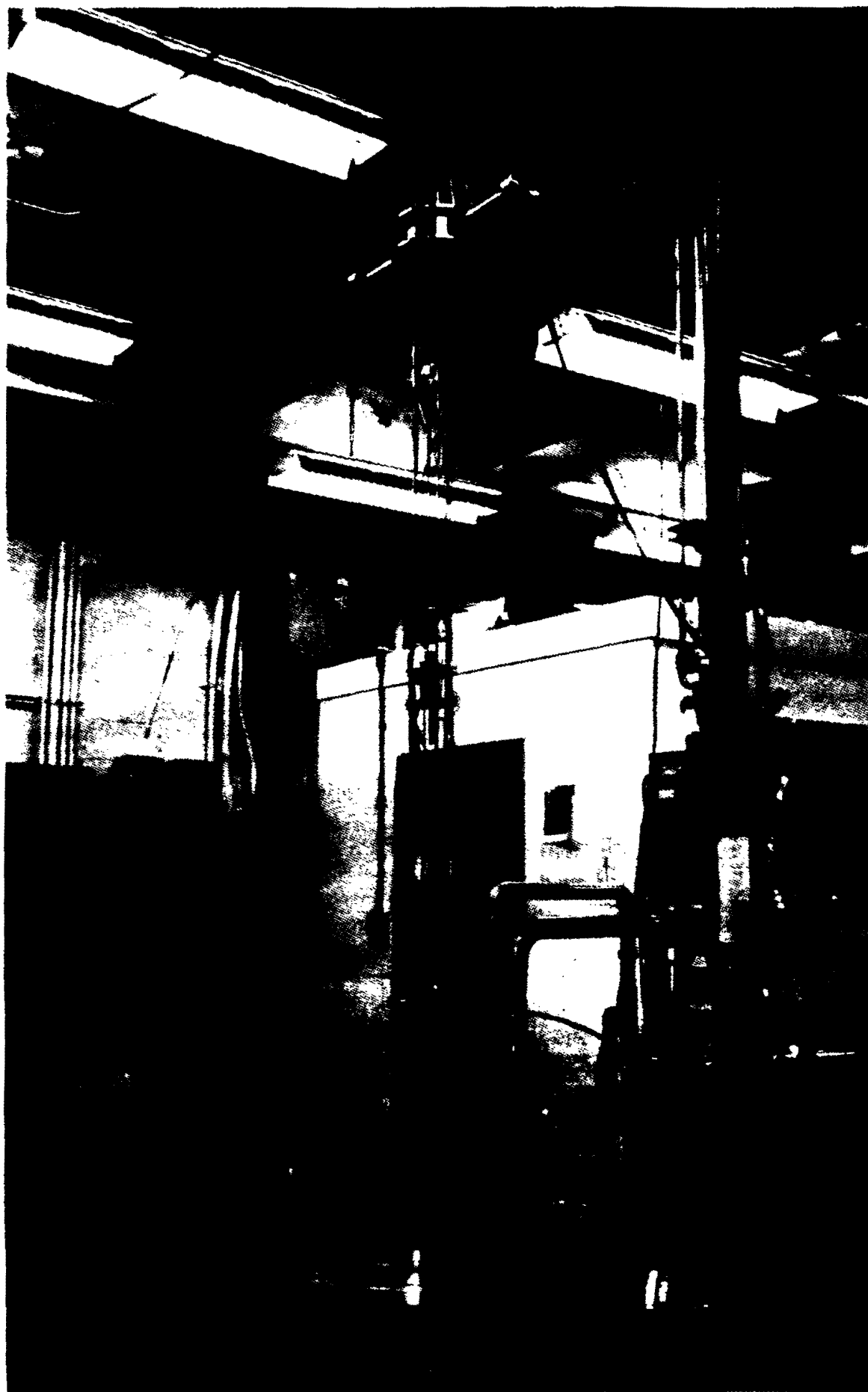
Figure 3.17: Cavity and cryostat mounting assembly.

References

1. Montgomery, Dicke, and Purcell, *Principles of Microwave Circuits*, (Boston Technical Publishers, Lexington, 1964), pp. 297-303.

2. φ, r, and z are standard cylindrical coordinates.

3. Hitachi Ltd: Alloy number c101000FE-HIT oxygen free electronic copper distributed by Copper and Brass Sales, John Dietsch Blvd, North Attleboro, MA 02763.

4. J. Rogers, S. De Panfilis, A. C. Melissinos, B. Moskowitz, Y. Semertzidis, W. Wuensch, H. Halama, A. Prodell, W. Fowler, F. Nezrick, Appl. Phys. Lett. 52 (26), 27 (1988).

5. See for instance W. Smythe, *Static and Dynamic Electricity*, (McGraw-Hill, New York, 1968).

6. H. Hahn and H. Halama, BNL Report AADD-129, January 1967 (unpublished).

7. D. Morris, LBL Report 17915, May 1984.

8. Sapphicon Inc., Milford NH.

9. T Weiland, DESY 86-106, ISSN 0418-9833 (1986).

10. T. Moreno, *Microwave Transmission Design Data*, (Dover, New York, 1948).

11. Electroglo Co., 621 S. Kolmar Ave., Chicago, IL 60624.

12. In electron beam welding the beam should travel into the crack between the two pieces to be welded rather than across it since the region in which the metal melts during welding is very narrow (less than 1/16 of an inch but it depends on beam focusing). The weld penetration is determined by adjusting the electron beam energy, but it is not possible to maintain the penetration to a close tolerance as any irregularities in the crack near the surface result in variation of the depth of the weld. If the beam breaks through the far surface of the metal a very rough line is produced and material is sputtered onto the surrounding surface. For this reason it is best to end the weld in metal and this is why the backing step is included in the design. The step also positions the end plate on the end of the cavity tube. The step does introduce a slight crack to the inside of the cavity, but the effect of this is minimized by creating an interference fit of the end plate with the cavity tube

by cooling the end plate to liquid nitrogen temperature before assembly.

Chapter 4: Detection Electronics

4.1 Introduction

The detection electronics are designed to monitor the microwave power produced by the cavity in the frequency bandwidth of the TM_{010} mode with a resolution approximately equal to the expected axion signal width: 200 to 800 Hz in the frequency range which has been covered by this experiment. As the resonant frequency of the TM_{010} mode is swept, the cavity output is measured, measurements are averaged together, and an extended frequency spectrum is produced. The expected signal, on the order of 10^{-24} W in a 200 to 400 Hz band, is extremely small and demands as sensitive a receiver system as possible. Since the noise performance of the microwave receiver used in this experiment is determined by the noise temperature of the first stage of amplification, an ultra low noise cryogenically cooled microwave preamplifier is used. A cryogenic microwave circulator is used between the microwave cavity and the preamplifier to eliminate the effect the strongly varying impedance of the cavity has on the noise performance of the amplifier. After the cryogenic preamplifier, a room temperature superheterodyne system is used to lower the frequency of the cavity output signal to the frequency band of 20 to 50 KHz. Final detection of the signal, with 200 or 400 Hz resolution, is accomplished using a 64 channel multiplexed filter-detector system. An on line data acquisition computer is used to

average measurements together and reconstruct the extended frequency spectrum. This spectrum, along with various calibration measurements are transferred to a VAX computer for final analysis.

4.2 Cryogenic Preamplifiers

The cryogenic preamplifiers, which have been constructed by our group, are modified versions of a cryogenic, L-band, GaAs FET amplifier designed and built by the National Radio Astronomy Observatory (NRAO) for use in radio telescopes[1]. The original NRAO amplifiers have a 10 to 15 °K noise temperature in the range of 1.2 to 1.7 GHz. A much broader frequency range is required in this experiment, so we have modified the original NRAO design[2] to produce a series of five preamplifiers covering 1 to 2.8 GHz. Each preamplifier typically has a 25% bandwidth which allows the use of a single preamplifier for the entire tuning range of a cavity-rod combination. The noise temperatures and gains of the amplifiers at 4.2 °K are shown in figures 4.1 to 4.5. As an example, the room temperature performance for amplifier 105 is shown in figure 4.6. Figure 4.7 is a graph of the frequency coverage of five preamplifiers.

The cryogenic preamplifiers use three GaAs FET stages in a lumped circuit element design with a stripline input matching network. Figure 4.8 shows a schematic of the circuit design. FETs have a highly reactive input impedance so source inductance is used to allow

Noise Temperature and Gain vs. Frequency, Amp. 101, 4.2 K

Figure 4.1: Preamplifier 101 at 4.2 °K.

Noise Temperature and Gain vs. Frequency, Amp. NRAO, T=4.2

Figure 4.2: Preamplifier NRAO at 4.2 °K.

Noise Temperature and Gain vs. Frequency, Amp. 104, T=4.2
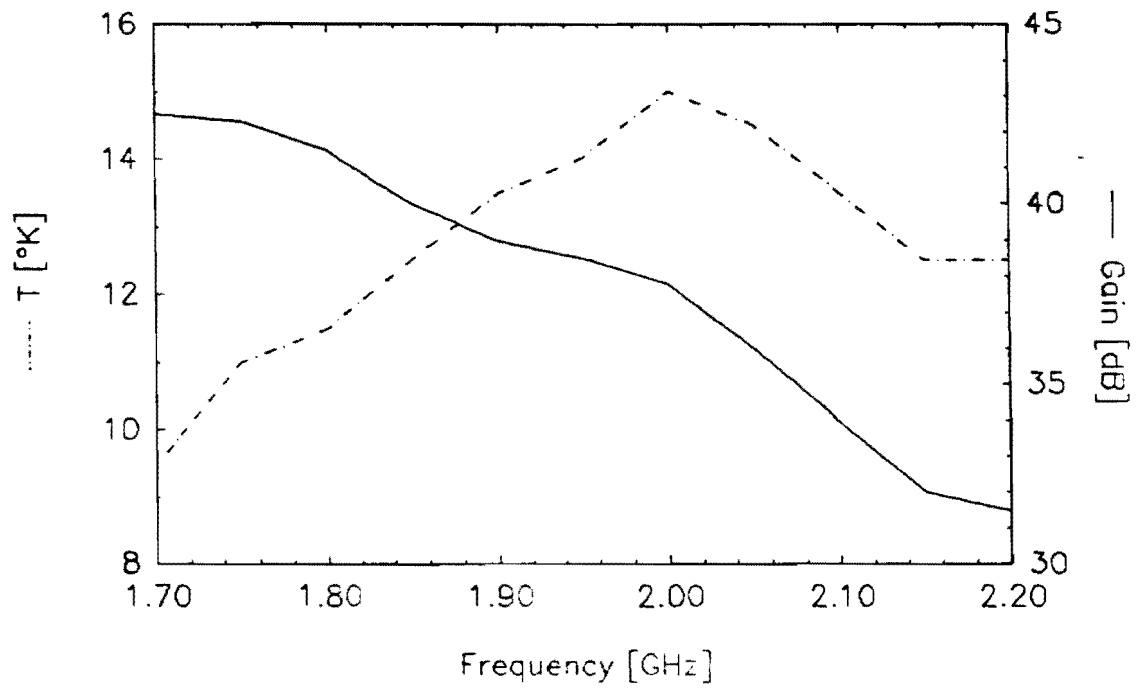
Figure 4.3: Preamplifier 104 at 4.2 °K.

Noise Temperature and Gain vs. Frequency, Amp. 105, T=4.2

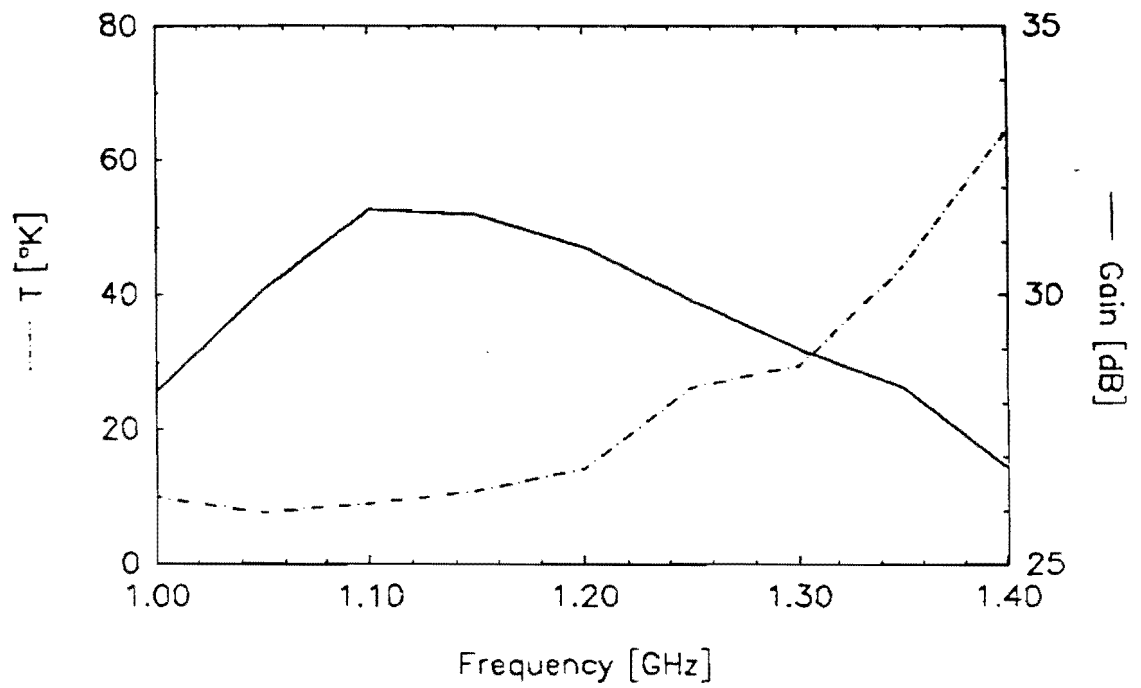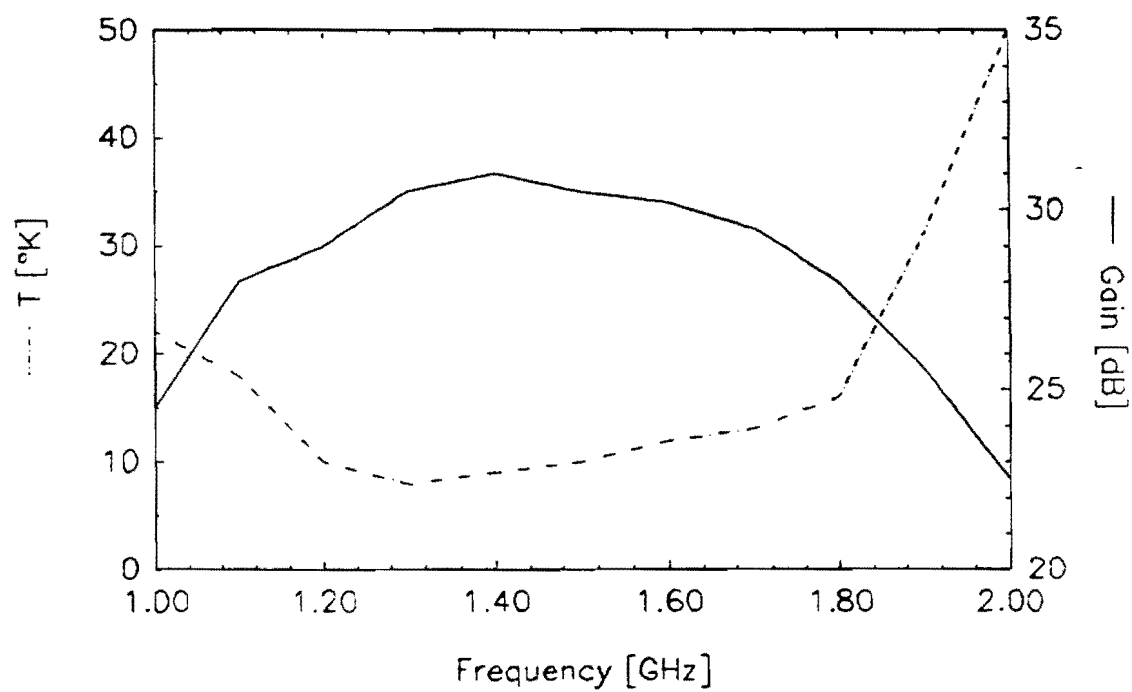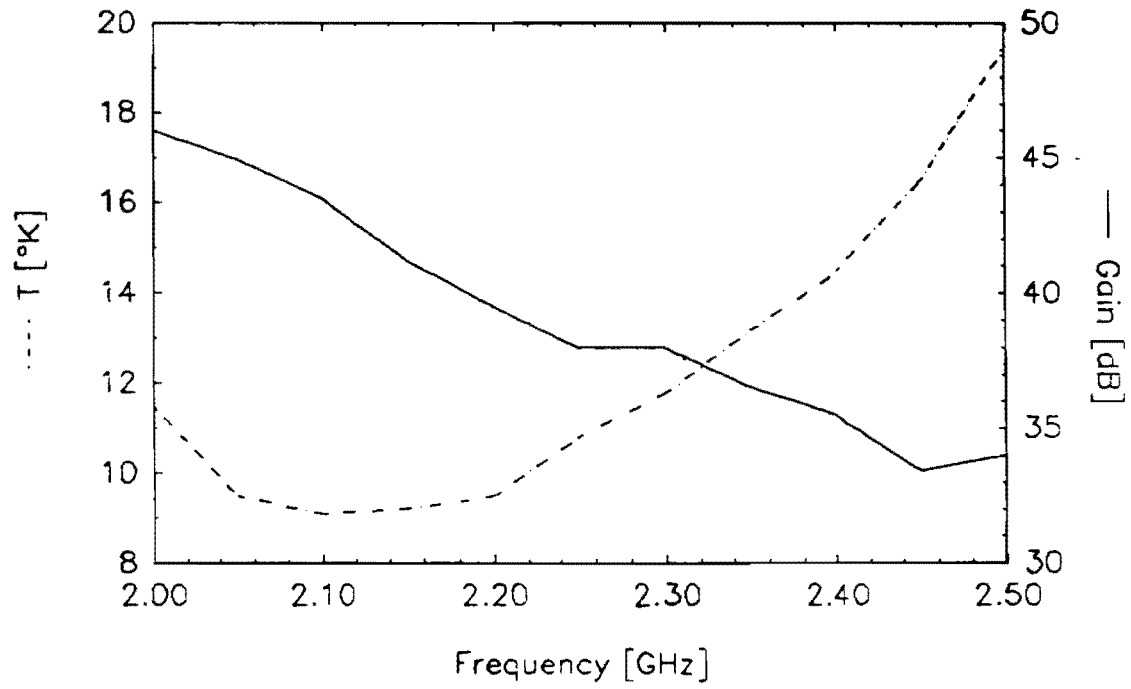Figure 4.4: Preamplifier 105 at 4.2 °K.

Noise Temperature and Gain vs. Frequency, Amp. 103, T=4.2
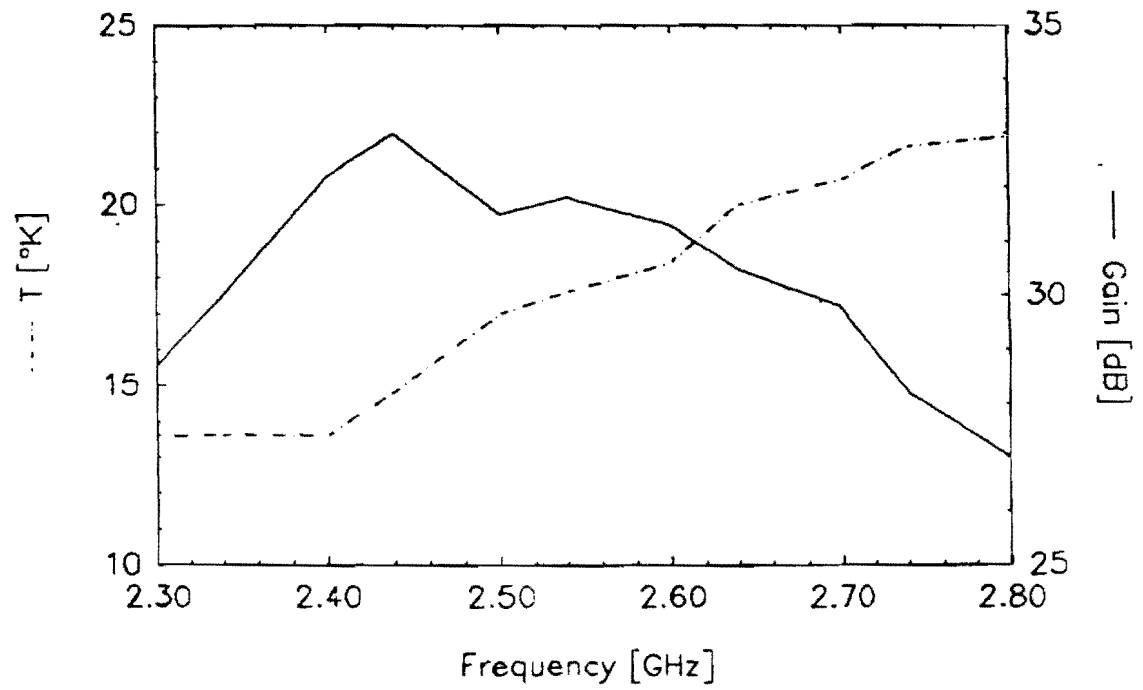
Figure 4.5: Preamplifier 103 at 4.2 °K.

Noise Temperature and Gain vs. Frequency, Amp. 105, T=293
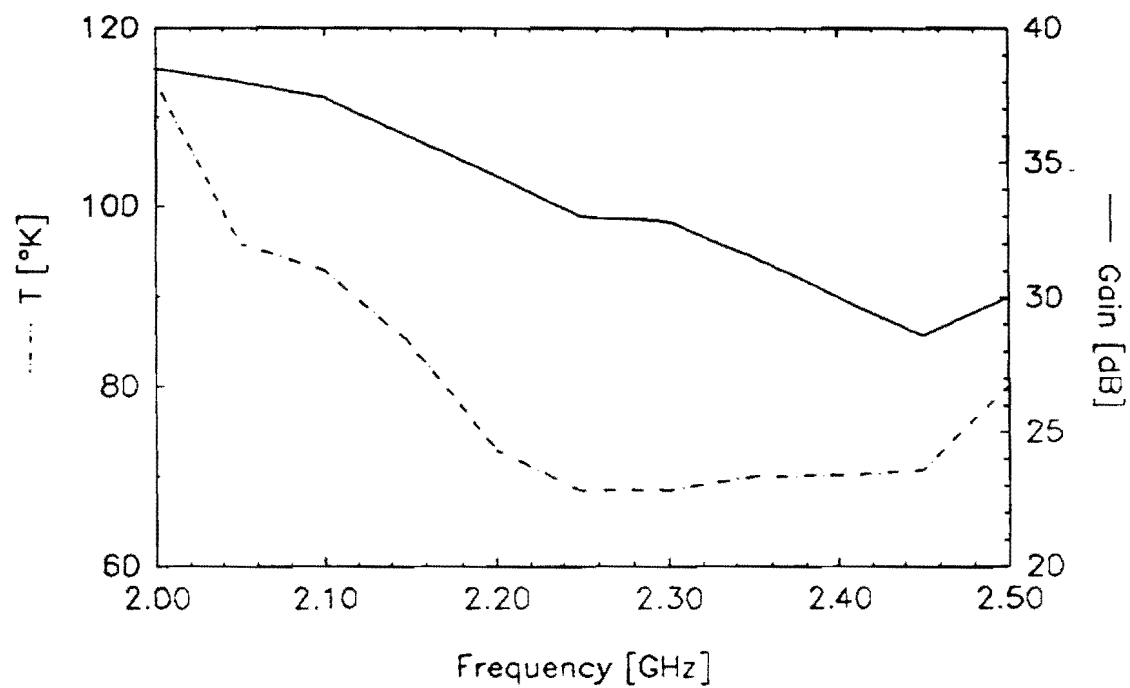
Figure 4.6: Preamplifier 105 at 293 °K.

Frequency Coverage by Amplifier
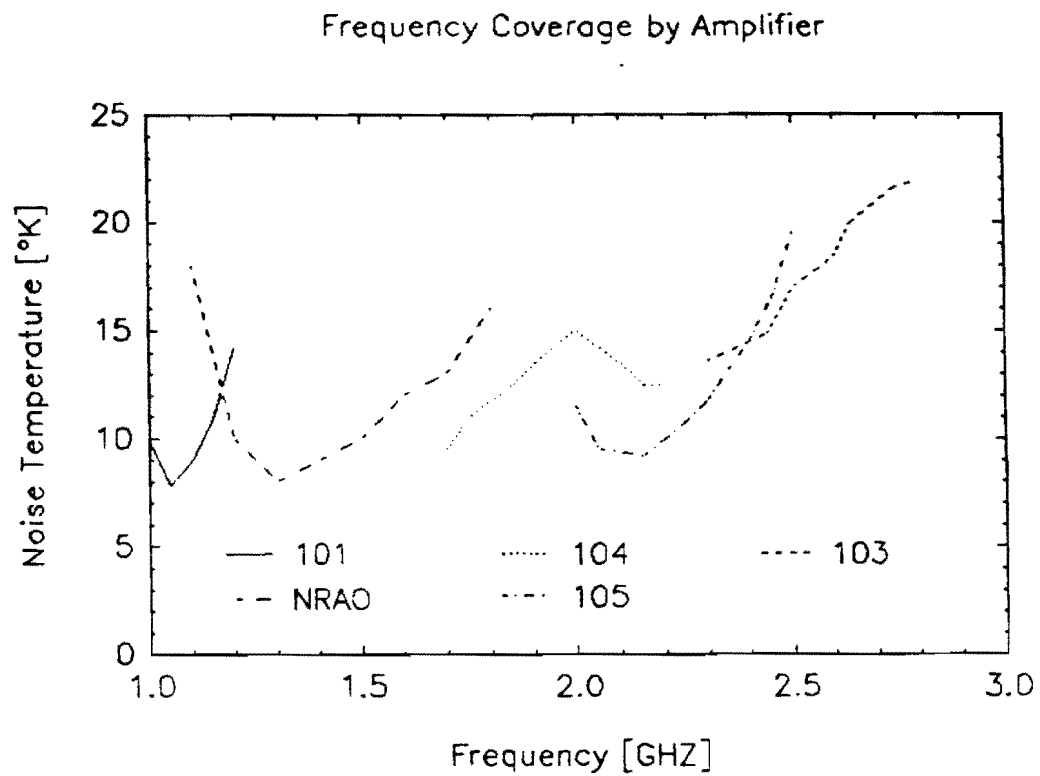
Figure 4.7: Noise temperature coverage by preamplifier as a function of frequency.

81
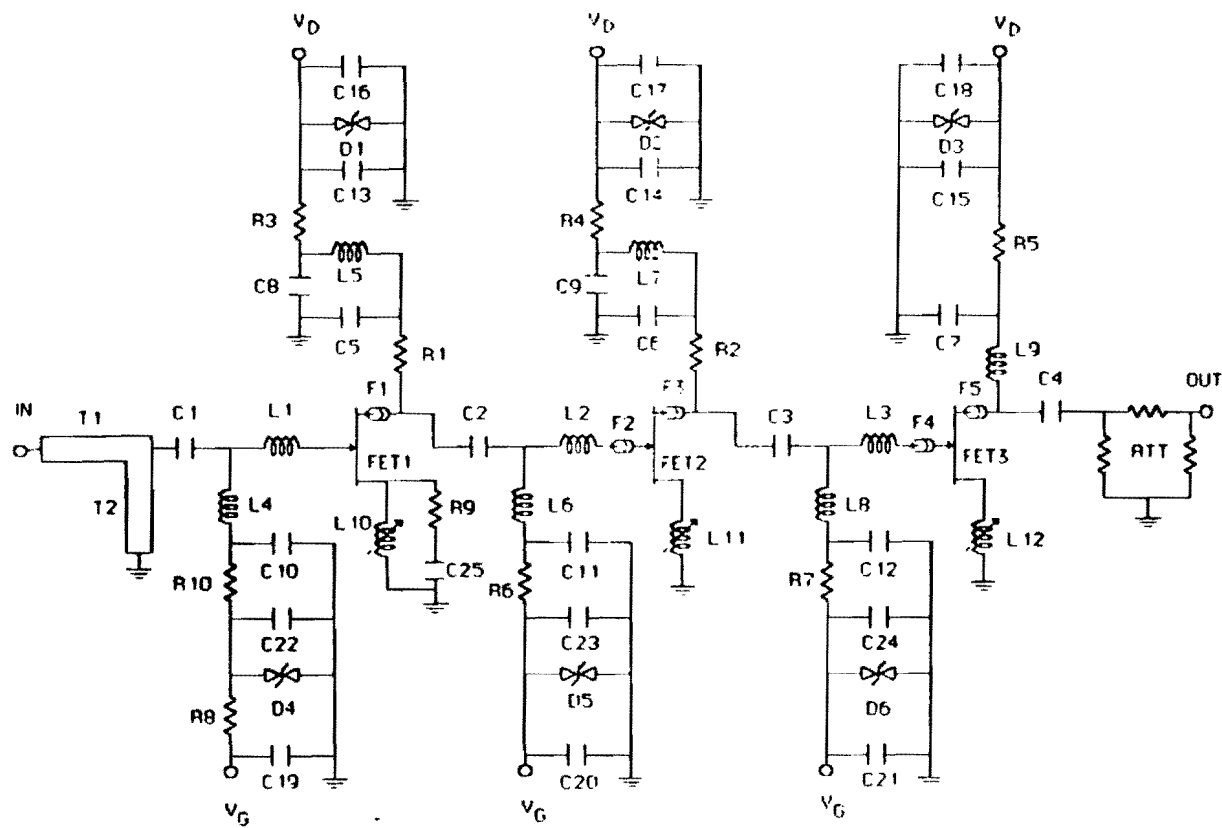
Figure 4.8: Preamplifier schematic.

the transistors to be matched to their optimum noise impedance while maintaining a relatively small input mismatch. The input matching network consists of a series $\lambda/4$ line with a $\lambda/4$ adjustable shunt which broadens the frequency range of the input match. Fine tuning of the input match is accomplished by adjustment of the shunt. The strip lines are constructed on a high dielectric constant ($\epsilon=10.4$) circuit board in order to minimize their size. Series R-C bypass networks in the first and second stage are used to reduce the tendency for high frequency oscillations. A 6 to 10 dB chip attenuator is incorporated into the output to insure stability independent of out-of-band termination impedance. The preamplifiers are constructed in a solid copper case which has been gold plated to maximize thermal conductivity. After construction the amplifiers must be tuned to optimize their low temperature performance due to variability in the construction and installation of the inductors.

Modification of the preamplifiers to operate at different frequencies has involved the redesign of the input matching network, shifting the frequencies of the interstage filters and R-C bypass networks, and readjusting the source inductance. The series and shunt striplines in the input matching network are linearly rescaled to maintain a $\lambda/4$ length. In addition the impedance of the series $\lambda/4$ line is changed as the optimum noise impedance for the FETs is a function of frequency. The shift in frequency of the interstage filters and R-C bypass networks requires changing the values of various capacitors and inductors. Another modification which has

83

been made, unrelated to changing the frequency, has been to replace the flat cover plate of the original design with a 1 inch deep "top-hat" cover. The NRAO amplifiers were designed to be as compact as possible to fit a number of amplifiers within the limited confines of a closed cycle helium refrigerator. The original cover plate, although compact, complicates optimization of the amplifier by introducing stray capacitance when put into place after tuning, causing unpredictable frequency shifts, overall increased noise, and oscillations. The top-hat cover has no noticeable effect on the preamplifier tune, and the extra space needed is not a problem in our configuration.

4.3 Circulators

The thermal noise power produced by a cavity is dependent on frequency and is given by,

$$P = 4kTB \frac{Q_L^2}{Q_0 Q_{ext}} \frac{1}{1 + Q_L^2 (\omega/\omega_0 - \omega_0/\omega)^2} \qquad (4.1)$$

where T is the physical temperature of the cavity and B is a measurement bandwidth smaller that the cavity width. Since the noise of the preamplifier is flat on the scale of a cavity resonance, the noise spectrum produced by the cavity and preamplifier should be that of equation (4.1) plus a flat background. However, the situation is more complicated due to impedance mismatches of the cavity and

84

preamplifier. The preamplifiers are designed to have a relatively low input mismatch, but they typically have a refection coefficient R ≈ .1 to .3 which varies slowly across the bandwidth of the preamplifier. In addition, the impedance a cavity presents is a strong function of frequency and is given by[3],

$$Z_c(\omega) = \frac{Z_0}{\beta} \left[1 + 2iQ_0 \left(\frac{\omega - \omega_0}{\omega} \right) \right] \qquad (4.2)$$

where $\beta = Q_0 / Q_{ext}$ (in this experiment $Z_0 = 50 \ \Omega$). The effect of the frequency dependant mismatch of the cavity combined with the mismatch of the preamplifier is to add a frequency dependence to the noise spectrum. The extra frequency dependence is due to varying reflections of the thermal noise of the cavity and preamplifier between the two devices. An example of the noise spectrum produced by a preamplifier with a microwave cavity on its input is shown in figure 4.9. The frequency dependence of the noise spectrum raises the overall noise temperature of the detection system, and produces a ripple in the final data when there are any variations in the tuning rate. Because peaks are being searched for in the data, flatness of the data is of primary importance, and the effect of ripple is quite serious. It would, in theory, be possible to compensate for the variation of the noise spectrum from the cavity in the data acquisition program, but the added complication due to impedance mismatches makes this impractical.
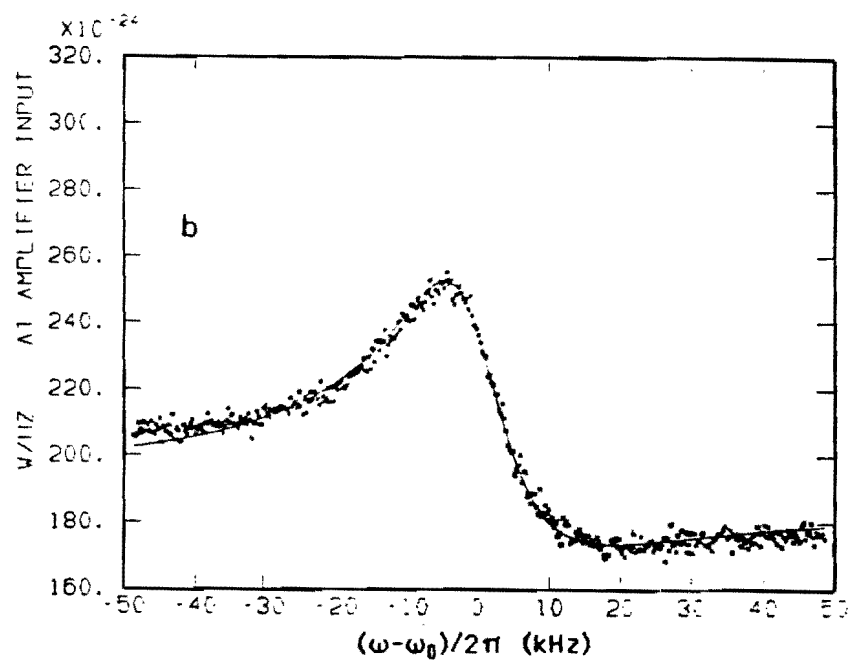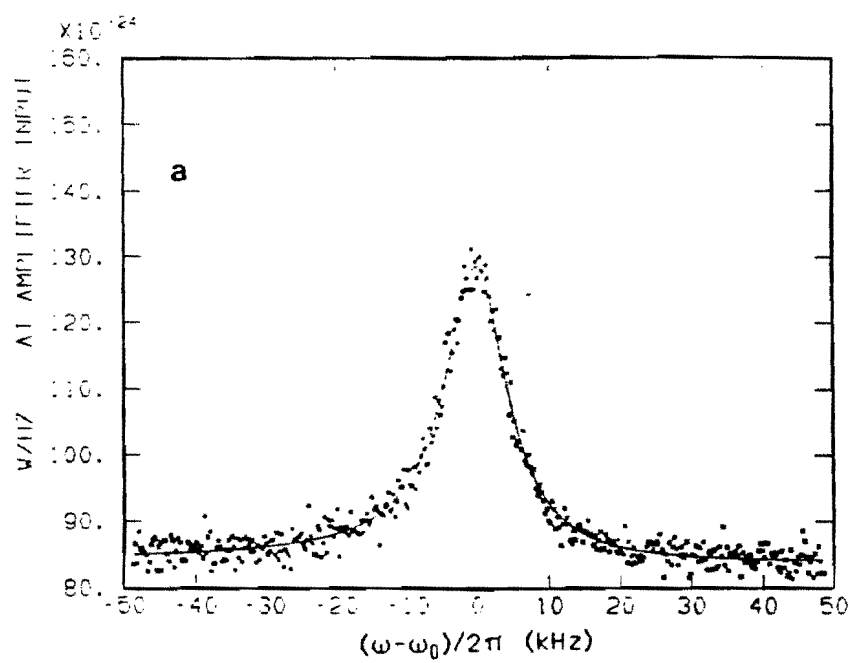
Figure 4.9: Noise from preamplifier 101 and cavity I. In the upper trace the cavity was tuned to 1.0902 GHz, in the lower trace the cavity was tuned to 1.2184 GHz. The cavity was critically coupled in both cases.

Instead, a circulator[4] is used to provide a constant 50 Ω input impedance to the preamplifier thereby eliminating reflections and flattening the noise spectrum. Circulators are passive, three port, unidirectional microwave devices. Microwaves can travel from one circulator port to the next in only one direction: either clockwise or counterclockwise. If one of the circulator ports is terminated the circulator behaves like an isolator; it allows a signal to pass from one device (A) to another (B) but not the reverse. This effectively provides a constant input impedance for the downstream device (B). Thus, when a circulator is placed between the cavity and the preamplifier the variation in the noise spectrum due to impedance mismatches is eliminated. This configuration is shown in figure 4.10.

In addition, the noise contribution of the termination on the circulator results in a completely flat noise spectrum if the termination is at the same temperature as the cavity. This is because the termination contributes to the thermal noise exactly in complement with the cavity. Noise from the termination is reflected from the cavity off resonance, which decreases the absolute sensitivity of the detector slightly. However, the flattening of the data makes the detector much more sensitive to actually finding a peak. Figure 4.11 shows data before and after use of the circulator[5]. There is still some ripple present in the data with the circulator present which is caused by non-uniformity in multiplexer channel calibration. As one can see, however, the
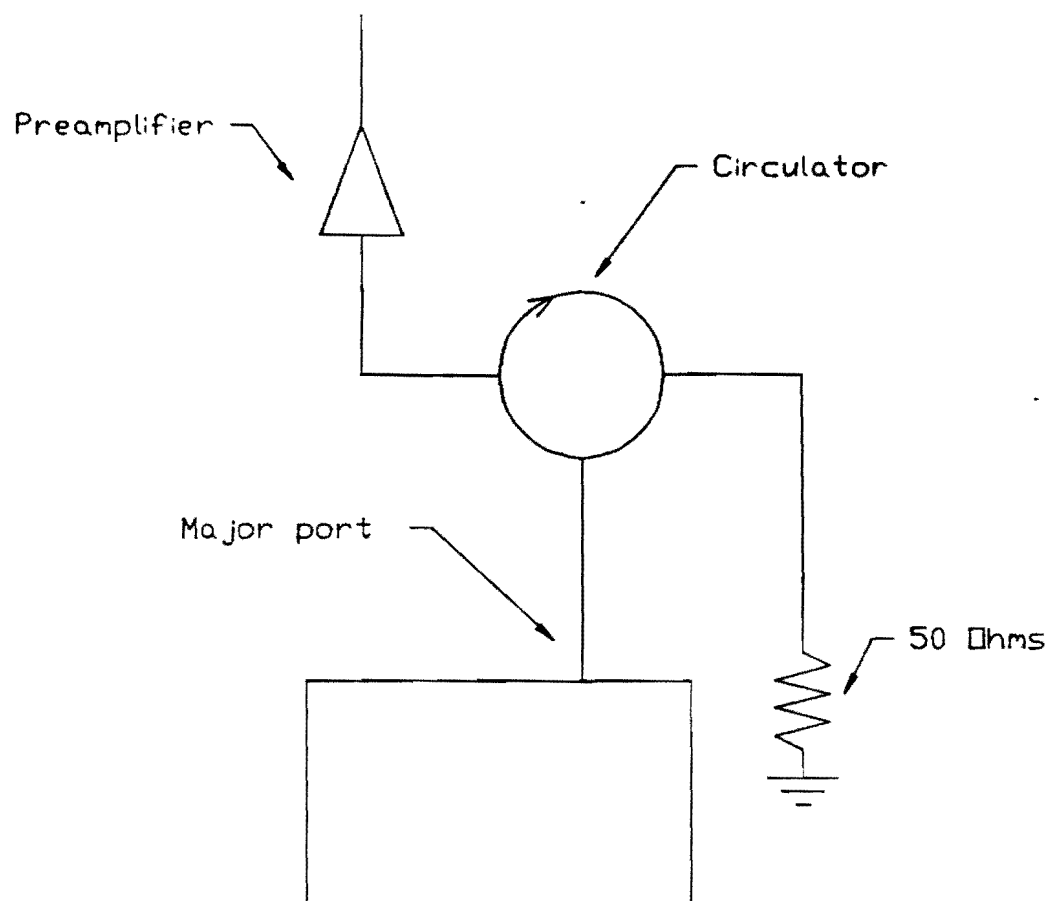
Figure 4.10: Cavity, circulator, preamplifier configuration.
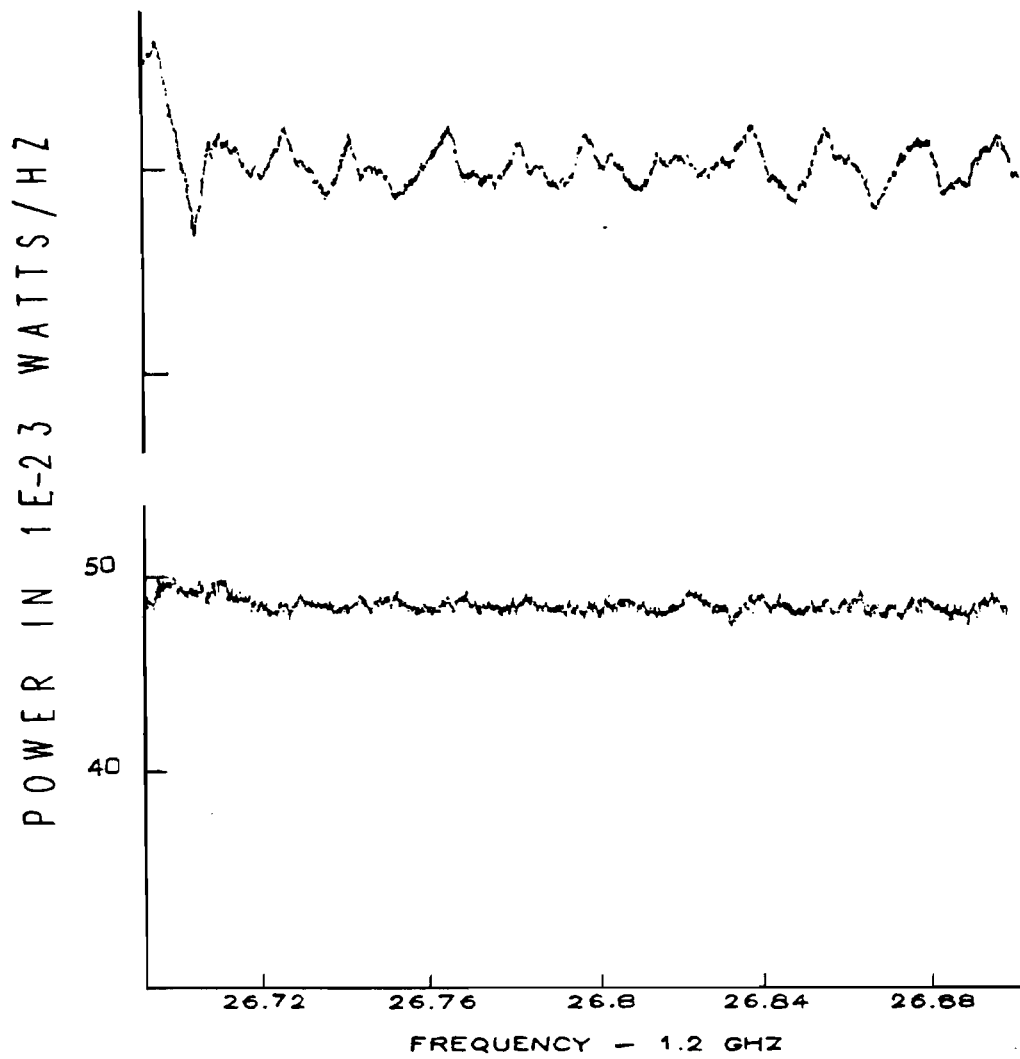
Figure 4.11: Sample data without the circulator (upper trace) and with the circulator (lower trace) for cavity II.

situation is much improved.

4.4 Room Temperature Electronics

After the cryogenic preamplifier, room temperature microwave devices are used for further signal processing. Figures 4.12 and 4.13 are schematics of the superheterodyne and final detection sections of the electronics. Before mixing, the signal exiting the cryogenic preamplifier is again amplified. Broadband room temperature amplifiers of sufficiently low noise for this purpose are readily available commercially. We have used a Miteq[6] AM-3A-1020 to cover the frequency range of 1 to 2 GHz and Miteq AFD4-020060-30 for the range 2 to 6 GHz. The noise temperatures of these amplifiers are 200 °K and 300 °K with gains of 35 and 40 dB respectively.

The signal has now been amplified enough to be mixed, since mixers have noise temperatures of approximately 10^5 °K. The signal is mixed twice: first to an intermediate frequency (IF) band of 10 MHz using the HP 8341A synthesizer as a local oscillator. The signal is then mixed to an IF of 10-50 kHz using an HP 3325A synthesizer as a local oscillator. This superheterodyne technique is used to keep the signal away from the phase noise of the first local oscillator. The frequency of the HP 8341A is swept to track the resonant frequency of the cavity as it is tuned to maintain a 10 MHz IF; thus all subsequent electronics can operate at a fixed frequency. Image-rejection mixers in both stages are used to

90
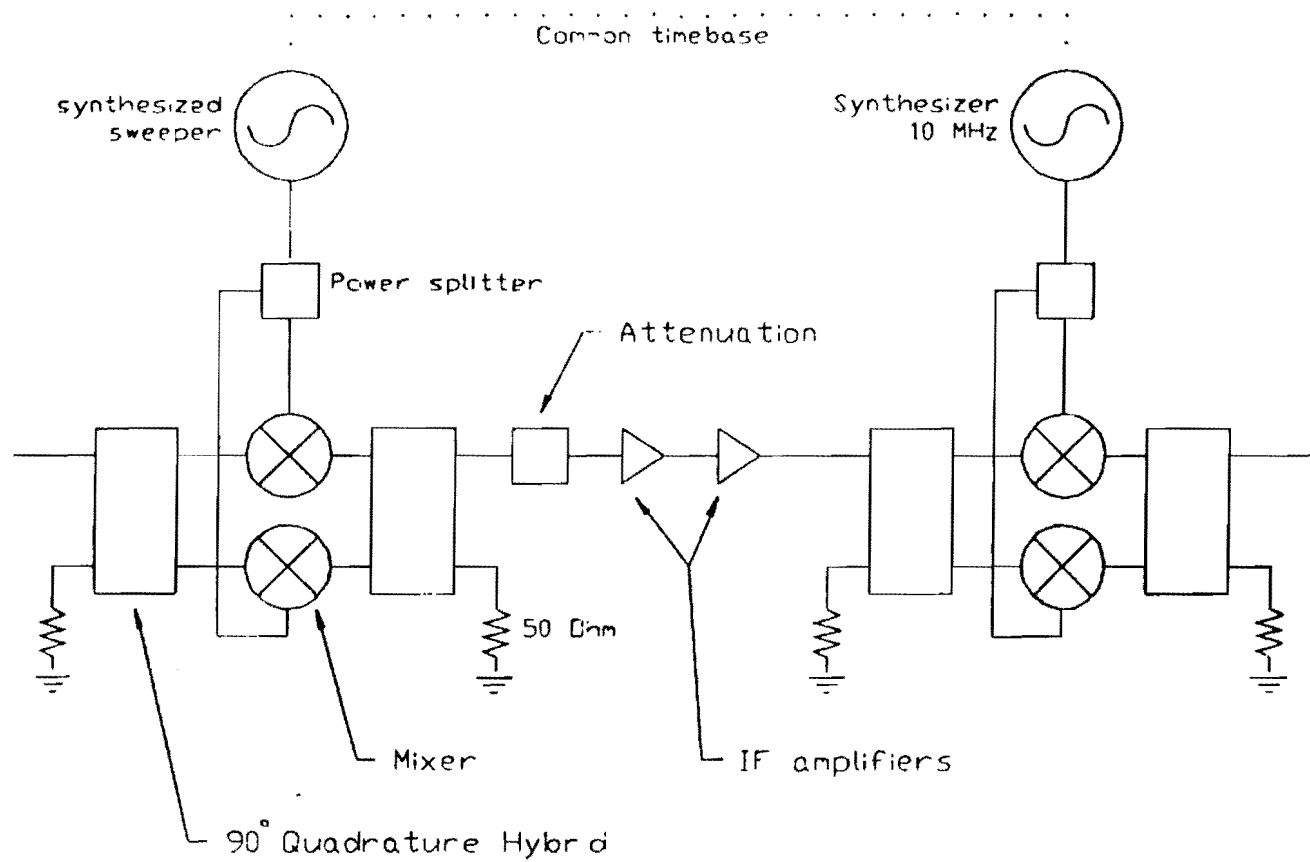
Figure 4.12: Superheterodyne section of the receiver.
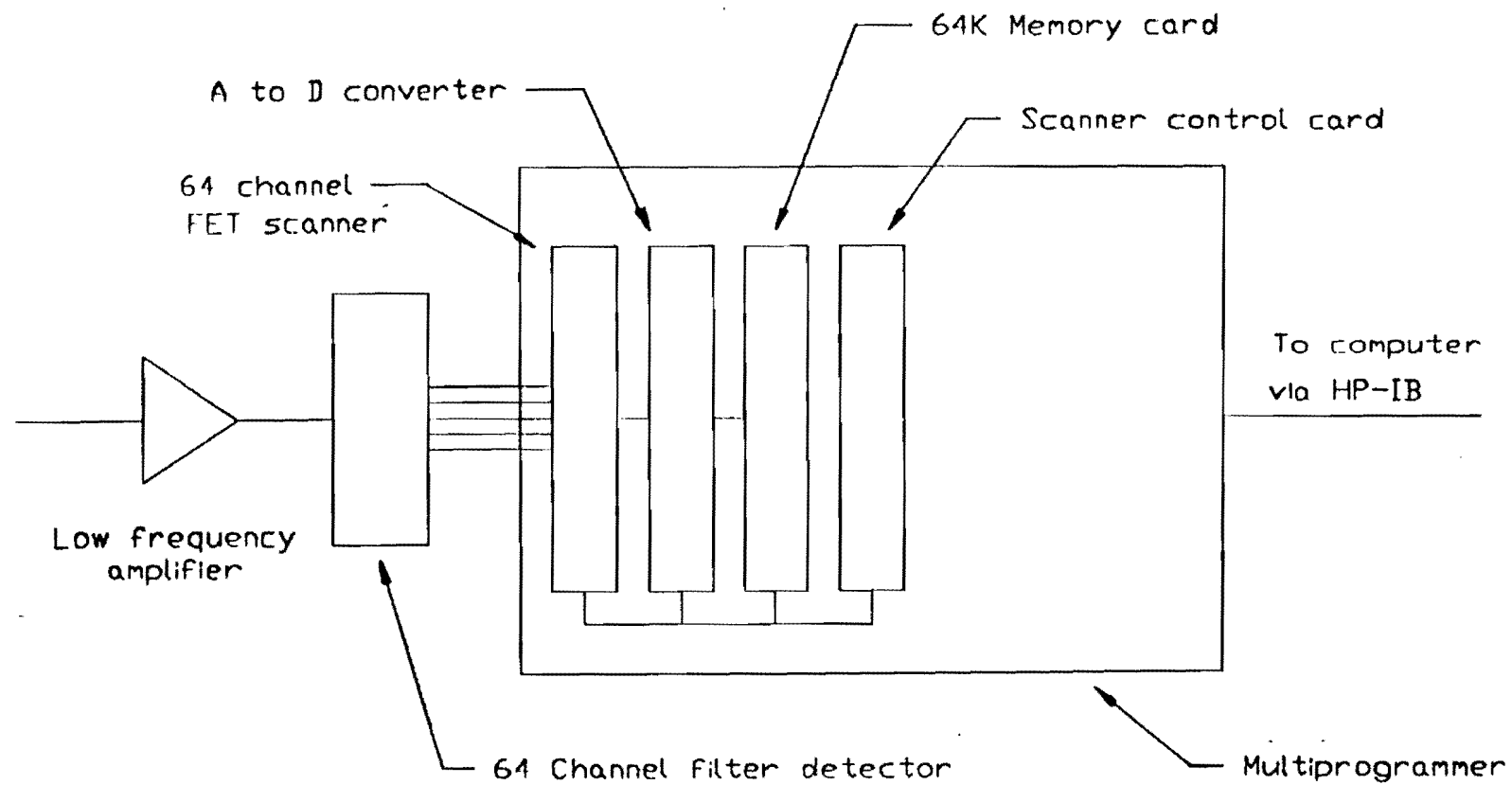
Figure 4.13: Final detection section of the receiver.

eliminate the unwanted sideband. Between mixing stages the signal is amplified by two 30 dB gain Anzac amplifiers[7].

After the final stage of room temperature amplification in a Brookdeal 5004 amplifier [8] the signal enters a 64 channel multiplexed filter/detector. Each of the 64 multiplexer channels has an active bandpass filter with an adjustable central frequency and bandwidth followed by a rectifier and low pass filter. Figure 4.14 shows a schematic of a single multiplexer channel. The 64 channels are tuned in ascending frequency from 20 KHz with a spacing equal to their bandwidth and act as a parallel spectrum analyzer. Two sets of filters have been used, one with 200 Hz, and the other with 400 Hz channel bandwidths. This allows one to match the filter bandwidth with the expected axion bandwidth at the frequency which is being searched. For example the 200 Hz channels have been used for data from 1.0 to 1.4 GHz and the 400 Hz channels have been used from 1.4 to 2.8 GHz (the expected axion signal $Q_{axion} \approx 3 \times 10^6$). The channels end in a rectifier followed by an averaging low pass filter with a time constant of .1 sec. This produces an output voltage proportional to the analog average of the of the peak to peak voltage of the incoming signal with an equivalent number of averages[9],

$$N_{ave} = \tau \Delta f \qquad (4.3)$$

where $\tau = 0.1$ sec and Δf is the channel width. The channels have an adjustable net gain which is used to ensure that the response to a

high Z input buffer   gain adjust   active filter   detector

1/4 IC1

input

R5   R1   1/4 IC1   R6   L1   C1   R8   R7   R2   R13   1/4 IC1   R9   1/4 IC1   C2   R10   R11   D1   output   R3   R4   R14   R12   C3
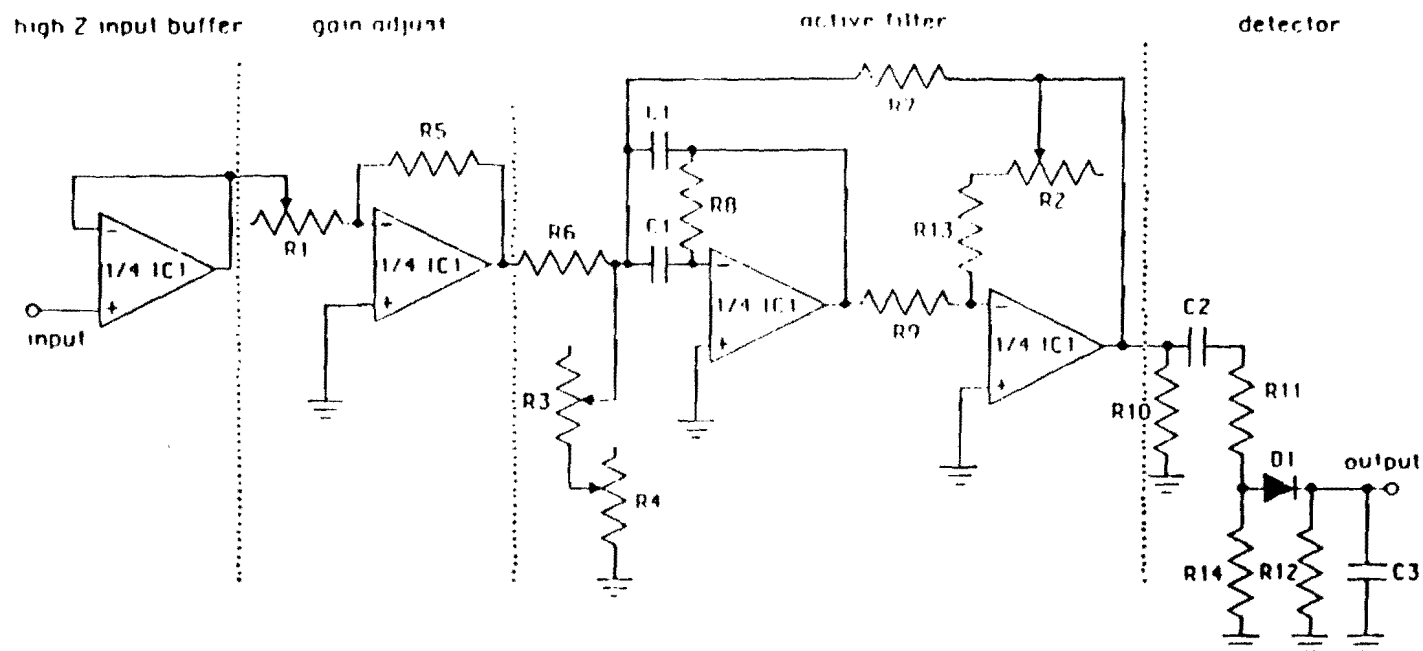
$R_1 = 50\ k\Omega$ $R_7 = 10\ k\Omega$ $C_1 = 1500\ pF$

$R_2 = 5\ k\Omega$ $R_{10} = 6.0\ k\Omega$ $C_2 = .47\ \mu F$

$R_3 = 1\ k\Omega$ $R_{11} = 50\ \Omega$ $C_3 = 4.7\ \mu F$

$R_4 = 20\ \Omega$ $R_{12,13} = 20\ k\Omega$ D_1 is an MBD101

$R_{5,6,8,9} = 46\ k\Omega$ $R_{14} = 10\ k\Omega$ IC1 is an HA4605

Figure 4.14: Multiplexer channel schematic.

flat noise spectrum from each channel is equal for all channels. This part of the multiplexer calibration is crucial as non-uniformities in channel response will contribute to ripple in the final data. Figure 4.15a shows the response of the multiplexer channels to white noise. The average output of the channels as a function of input power is also measured, as shown in figure 4.15b: this information is used by the off-line data analysis program.

The output of the integrating filters are connected to a single analog to digital converter through a 64 channel FET switch scanning system. The A/D, an HP 69751A, and the FET scanner, an HP 69752A, are cards which plug into an HP 6942A multiprogrammer. The function of these two cards are controlled by an HP 69750A scan control/pacer card and this card is in turn directly programmable by the acquisition computer through the multiprogrammer. The output of the A/D is stored in an HP 69791A 64K memory card. During data taking the FET scanner is programmed to read the output of the integrating filters sequentially at such a rate that any given channel is read every 100 msec, the decay time of the low-pass filter.

As the FET scanner and the A/D read successive multiplexer channels the A/D output is stored in the 64K word memory card in the multiprogrammer. At a rate of reading 64 channels every 0.1 seconds the memory card is half filled after 50 seconds. The card is configured in such a way that data are stored and read in a FIFO (first in first out) mode. In this way data can be read out from the
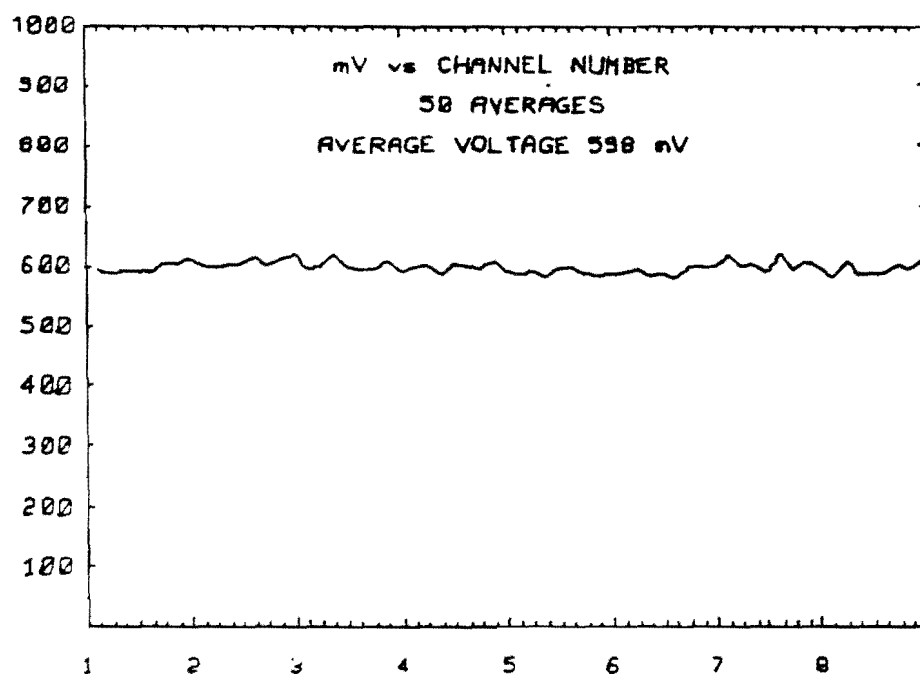
Figure 4.15a: Multiplexer channel response to white noise.

400 Hz Multiplexer Calibration 4/4/88

all points

$y = 1.2871 + 4.2054e\text{-}2x + 6.9316e\text{-}5x^2$

y = Power Input (nW/Hz)

x = mV out
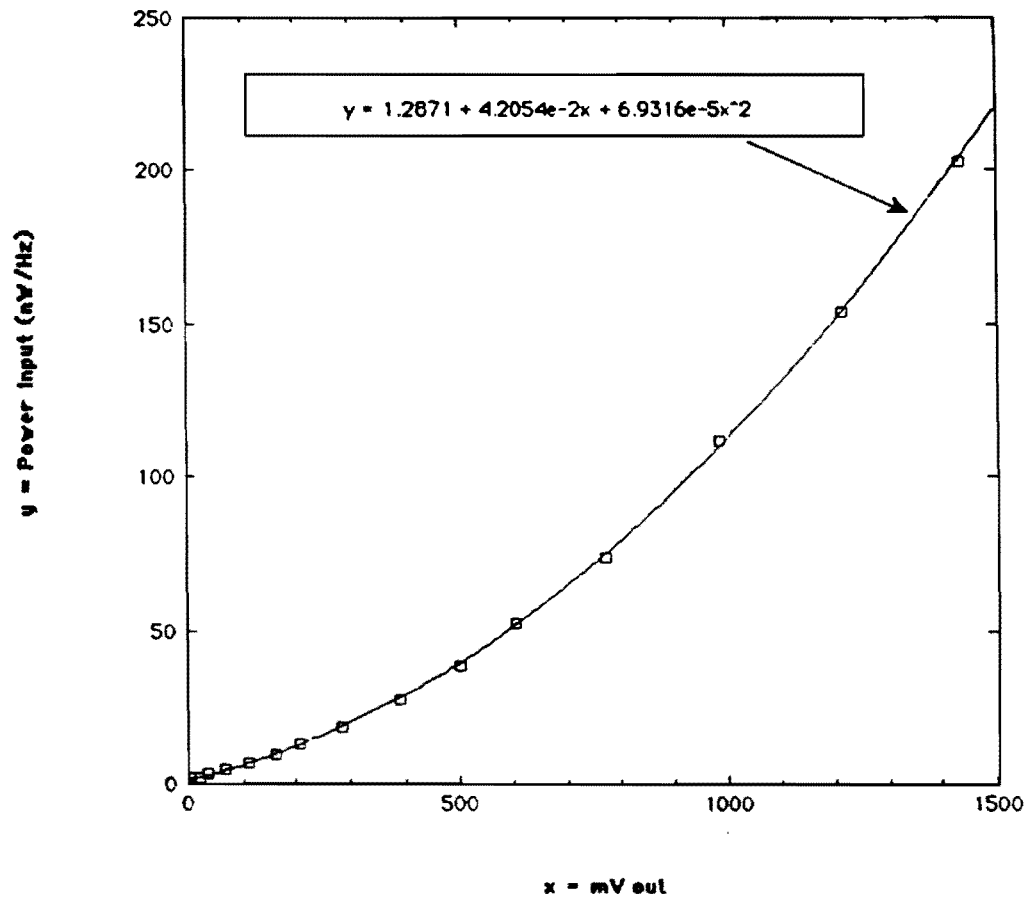
Figure 4.15b: Multiplexer output voltage vs. input power.

card concurrently with the card reading in more data.

Many of the functions which have been described use the same instruments. For example the synthesizer used as the first local oscillator is also used to determine the resonant frequency of the cavity, coupling strength etc. This is accomplished by using a series of electrically controlled microwave switches[10]. The switches are under computer control via an HP 69730A relay output card installed in the multiprogrammer. Figure 4.16 shows the switch configuration and the various settings which are used.

4.5 On-Line Noise Temperature Calibration

The experiment is configured to allow system gain and noise temperature measurements to be made during the course of data taking in order to determine the sensitivity as a function of frequency. The basic principle of the gain and noise temperature measurement is to compare the output of a device when different temperature calibrated white noise sources are input into the device. We have used a diode noise source with an excess noise ratio, ENR[11], of 15.80 dB or noise temperature 11,315 °K when biased and noise temperature 290 °K when unbiased as a well calibrated source of the white noise[12]. The measured power output by a device when a noise source is on and off are given by

$$P_{on} = kBG(T_{dev} + T_{on}) \qquad \text{Noise source on} \qquad (4.4)$$

98

HP8341A Synthesizer

Superheterodyne receiver

C

2

B

1

1   2

Noise source

D   1

Miteq

HP8757A Scalar
network analyzer

2

Cryogenic

Amplifier

20 dB attenuator

1   2

3

Circulator

Major port

Minor port

Cavity

	B	C	D	NS
Data	1	1	1	off
Reflection	2	2	2	off
Gain	1	1	1	on
Transmission	1	2	2	off
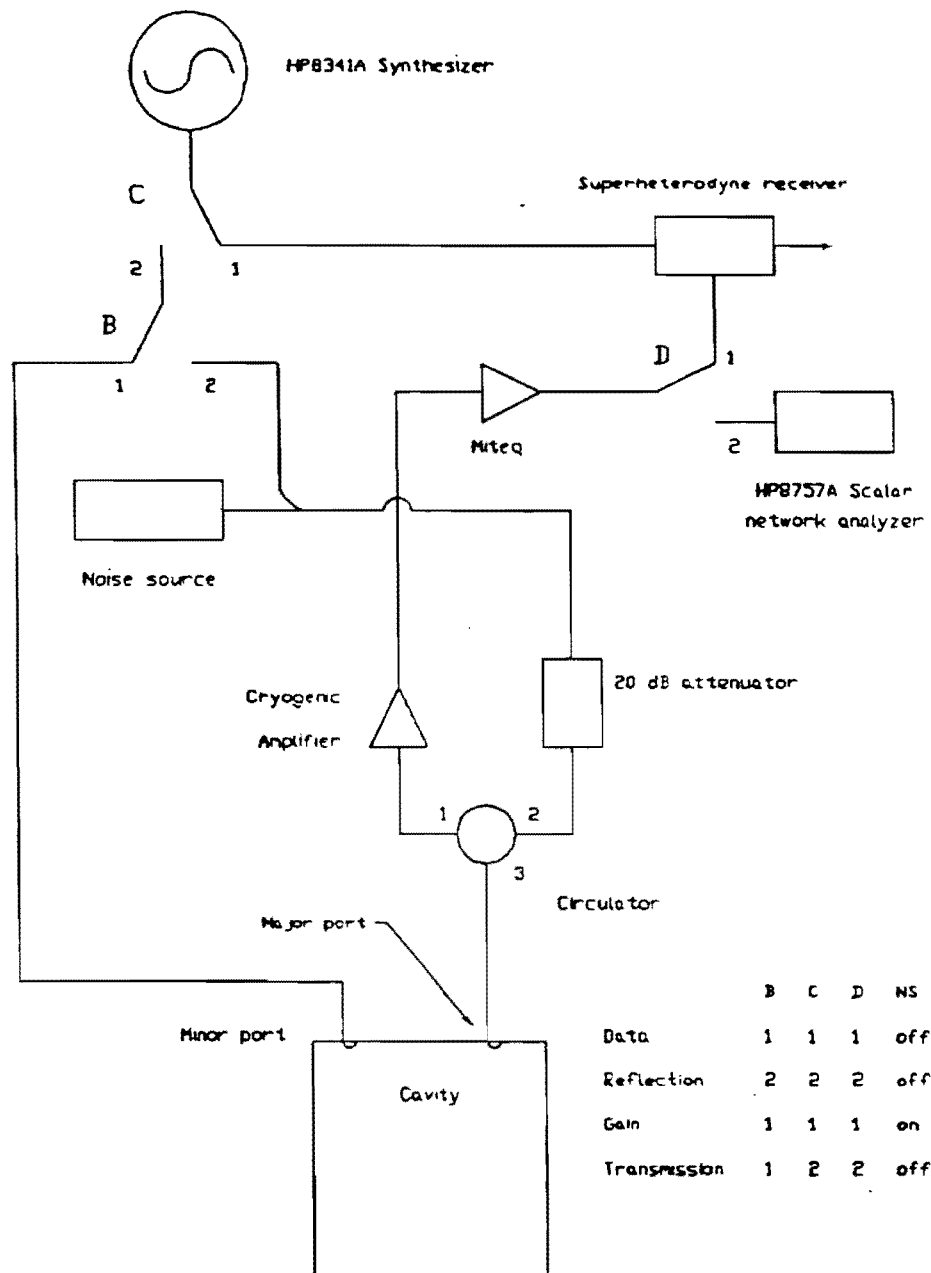
Figure 4.16: Microwave switch configuration.

$$P_{off} = kBG(T_{dev} + T_{off}) \qquad \text{Noise source off} \qquad (4.5)$$

where G is the gain, T_{dev} is the noise temperature of the device, and B is the measurement bandwidth. By subtracting the two equations one can calculate G,

$$G = (P_{on} - P_{off})/kB(T_{on} - T_{off}). \qquad (4.6)$$

And from G,

$$T_{dev} = P_{off}/kBG - T_{off}. \qquad (4.7)$$

The accuracy of a noise temperature measurement improves if the noise temperature of the noise source when unbiased (off) is about equal to or less than the noise temperature of the device under test. When testing a device of very low noise temperature like a cryogenic preamplifiers, a 20 dB attenuator is placed on the input which is cooled with the device. When the attenuator is cooled to a temperature T_{bath}, the effective noise temperature of the noise source is,

$$T = T_{bath} + \frac{T_{ns} - T_{bath}}{A} \qquad (4.8)$$

where A is the attenuation (20dB), and T_{ns} is the noise temperature of the noise source. In our application $T_{bath} = 4.2 \,^\circ K$.

100

The system gain and noise temperature measurement technique for on-line noise temperature measurements utilizes the circulator and reflection from the cavity off resonance to introduce the noise-source-on signal to the amplifier. The basic setup is shown in figure 4.17. Note that the termination on port 2 of the circulator has been changed to a 20 dB attenuator. This does not affect the function of the circulator as a 20 dB attenuator behaves very much like a termination. Regular data are used for the P_{off} measurement. P_{on} is measured by taking 10 readings per multiplexer channel, and averaging all channels together (for a total of 640 A/D readings), in normal data taking mode with the noise source on, and the local oscillator set so the receiver observes a band 1 MHz below the cavity resonance. Measuring the noise off of the cavity resonance is necessary to insure a complete reflection of the noise signal from the cavity. The noise-source-on measurement are taken at the end of each file. The off-line analysis programs perform the actual calculations. This technique calculates the gain and noise temperature for the entire detection system. The only quantities which must be supplied are the total attenuation between the noise source and the amplifier, and the temperature of the noise source on and off.
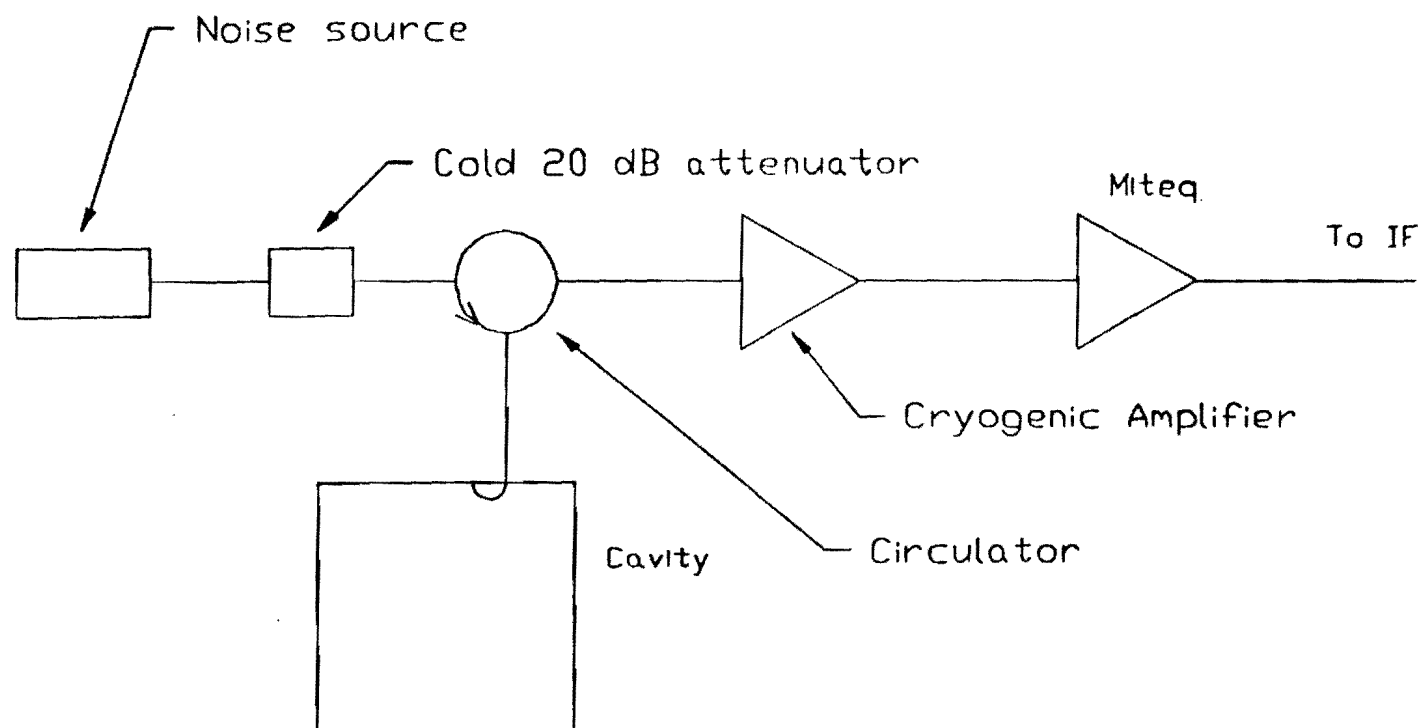
Figure 4.17: Noise measurement configuration.

4.6 The Data Acquisition Process

This section describes the computer program which controls the various components of the experiment and records the data. In the most general terms the task of the computer program can be divided into two main processes which must occur repetitively during data taking. First, as the resonant frequency of the cavity is swept by withdrawing the sapphire rod from the cavity, the acquisition program must track the resonant frequency of the cavity because the tuning rate is not perfectly uniform. Consequently, the program must keep the receiver tuned to the resonance by resetting the first local oscillator. Secondly, the output of the multiplexer must be recorded. This involves periodically transferring the data which have accumulated in the multiplexer memory card to the acquisition program and partially analyzing them. In addition to these two main tasks, the system also performs the noise temperature calibration, measurement of coupling, and measurement of current cavity Q at the end of each file. An HP series 9000 model 310 microcomputer is used for data acquisition and control purposes. Instruments are connected to it through an HP-IB (IEEE 488 standard) interface system, figure 4.18. The experimental control and data acquisition program is known as "ZAPPONE" and is written in Basic. A schematic representation of the program function is given in figure 4.19.

ZAPPONE begins the data taking process with an instrument initialization procedure which includes placing all computer
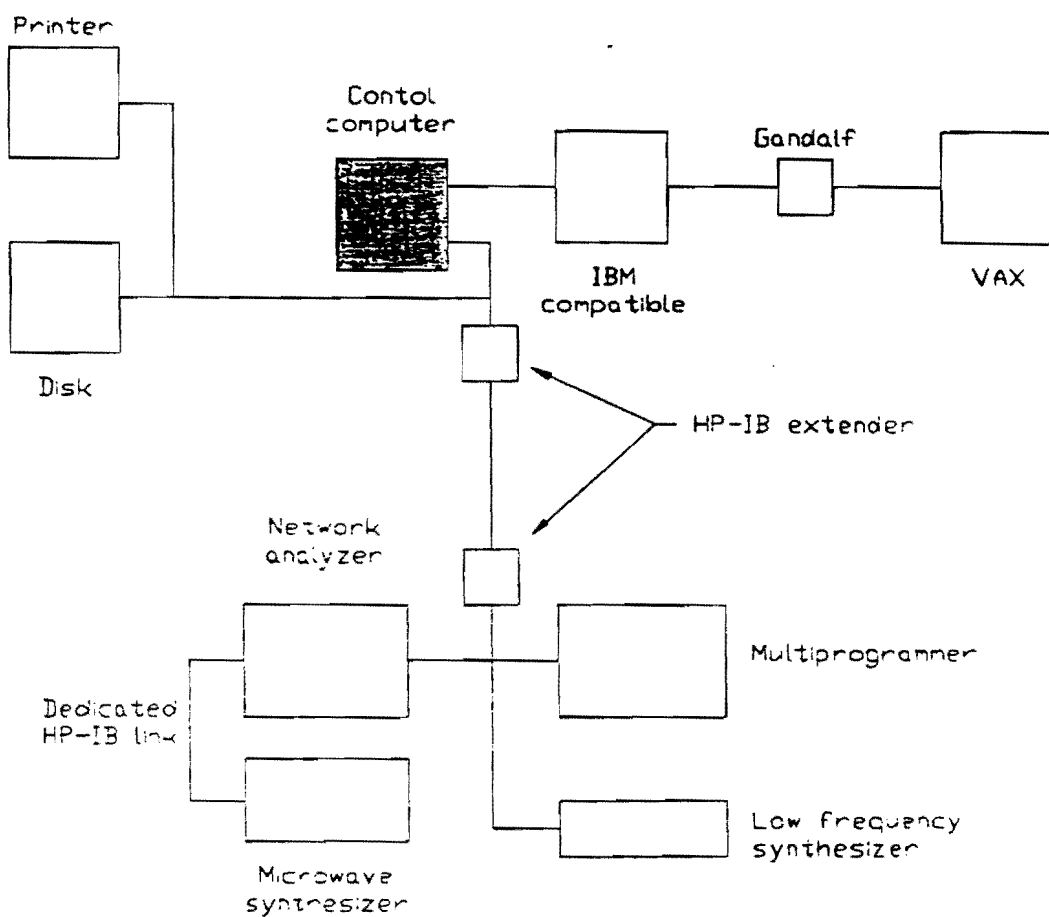
Figure 4.18: HP-IB instrument configuration.
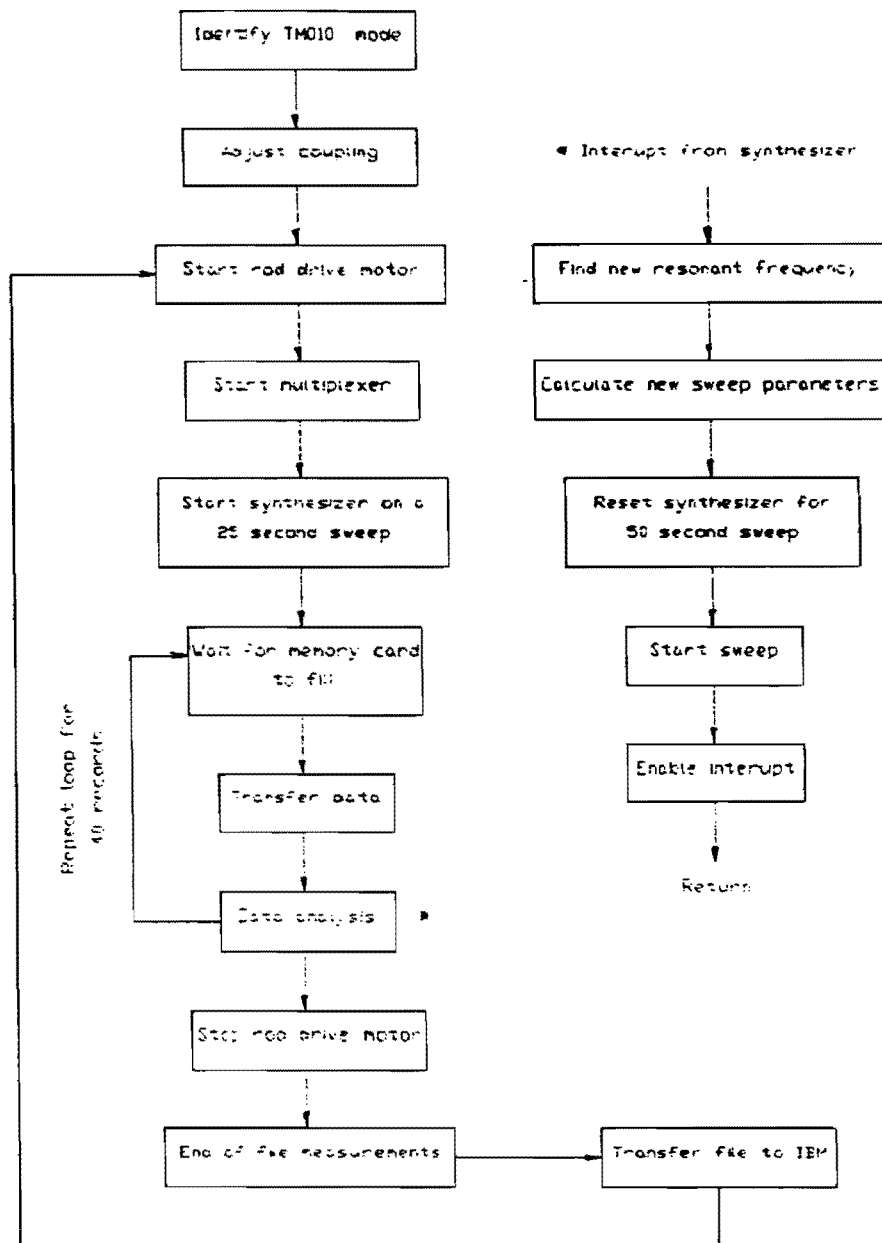
Figure 4.19: Schematic of ZAPPONE.

controlled instruments into known states and setting the second (fixed) local oscillator. ZAPPONE must be given the initial resonant frequency of the TM_{010} mode in order to identify it from the many other cavity resonances which exist. With the microwave switches set to transmission and the synthesizer set on a broad sweep, the experimenter selects the TM_{010} mode by centering it on the network analyzer display. ZAPPONE will remain locked on the TM_{010} mode during the rest of the data taking process. The coupling of the major port is then adjusted by hand with the microwave switches set to reflection and the synthesizer on a narrow sweep around the resonant frequency. The program then sets the tuning rod drive mechanism into motion and places the microwave switches into their data taking settings. A series of commands are sent to the scanner control card which instruct it to begin the reading of the multiplexer channels. Once initiated, this process continues without further intervention from the control program. Now the first local oscillator sweep is set and data taking has begun in earnest.

ZAPPONE performs the two processes of monitoring the resonant frequency of the TM_{010} mode and setting the local oscillator, and transferring and analyzing data on two 50 second cycles offset from each other by approximately 25 seconds. Each of the two processes require use of the HP-IB for about five seconds per cycle and the offset insures that they do not interfere with each other in their use of it. The main body of the program is linked to the 50 second data transfer and analysis cycle. As data is being taken and the

memory card is being filled, the program sits in a loop and continually checks to see when the memory card has been filled to 32K entries. This takes nearly exactly 50 seconds since the scanner control card has been instructed to scan at such a rate, see section 4.4. When the memory card is filled to this point, ZAPPONE begins to transfer the 32K words into an internal array over the HP-IB interface. The transfer of data takes about 5 seconds to complete. It should be noted that new data is still being read in while the transfer process occurs and there is no associated dead time. ZAPPONE then reduces the data, a task of some 30 seconds. A sample of the data is displayed on the computer terminal as well as the current resonant frequency, sweep rate, cavity Q, record and file number. The program now returns to the wait loop where it waits for the memory card to finish filling to 32K words. When the memory card has filled, the process of data transfer and analysis begins again.

Concurrently with data transfer and analysis, ZAPPONE is monitoring the frequency of the cavity resonance and resetting the local oscillator sweeps on the other 50 second cycle. The 50 second period is chosen to be short enough to insure that the resonant frequency of the cavity does not drift away from the receiver frequency during the course of a sweep. The timing of this cycle utilizes the interrupt capability of the HP computer and HP-IB interface system and consequently involves no waiting time on the part of the main program. When a synthesizer sweep is begun the synthesizer is instructed to generate an interrupt upon completion of

107

the sweep. When ZAPPONE detects an interrupt from the synthesizer it immediately branches to a subroutine called Syn_interrupt. Due to the 25 second offset of the two processes, this occurs when the computer is reducing data. Data reduction is suspended temporarily when the interrupt is received, however the program returns to that point at which it was interrupted upon completion of Syn_interrupt. Syn_interrupt finds the current cavity frequency, calculates the current sweep rate, and starts the local oscillator on a new sweep. ZAPPONE finds the current resonant frequency using a subroutine called Peak_find. Peak_find resets the microwave switches to their transmission settings and uses network analyzer and synthesizer to produce a transmission response curve of the cavity around the expected center of the cavity resonance. The point of maximum transmission through the cavity is the resonant frequency. ZAPPONE then calculates the sweep rate based on the resonant frequency of the cavity measured on the previous synthesizer cycle. In order to smooth out any non uniformities in the sweep rate, the calculated sweep rate is averaged with the old sweep rate according to the formula,

$$R = (R_{measured} + 2\ R_{old})/3. \qquad\qquad (4.9)$$

The microwave switches are returned to their data taking settings, the synthesizer is started on a new sweep, and the end of sweep interrupt is enabled. The peak finding and local oscillator resetting procedure takes approximately four seconds. The program

now returns to data reduction. During the four seconds of peak finding and local oscillator resetting the system has continued to read in values of the multiplexer channels. These readings do not represent valid data as the HP 374862 synthesizer is being used in a cavity transmission mode rather than in a local oscillator mode and the microwave switches are in transmission rather than data taking. These data are thrown out by ZAPPONE.

4.7 On-Line Data Reduction

The data which are read into ZAPPONE are in the form of a sequential list of multiplexer channel power levels. Of course, during the time the channels are read, the first local oscillator of the receiver has been sweeping. This means that a given channel of the multiplexer has measured a continually changing frequency band at the input of the multiplexer. In order to sort the sequential list of multiplexer channel outputs according to frequency, the frequencies of the multiplexer channel readings must be determined by the frequency of the local oscillator at the time of measurement. This is possible because the times of the beginning and end of the synthesizer sweeps are recorded. In addition, the time of the first channel reading in the 32K group is recorded and the time interval between channel readings is known (1.56 msec) so the time at which any given channel was read out can be determined. The subroutine Digest is designed to sort the data in this way. The algorithm used is fast enough to allow merely the use of interpreted Basic. The

properly sorted data is recorded in two arrays, File_dat and File_num. The entries of File_dat represent a frequency spectrum with a series of frequency bins with widths equal to the multiplexer channel width. The value of a given bin in File_dat is equal to the sum of the power levels of all channel measurements which correspond to the frequency of the bin. The bins in File_num contain the number of times a given frequency bin was measured. The averaged power as a function of frequency is thus determined by dividing the elements of File_dat by the corresponding elements of File_num.

At the end of 40 memory card dumps, i.e. 2000 seconds, ZAPPONE completes what is called a file. The rod drive motor is turned off. At this time the program takes a cavity transmission curve, a reflection curve, and the noise level away from resonance. Then it transfers the data over the HP-IB bus to the communications computer, an IBM PC clone[13]. At that point the HP begins taking data again. Meanwhile the PC transfers data to a VAX over Brookhaven's PACX phone line system. The data transfer takes about 10 seconds. The files are stored on the VAX for full analysis as described in the next chapter. In addition, a partial analysis is done immediately and the results are transferred back to the communications computer. There one can then see an immediate display of certain experimental parameters such as system gain and noise temperature, sweep rate, cavity Q, and coupling on a file by file basis. These outputs for cavity III, .400 rod, sweep 1 are shown in figures 4.20a to e. Various discontinuities are apparent in these figures. The sudden

110

drops on the system noise temperature plot are due to liquid helium refills which lower the physical temperature of the preamplifier. The jumps in cavity Q and coupling occur when the major port is readjusted for critical coupling, because, in general, the coupling increases as the rod is withdrawn, for a fixed major port position.
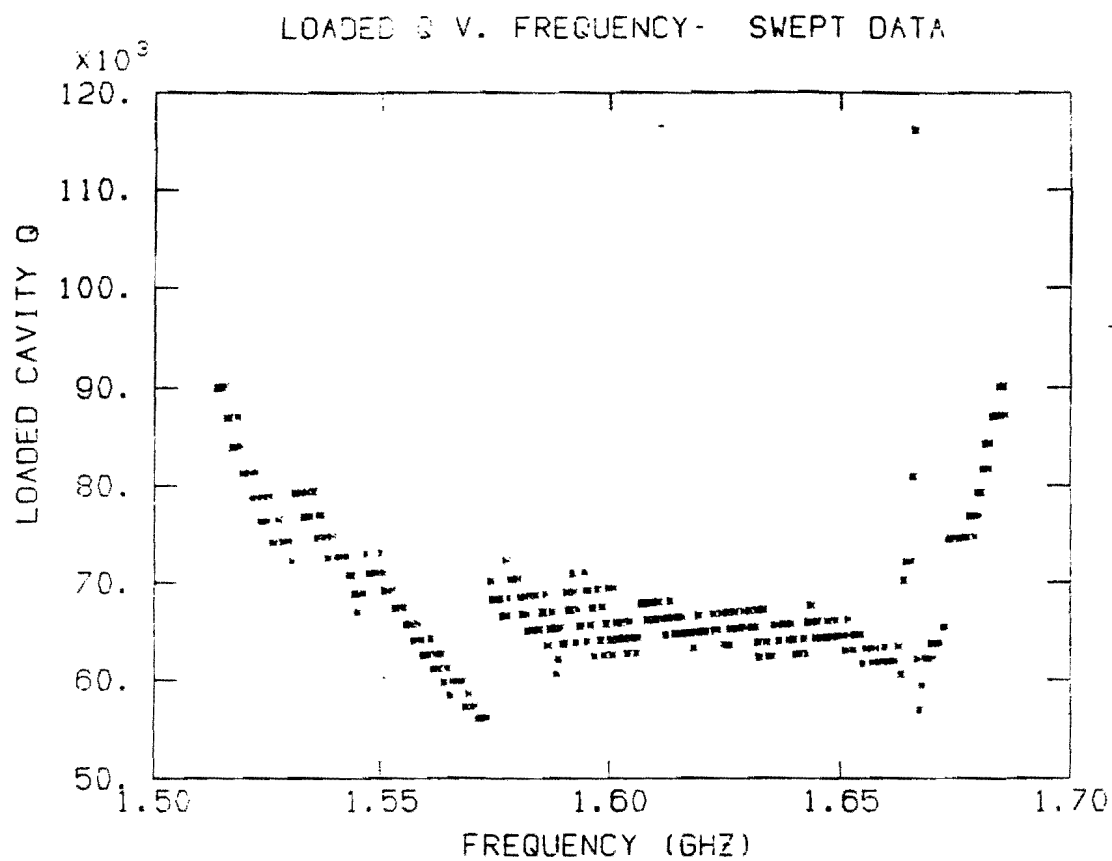
Figure 4.20a: Immediate display from cavity III, sweep 1, loaded Q vs. frequency.

CAVITY REFLECTION V. FREQUENCY-   SWEPT DATA
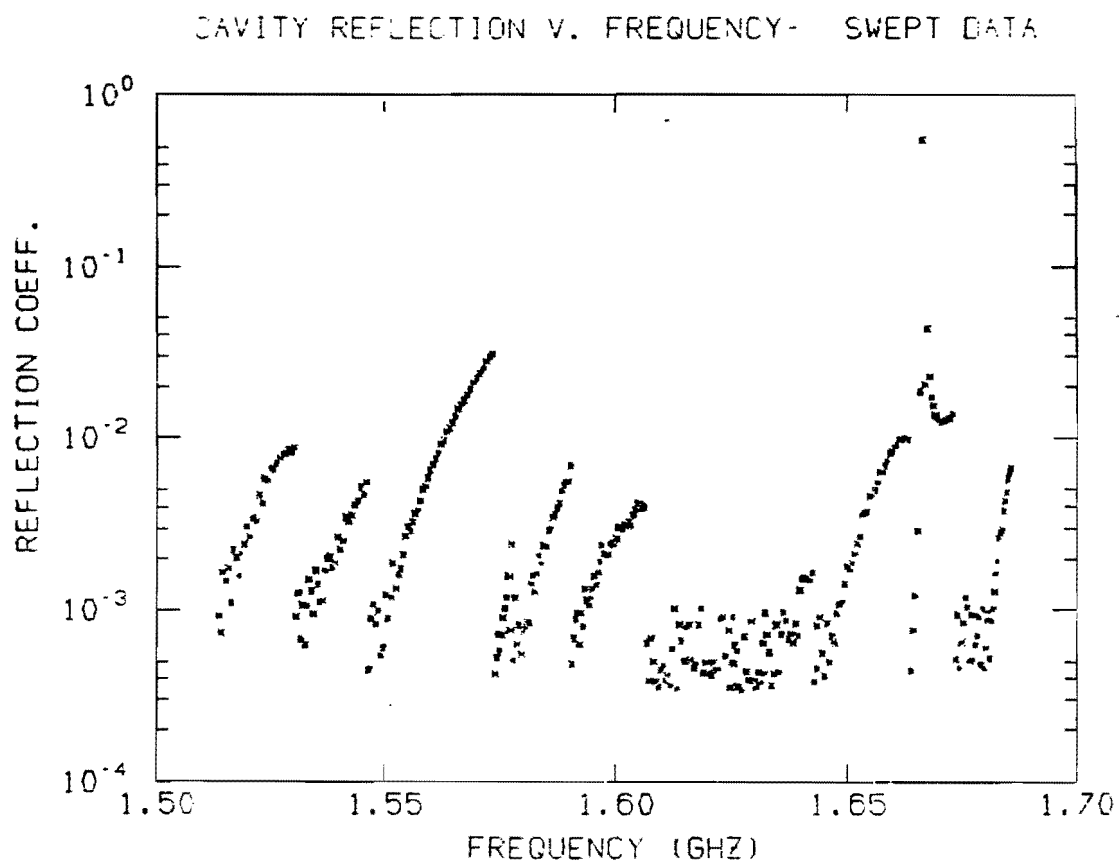
Figure 4.20b: Immediate display from cavity III, sweep 1, reflection form the minor port vs. frequency.

TOTAL SYSTEM GAIN V. FREQUENCY- SWEPT DATA
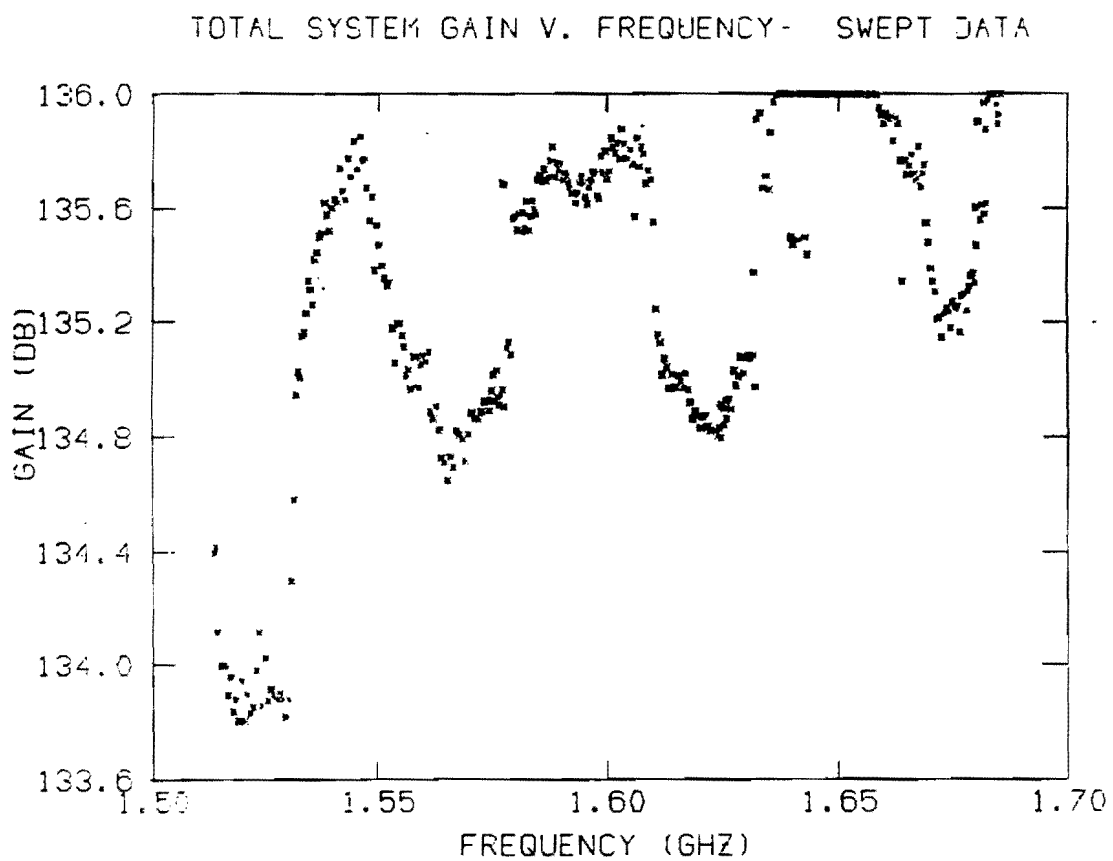
Figure 4.20c: Immediate display from cavity III, sweep 1, system gain vs. frequency.

114

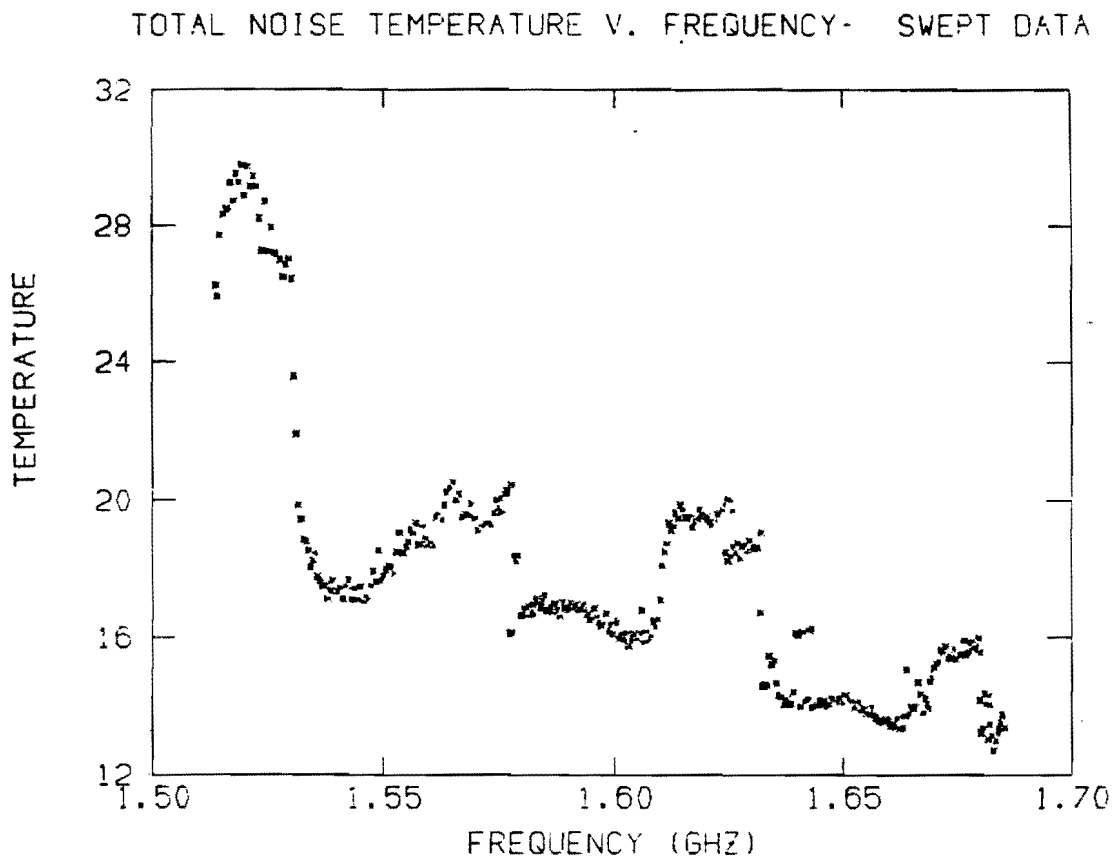TOTAL NOISE TEMPERATURE V. FREQUENCY- SWEPT DATA

Figure 4.20d: Immediate display from cavity III, sweep 1, system noise temperature vs. frequency.
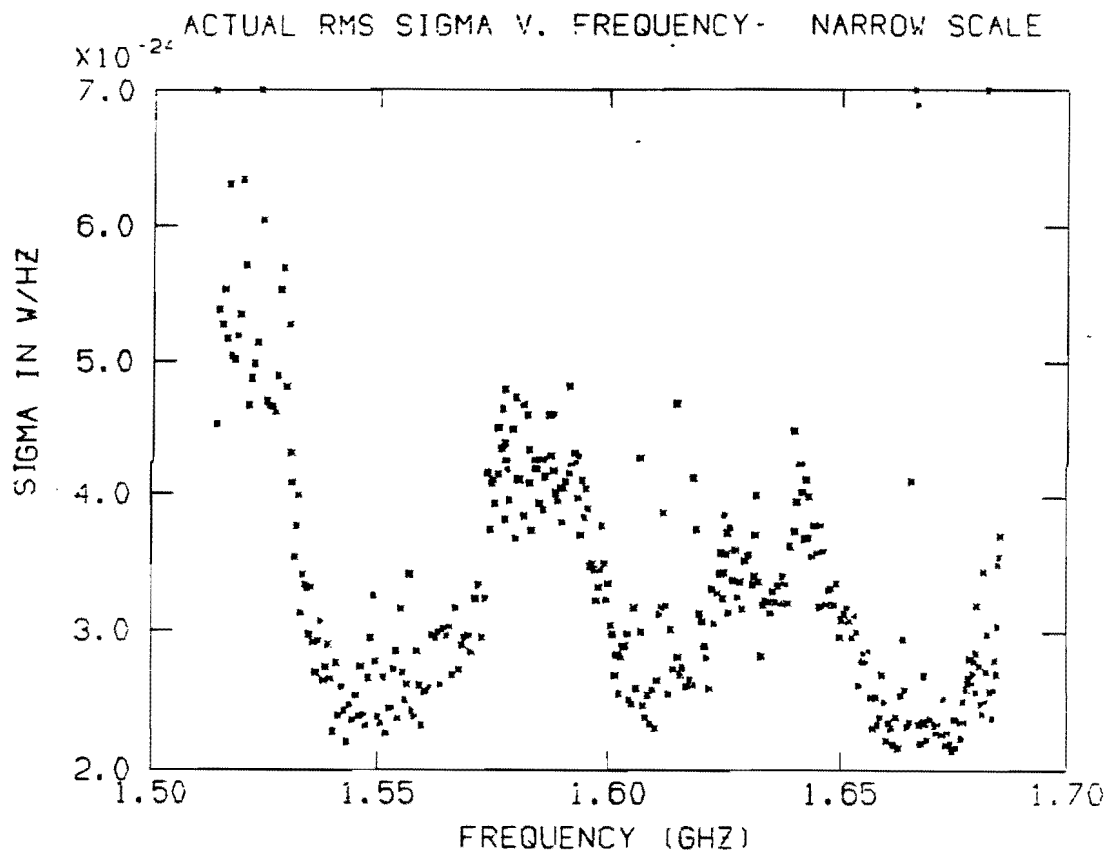
115

Figure 4.20e: Immediate display from cavity III, sweep 1, value of σ vs. frequency.

116

References

1. S. Weinreb, D. Fenstermacher and R. Harris, "Ultra Low-Noise 1.2-1.7 Ghz cooled GaAs FET Amplifiers," National Radio Astronomy Observatory internal report 220, 1981.

2. S. De Panfilis, J. Rogers, "L- and S-Band Low-Noise Cryogenic GaAs FET Amplifiers," IEEE Trans. on Microwave Thy. and Tech. 36, 607 (1988).

3. B. Moskowitz, J. Rogers, "Analysis of a Microwave Cavity Detector Coupled to a Noisy Amplifier," Nucl. Inst. and Meth. **A264**, 445 (1988).

4. We have used cryogenic circulators manufactured by Passive Microwave Technology, Canoga Park, California. The following models with corresponding frequency ranges were used: LTE 1208 for 1.1 to 1.4 GHz, LTE 1212K for 1.4 to 1.9 GHz, STE 1220K for 1.8 to 2.1 GHz, STE 1221K for 2.1 to 2.6 GHz, STE 1222K for 2.5 to 3.5 GHz, CTE 1144K for 3.3 to 4.6 GHz, and CTE 1145K for 4.3 to 6.0 GHz.

5. An explanation of the meaning of the data output can be found in section 5.3.

6. Miteq Inc., 125 Ricefield Lane, Hauppauge, New York 11788.

7. Anzac. Inc.,80 Cambridge St., Burlington, MA 01803.

8. Brookdeal Electronics Limited, Doncastle House, Doncastle Road, Bracknell, Berkshire RG12 4PG.

9. R. B. Blackman and J. W. Tukey, *The Measurement of Power Spectra* (Dover, New York 1958).

10. Teledyne Microwave, Model CS33S6D microwave switches.

11. The ENR is defined by

$$ENR = 10 \log ((T-290)/290)$$

where T is the noise temperature of the device in degrees K.

12. Micronetics Inc. model NSI-11B noise source. Micronetics Inc., 36 Oak Street, Norwood, New Jersey 07648.

13. A PCs Limited Turbo PC with an HP 82990A HP-IB interface board.

Chapter 5: Data Analysis

5.1 Data Taking

The cavity sweep rate, which is a function of the rod drive motor speed and of the amount of drive shaft reduction, determines the time it takes to cover the frequency range of a particular cavity and tuning rod combination. The sweep rate is controllable by the experimenter and represents a conscious compromise between sensitivity and frequency coverage over a fixed period of time. In particular, the signal to noise ratio of the detector, r, as a function of sweep rate, df/dt, is given by,

$$r = \frac{P_a}{\Delta P_n} \tag{5.1}$$

$$= \frac{P_a}{kT_n \Delta f (N^{-1/2})} \tag{5.2}$$

$$= \frac{P_a}{kT_n} \left(\frac{m}{df/dt} \right)^{1/2} \tag{5.3}$$

where P_a is the expected axion signal stength, ΔP_n is the power level of 1σ fluctuations in the noise, T_n is the noise temperature of the detector, N is the number of measurements which are averaged, Δf is the multiplexer channel width, and m is the number of multiplexer channels. Our group has placed relatively more importance on

118

frequency coverage and sensitivity of the basic apparatus than to increasing the sensitivity with low sweep rates. We feel that this is a reasonable position as a comprehensive axion search would ultimately have to cover more than the range of 1 to 30 GHz and, furthermore, the limit placed on $g_{a\gamma\gamma}$ only improves in proportion to $t^{1/4}$, where t is the time spent averaging on a particular frequency band, as discussed in section 2.3.

Two sweeps are taken through each cavity-rod tuning range and the sweep rate for each run is adjusted so that the two sweeps take approximately one month (the setup and cool-down takes approximately one week). A listing of the dates on which the various cavity rod combinations were used to take data is given in table 5.1. Maintaining such a schedule typically results in sweep rates of one multiplexer channel bandwidth per second[1], that is, 200 Hz/sec for cavity II and 400 Hz/sec for the remaining cavities. From this, one can obtain a rough idea of the degree of improvement in sensitivity which will be brought about by averaging. Since there are 64 multiplexer channels, a given frequency bin is active for 64 seconds, and 640 A/D readings are taken. Including the effects of the averaging filter (equation 4.3), a typical frequency bin is averaged 25,000 times when 200 Hz wide bins are used and 50,000 times when 400 Hz wide bins are used. For such averaging and a system noise temperature of 15 °K, the magnitude of a 1σ fluctuation in the background noise spectrum has a power density of $\sigma \approx 9 \times 10^{-25}$ W/Hz. Because the sweep rate, and consequently the number of averages per

CAVITY NUMBER	ROD DIAMETER	FREQUENCY RANGE (GHz)	DATES
		·	
2	.585"	1.218184 1.415462	Apr 23 – Jun 22 (1987)
5	.250"	2.235948 2.458031	Dec 3 – Jan 8 ('87–'88)
5	.400"	1.951617 2.247175	Jan 12 – Feb 5 (1988)
3	.400"	1.513340 1.685593	Feb 23 – Mar 15
4	.400"	1.761929 2.085878	Mar 27 – Apr 18
3	.585"	1.413812 1.516602	May 2 – May 8
4	.585	1.686074 1.764383	May 25 – Jun 1

·

Table 5.1:   The dates on which runs of different cavity–rod combinations occured.

frequency bin, varies during data taking, the power level of a 1σ fluctuation varies.

After a file of data has been taken, it is sent to the University of Rochester VAX 11/780 at the Brookhaven On Line Data Facility (OLDF) as described in section 4.7. The data have already been partially analyzed by the acquisition program in the sense that the individual A/D readings have been averaged together within a file. However, the data must be further analyzed by combining the files together into a continuous frequency spectrum, calculating the system gain and noise temperature, tabulating values of Q and reflection, and producing graphical output. Calculation of the system gain specifies what power level, at the output of the microwave cavity, a given multiplexer channel output corresponds to. This in turn specifies the noise temperature of the system. These tasks are accomplished by the program AXION on the VAX computer. The program also calculates the statistical distribution of the power levels of the frequency bins and selects statistically significant peaks from among them. An abbreviated version of AXION, IMMEDIATE_AXION, is run by the VAX after every file transfer. The system gain, noise temperature, cavity coupling, and cavity Q for the transferred file are returned to the communications PC for display, as already mentioned. At the end of each sweep through a cavity rod tuning range, all of the files of data are combined into a single file known as a DST (data summary tape). A DST contains gain normalized power levels and number of A to D readings for all frequency bins.

121

5.2 The Data

Figure 5.1 shows the fully analyzed data from two passes through a 400 kHz frequency range taken with cavity III and amplifier 104. Each bin represents the averaged power in 400 Hz. Printouts of the data similar to figure 5.1 are produced for the entire tuning range of each cavity-rod combination. The vertical bars of the data points represent the magnitude of the 1σ standard deviation the points should have based on the number of averaged power measurements at that particular frequency. If the variation in the power in each of the bins is merely due to averaged noise, then the distribution of power levels should be Gaussian with a standard deviation equal to the standard deviation calculated from the number of averages,

$$\sigma_n = \frac{P_{ave}}{(N_{ave})^{1/2}} = \frac{P_{ave}}{(N_{a/d}\Delta f\tau)^{1/2}} \qquad (5.4)$$

were P_{ave} is the average power level, N_{ave} total number of averages, $N_{a/d}$ is the number of A to D readings, Δf is the multiplexer channel width, and τ is the time between readouts of the multiplexer averaging filters. One can see that σ_n corresponds to the standard distribution of the actual distribution of power levels because a histogram of $(P_i - P_{ave}) / \sigma_n$ results in a Gaussian distribution of unit width. Figure 5.2 shows the histogram of $(P_i - P_{ave}) / \sigma_n$ for the first 100,000 frequency bins of cavity III. The full width at half maximum of a Gaussian of unit width should be 2.35, while 2.5 is
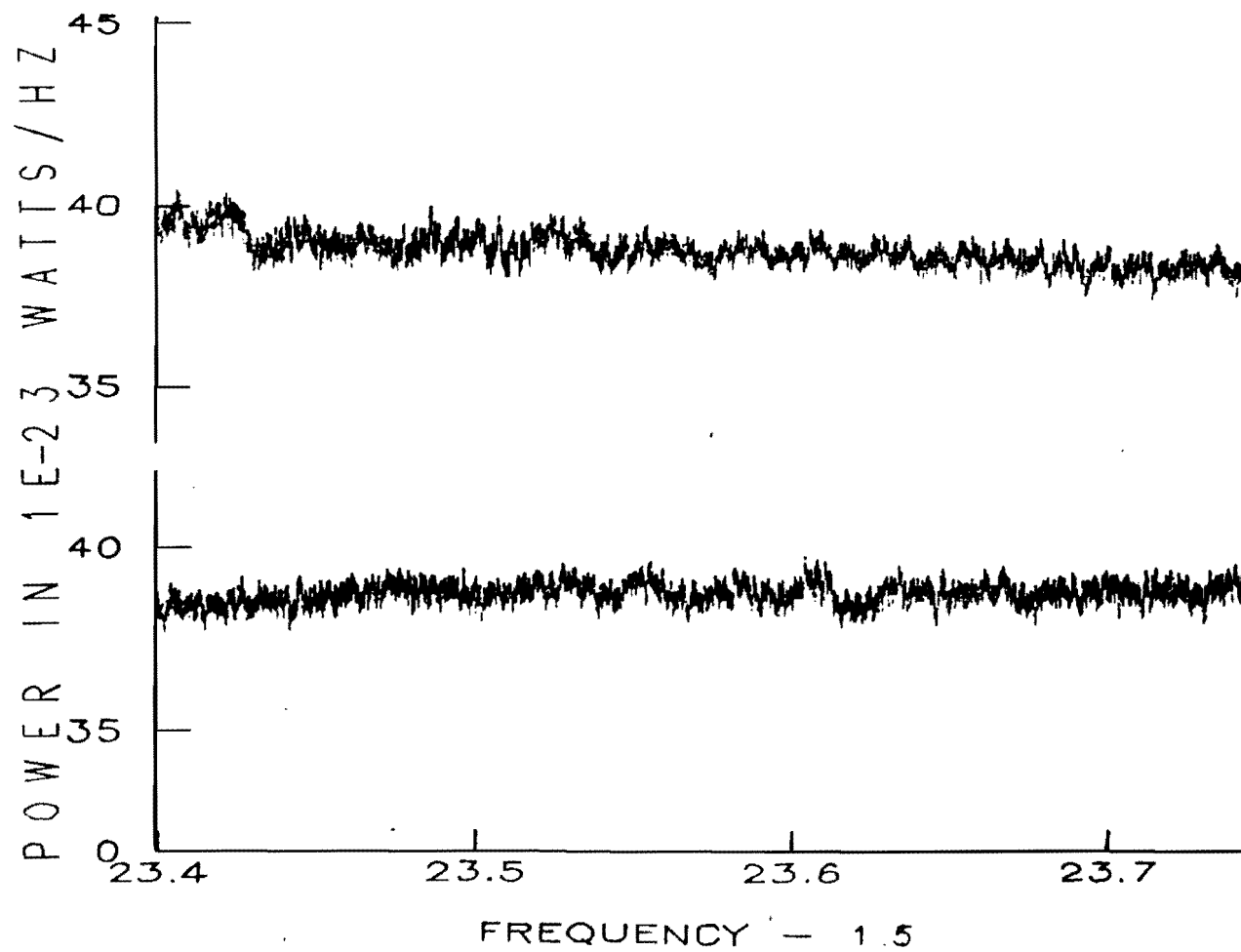
Figure 5.1: Data from cavity III with 400 Hz multiplexer channels. The upper trace is sweep 1, the lower is sweep 2.
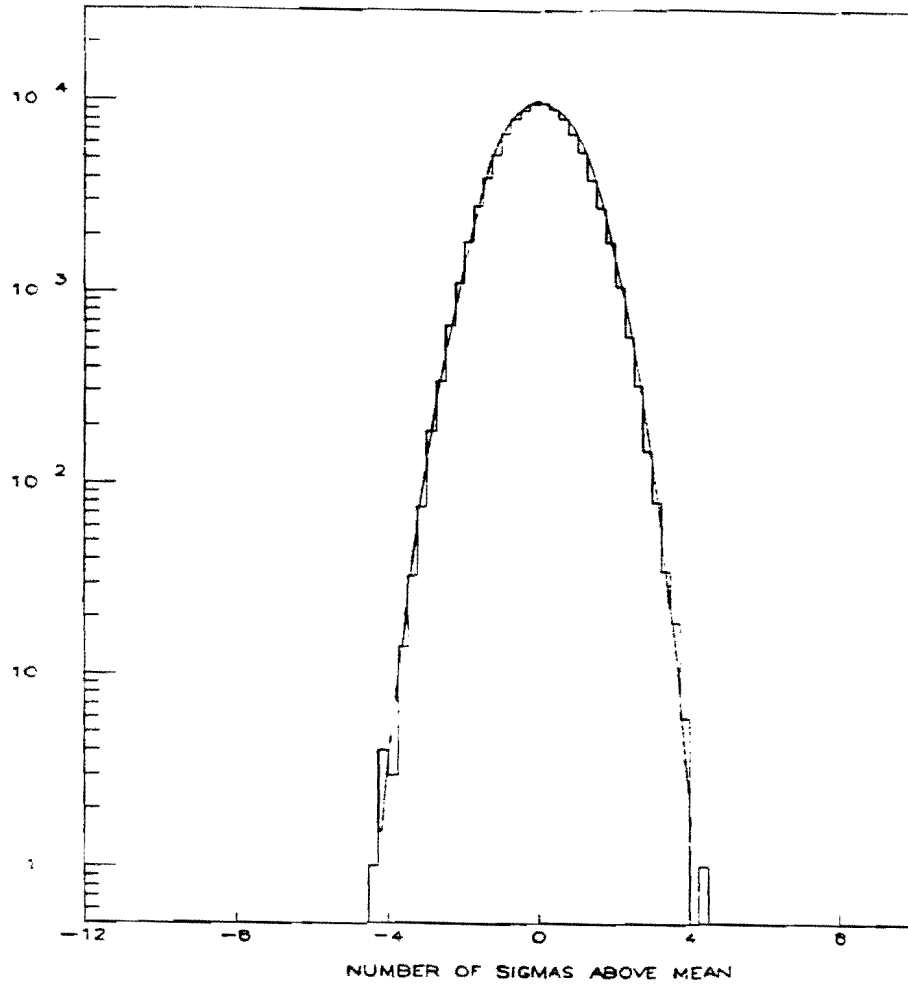
Figure 5.2: Histogram of $(P_i - P_{ave})/\sigma_{a/d}$ from the first 100,000 bins of cavity III. The superimposed curve is a Gaussian of unit width, $\sim e^{-x^2/2}$.

found in figure 5.2.

However, from figure 5.1 one can see that the distribution of power levels is not *completely* Gaussian. There are a number of structures in the data at various scales which are a result of various idiosyncrasies of the apparatus. For example there are undulations with a "wavelength" on the order of 50 bins. They are due to non-uniformities in sweep rate between synthesizer resets, combined with unevenly calibrated multiplexer channels. If the sweep rate speeds up or slows down then a particular frequency bin will not be averaged the same number of times by each multiplexer channel. Some frequency bins will be averaged relatively more by higher noise channels (channels in which the product of bandwidth and gain is larger) than other frequency bins. Since the sweep-rate is uniform during an individual local oscillator sweep this uniformity only shows up on a time scale of 50 seconds, the time between synthesizer resets. This corresponds to about 50 frequency bins with a sweep rate of one channel per second. For this reason, the change in sweep rate during local oscillator resets is damped by averaging the current sweep rate with the past average sweep rate, see section 4.5. On scales of MHz one starts to see variations in the power spectrum due to microwave reflections and variation of the microwave devices in general. In particular, the preamplifier has gain and noise temperature variations on this scale.

5.3 Finding Peaks

The major objective of the data analysis is to search through the frequency spectra which are produced by the apparatus to determine whether there are any structures which may be caused by the conversion of axions. As discussed in section 1.3, it is not known exactly what the power spectrum of galactic halo axions would be. In general, though, the expected feature in the data is a peak of some narrow, but unknown, width. Such a peak would appear in the data as one or more frequency bins where the power level is higher than the local background power level. A certain number of peaks will exist due to the Gaussian nature of the noise spectrum, as discussed in section 2.3. In addition, searching for peaks is complicated by the imperfections present in real data.

Therefore, a peak searching algorithm must have a definition of a peak which is functional given the imperfections of the data. The most natural definition of a peak is a frequency bin which deviates some number of standard deviations from a locally calculated mean using a locally calculated standard deviation. If the data were purely Gaussian this would be a very satisfactory definition. In actual practice, the local mean and standard deviation, σ, are calculated by considering the power levels in 30 bins higher and

126

lower in frequency to the bin of interest. For the ith channel,

$$\langle x_i \rangle = \frac{1}{60-2} \left[\sum_{i-30}^{i-1} x_j + \sum_{i+1}^{i+30} x_j \right], \tag{5.5}$$

$$\sigma_{local} = \langle x^2 - \langle x \rangle^2 \rangle^{1/2}, \tag{5.6}$$

$$n_\sigma = x_i - \langle x_i \rangle / \sigma_{local} \tag{5.7}$$

The window for the calculation is limited to 60 bins to try to exclude any larger scale trends in the data from skewing the statistical weight assigned to certain bins. However, even the 60 bin mean results in the preferential selection of bins at the top of undulations and an overestimate of the size of σ. In addition, the bin of interest and the points immediately higher and lower in frequency are excluded in order to eliminate errors in the average power level when signal strengths are very high, in particular for the case when calibration peaks are injected (see below). This is necessary because peaks are broadened by the Lorentzian line shape of the multiplexer filters. In other words, a channel still has some response to frequencies that nominally lie inside adjacent channels. This can cause errors in the average power level and σ for sufficiently strong peaks.

Given a peak finding algorithm, AXION calculates the number of standard deviations the power level of a particular frequency bin is away from the mean. It then produces a file which contains a list of the frequencies and number of standard deviations above the mean

127

of all bins which have channels above a specified threshold (usually 3σ). These files are known as ANA (analyzed) files. The distribution of the deviations from the mean of power levels in terms of the locally calculated σ's for the entire sweeps of cavity III, .400 rod, and cavity V, .250 rod, are shown in figures 5.3 and 5.4 respectively. The figures show a Gaussian distribution of deviations from the mean power level with small tails of high σ events.

In order to test the peak checking algorithm we have placed calibration signals into the data to determine how well the algorithm recognizes a peak. This is accomplished by injecting a narrow constant frequency signal into the cavity through the minor port during normal data taking. When the cavity tunes through the frequency of the calibration signal a peak will appear in the data. Modifications to the basic data taking setup for peak injection are summarized in figure 5.5. A frequency doubler (although it is often used as a frequency tripler) was used because the HP8656B synthesizer has a maximum frequency of 990 MHz and no other microwave synthesizer was available in the lab. The signal strength is first calibrated with the system set to transmission using the network analyzer as a power detector. Then an appropriate amount of attenuation is added to the injected signal path to bring the signal power down to a value corresponding to the number of σ peaks one wishes. Figure 5.6 shows an example of an injected peak with a power of 2.0×10^{-18} W at 2.4 GHz. The peak is a testament to the absolute frequency accuracy of the experiment as the peak falls exactly in the appropriate bin

Figure 5.3: Distribution of bin power levels in terms of a locally calculated mean and σ for cavity III, .400 rod, for 400 Hz wide channels. The superimposed curve is a Gaussian of unit width, $\sim e^{-x^2/2}$.
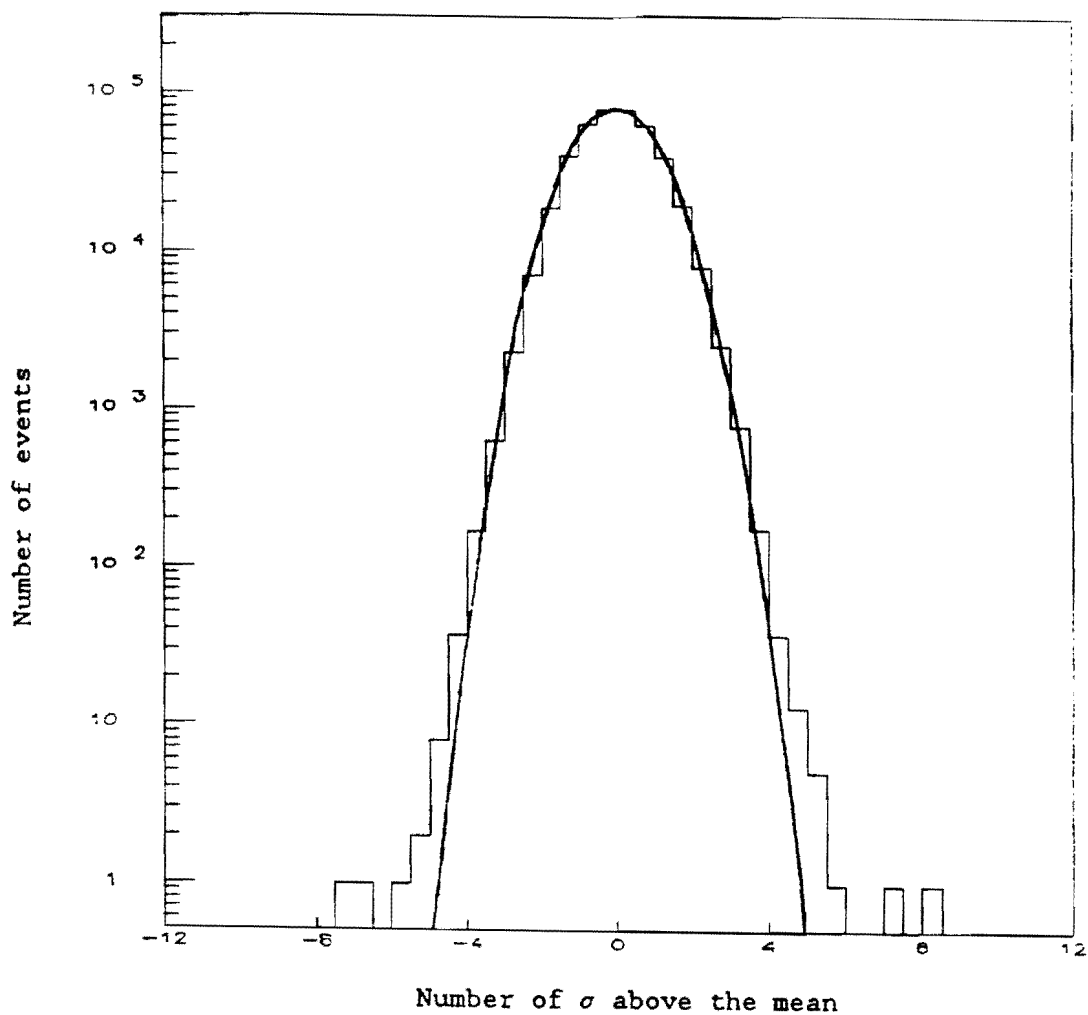
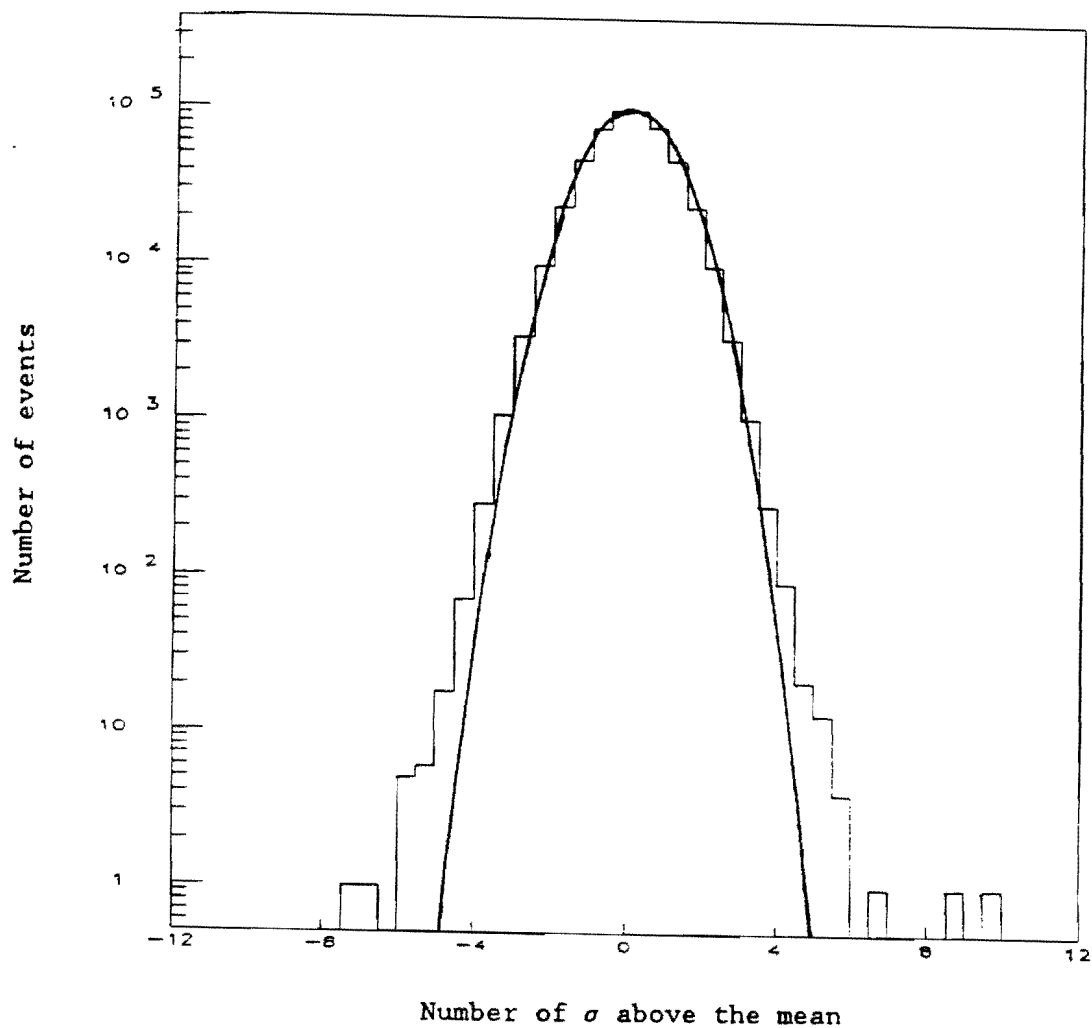129

Figure 5.4: Distribution of bin power levels in terms of a locally calculated mean and σ for cavity V, .250 rod, for 400 Hz wide channels. The superimposed curve is a Gaussian of unit width, $\sim e^{-x^2/2}$.
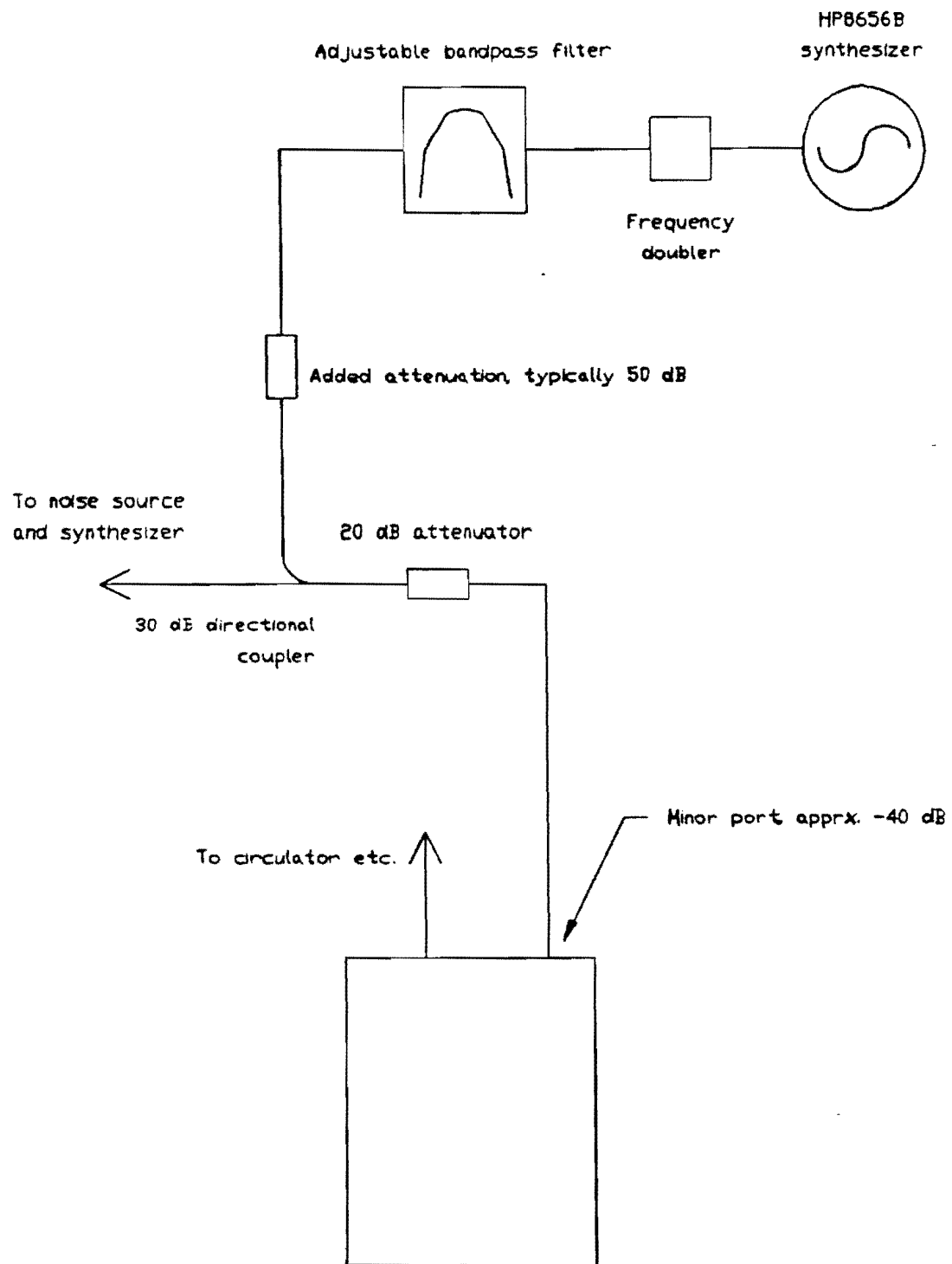
130

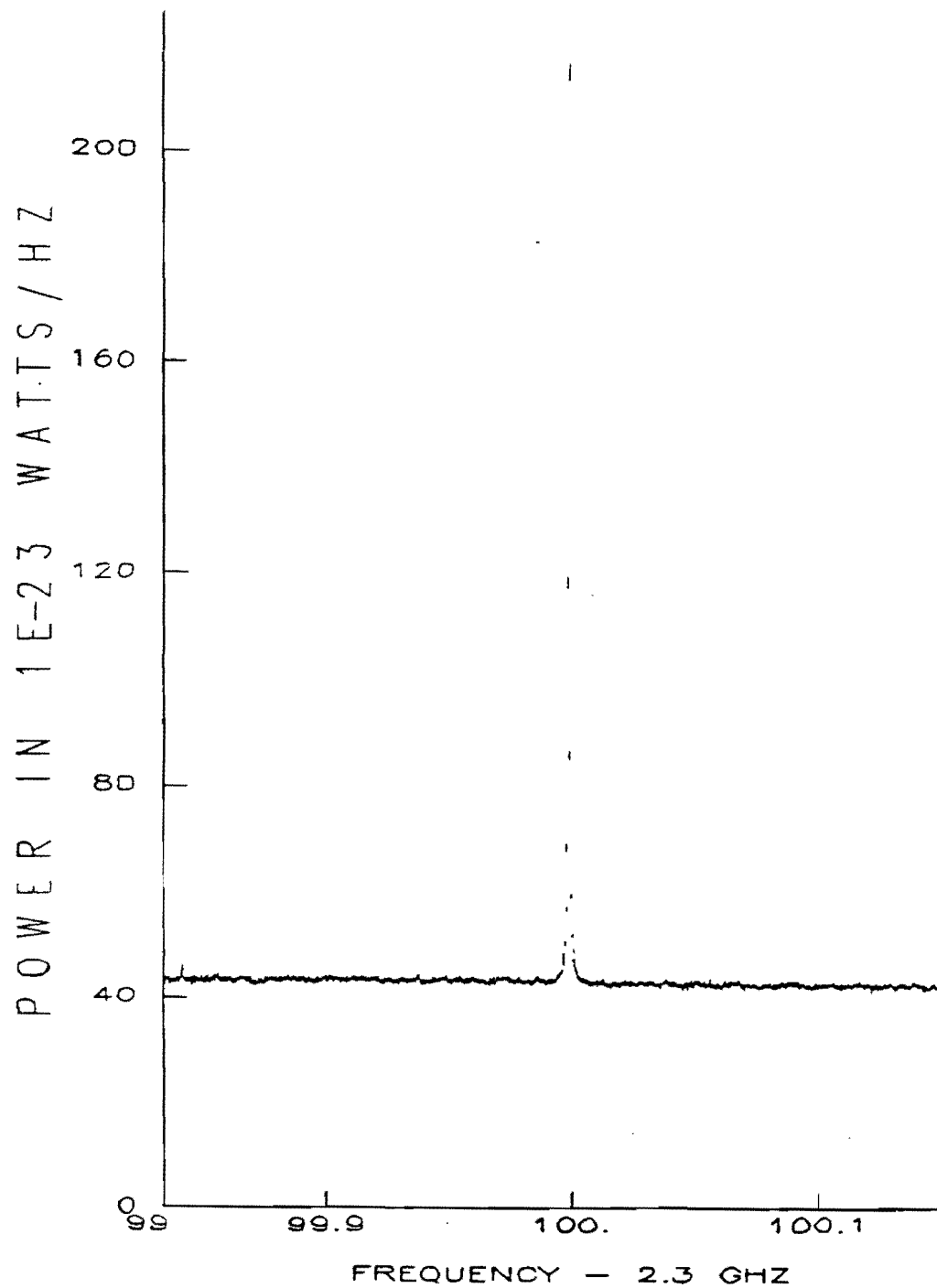Figure 5.5: Configuration of the apparatus for peak injection.

Figure 5.6: An injected peak at 2.400 000 000 GHz, the peak has a total power of $2 * 10^{-18}$ W.

despite the fact that the time standards of the signal generating and receiver synthesizers are independent.

As was mentioned, the tuning range of each cavity and tuning rod combination is swept over twice. The conversion of axions is a continuous process, unlike the expected signal from a magnetic monopole search, and the axion signal should be present every time data is taken at the appropriate frequency. The axion signal should therefore appear in the same frequency bins in coincidence in both sweeps. The requirement that a frequency bin have statistically high power levels in both sweeps greatly reduces the number of random candidate peaks which must be considered. In particular, if N_1 bins are found to be above a certain threshold in one sweep N_{tot} bins wide, and N_2 bins are found above the threshold in the second sweep then the expected number of coincidences, N_c, is equal to

$$N_c = N_1 \, N_2 \, / \, N_{tot}. \qquad\qquad (5.8)$$

One could also average the two sweeps together and choose the channels with highest statistical significance, or in fact take only a single sweep at half the sweep rate and pay overhead only once. It seems most advantageous, however, to consider the two sweeps separately and use the coincidence criterion. In particular, the previously mentioned structure caused by the imperfectly tuned multiplexer channels combined with non uniformities in sweep rate cause an excess of high σ events as can be seen in the tails of the

133

distributions shown in figures 5.3 and 5.4. By using the two sweeps, a certain amount of subjective judgement about the data can be incorporated to determine if the structure which causes the peak in at least one of the sweeps is caused by a recognizable idiosyncracy of the apparatus. Using this sort of judgment is not rigorous and does have pitfalls, but it ends complete dependance on a computer algorithm of unknown effectiveness, especially since the shape of the axion signal is not known. Eliminating peaks which are not caused by axions is necessary to determine whether any peaks could be caused by axions.

The actual job of finding coincident peaks is accomplished by a program called MATCH which is run after both sweeps have been completed. MATCH compares the statistically significant frequency bins in the ANA files from the two sweeps and then compiles its own list of peaks with specified levels of coincidence. Usually MATCH is run with a threshold of 4σ. The coincidences are compared within a window equal to twice the bin width. This is to compensate for the fact that the central frequency of the bins is probably not the same in both sweeps, and for any systematic errors caused by rounding[2]. Tables 5.2a to d contain a complete listing of coincident peaks which were found in the data; organized by cavity[3].

After both sweeps have been completed and MATCH has produced a list of coincident peaks, the experimenter must recheck them with the apparatus in an unswept mode to determine if any one of them does indeed represent a signal caused by the conversion of axions. During

134

COINCIDENCES ABOVE 5 SIGMA FOR CAVITY # 2

Typical sigma = 3×10^{-24} Watts/Hz

f (GHz)   DEV. RUN 2

Bin width = 200 Hz

f (GHz)	DEV. RUN 2
1.236761853	5.73
1.318580091	5.88
1.323649639	5.57
1.332724242	5.28
1.350727308	5.22
1.359858687	5.02
1.377900627	5.37
1.378214427	5.16
1.383166634	7.31
1.383198234	5.77
1.383965234	5.61
1.383992034	6.65
1.385641434	5.41
1.394035809	5.51
1.404080010	5.48
1.407927789	5.06

Table 5.2a: A complete list of coincident peaks which were rechecked with the appartus from data taken with cavity II.

COINCIDENCES ABOVE 4 SIGMA FOR CAVITY # 3

Typical sigma = 3 x 10^{-24} Watts/Hz

f (GHz)	DEV. RUN 1	DEV. RUN 2

Bin width = 400 Hz

1.468732600	5.87	4.45
1.493688400	4.05	4.07
1.507176400	6.98	4.01
1.622362823	4.49	4.09

Bin width = 800 Hz

1.494900600	6.46	4.11
1.499403800	4.28	4.07
1.511252200	4.27	4.09
1.513151000	4.61	4.02
1.564445399	4.80	10.26
1.618533024	5.67	3.75
1.659169025	9.31	4.01

Bin width = 1600 Hz

1.424814400	4.00	6.79
1.430335200	4.51	4.90
1.430445600	5.11	4.19

Table 5.2b: A complete list of coincident peaks which were rechecked with the appartus from data taken with cavity III.

1.499403800	4.39	4.20
1.610308624	4.04	4.48
1.610309424	4.85	4.48
1.680542422	4.30	4.57

Bin width = 3200 Hz

1.548771599	4.30	4.70
1.553998801	5.19	3.30
1.579774401	4.13	3.19
1.579776001	5.19	3.45

Table 5.2b: cont.

COINCIDENCES ABOVE 4 SIGMA FOR CAVITY # 4

Typical sigma = 3.1×10^{-24} Watts/Hz

.

f (GHz)	DEV. RUN 1	DEV. RUN 2
Bin width = 400 Hz		
1.697249000	4.64	5.01
1.791623800	4.16	4.47
1.799344800	5.10	4.62
1.805940000	5.64	4.42
1.810732600	6.02	5.24
1.834554200	4.46	4.47
1.858464600	4.10	4.52
1.878969600	4.02	4.24
Bin width = 800 Hz		
1.686463200	4.16	4.57
1.687325200	4.56	5.82
1.687652000	4.20	4.09
1.692627600	5.07	4.60
1.693280800	5.12	5.96
1.719659200	4.47	4.36
1.723439600	5.73	4.79
1.724834400	4.69	5.31
1.726788000	4.38	5.14
1.729365400	4.38	3.44
1.729379400	5.15	3.61
1.730332800	4.24	4.51

Table 5.2c: A complete list of coincident peaks which were rechecked with the appartus from data taken with cavity IV.

1.732164000	5.08	4.77
1.733459200	4.55	6.50
1.733793200	4.20	4.09
1.734228800	4.03	4.60
1.734316800	5.57	4.86
1.734645600	4.47	4.15
1.734671600	4.41	4.22
1.736217000	4.38	4.21
1.736292600	4.40	4.63
1.736841800	4.31	4.41
1.737780200	5.26	3.03
1.738330600	5.02	5.41
1.738739400	4.86	4.49
1.738929000	4.42	4.14
1.739701400	5.46	4.48
1.740866200	4.50	4.04
1.741106600	4.43	4.91
1.742142400	7.80	5.97
1.744353000	4.52	4.54
1.745491000	4.77	4.57
1.745719000	4.45	4.22
1.745733000	4.15	4.24
1.751985000	4.25	4.00
1.754739400	5.06	4.14
1.756301600	4.36	4.39
1.792515200	4.14	4.01
1.799970200	4.21	7.05
1.803355000	4.33	5.21
1.807754800	4.32	4.21
1.817667200	5.11	4.80
1.819897200	4.24	4.22
1.841066200	4.28	4.47
1,872342200	3.43	4.37
1.932907600	4.56	4.95
1.934348000	5.66	4.81
1.937250000	4.49	4.46
1.941934000	4.37	5.39
2.945816400	4.28	4.88
2.046406400	4.03	4.99
2.052117200	4.28	4.96
2.062212200	5.83	6.63
2.069301800	4.18	4.64
2.071536200	3.74	4.15
2.082717800	4.03	5.07

Table 5.2c: cont.

Bin width = 1600

    1.964082000   4.03   4.59

Bin width = 3200
                                        .

    2.084968600   7.11   4.09

COINCIDENCES ABOVE 4 SIGMA FOR CAVITY # 5

Typical sigma = 3.5 x 10^{-24} Watts/Hz

f (GHz)	DEV. RUN 1	DEV. RUN 2

Bin width = 400 Hz

f (GHz)	DEV. RUN 1	DEV. RUN 2
2.029179433	8.75	4.56
2.270325855	4.43	4.74
2.365800034	5.13	4.23
2.371142835	4.98	5.23
2.384048106	6.62	4.03

Bin width = 800 Hz

f (GHz)	DEV. RUN 1	DEV. RUN 2
1.967561175	4.94	4.96
2.074141645	5.68	4.42
2.077902445	4.15	4.11
2.284426086	4.64	4.31
2.230859064	5.03	4.62
2.370111835	11.81	6.61
2.396625505	4.03	4.34
2.439500151	4.03	4.13
2.442431350	4.04	4.14
2.455374390	4.28	4.31
2.456531081	4.56	5.56

Bin width = 1600 Hz

f (GHz)	DEV. RUN 1	DEV. RUN 2
1.952657432	6.29	5.00
1.993201006	4.56	4.09

Table 5.2d: A complete list of coincident peaks which were rechecked with the appartus from data taken with cavity V.

2.005008604	4.16	4.50
2.019540463	4.22	4.30
2.254244073	4.35	4.12
2.254245673	4.38	4.50
2.256132073	5.25	4.24
2.322403465	5.15	4.19
2.324896265	2.88	4.12
2.333367005	4.04	4.06
2.354930708	4.81	4.64
2.390783104	4.75	4.05

Bin width = 3200 Hz

|		
2.005008604	4.04	4.70
2.006587804	4.84	4.02
2.017718063	5.44	4.40
2.273083256	4.35	4.36

Table 5.2d: cont.

142

peak checking the cavity is left tuned to the frequency of the suspect peak and the first local oscillator is set, fixed, to the appropriate frequency. There is an important change in the apparatus during peak checking; rather than using the multiplexer, an HP 3561A FFT dynamic signal analyzer is used for final detection. As was mentioned earlier, the different multiplexer channels have slightly different responses to a flat noise spectrum. When the frequency of the multiplexer is not swept this lack of flatness becomes unacceptably large. Also, when the frequency of the first local oscillator is not being swept, a particular IF frequency corresponds to a fixed RF frequency and therefore need only be averaged with itself during data taking, not shifted. For this reason, it is preferable to use the FFT.

The HP 3561A has extensive internal averaging capabilities and will average an arbitrary number of power spectra. The number of averages is chosen so that the sensitivity achieved with the FFT exceeds that of the original data in which the suspect peak was found. When the average is complete, the power spectrum is checked to see if the suspect peak has reappeared. In general no signal is found, indicating that the suspect peak was probably a statistical fluctuation in the power spectrum. However, if the peak does reappear, a number of tests can be applied to determine its origin. First, the cavity is retuned away from the peak without changing the frequency of the local oscillator. Data are taken and if the peak persists then it is probably a result of pickup in the electronics

chain and is definitely not due to the conversion of axions. This test has eliminated all of the suspect peaks in the data so far which were determined not to be caused by statistical fluctuations.

Any peak which depended on cavity tune would be further tested by its dependence on magnetic field: the power of the signal should depend on the square of the magnetic field as per equation 2.15. Figure 5.7 shows a peak in coincidence in two sweeps at a frequency of 1.564 445 600 GHz and figure 5.8 shows the same peak as it appeared when checked with the FFT. The peak remained after detuning the cavity and so was determined not to be due to the conversion of axions. The precise source of the signal was not determined, but was probably due to pickup of a microwave emission in the lab. Figure 5.9 shows a very clear peak at 2.235 006 422 GHz which appeared in the first sweep of cavity V, .400 rod, but not in the second. Because of the specific frequency, the source of the signal was determined to be another synthesizer in the lab which was being used for a preamplifier test.

In this way all of the frequencies listed in tables 5.2a to g have been eliminated. The only limit to the number of peaks which can be checked is the patience of the experimenter. The practical solution to the peak checking procedure is to check all peaks above a certain threshold in the number of standard deviations the peak represents. If the axion signal is not found in the data, then a limit on the axion signal power is set which is equal to the power

144
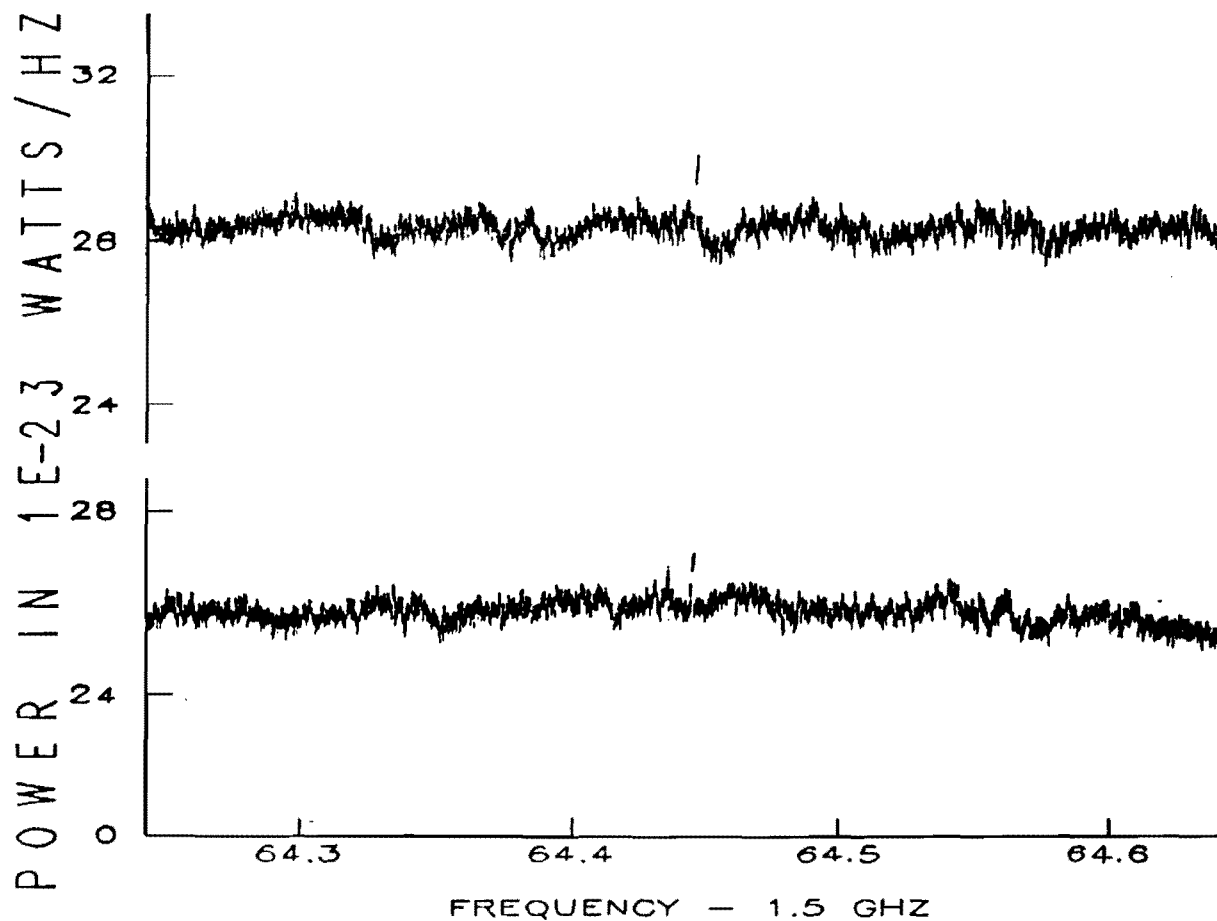
Figure 5.7: A signal which appeared in coincidence in both sweeps (the upper trace is sweep 1 and the lower is sweep 2). The peak appeared at 1.564 445 600 GHz, in cavity III, .400 rod.
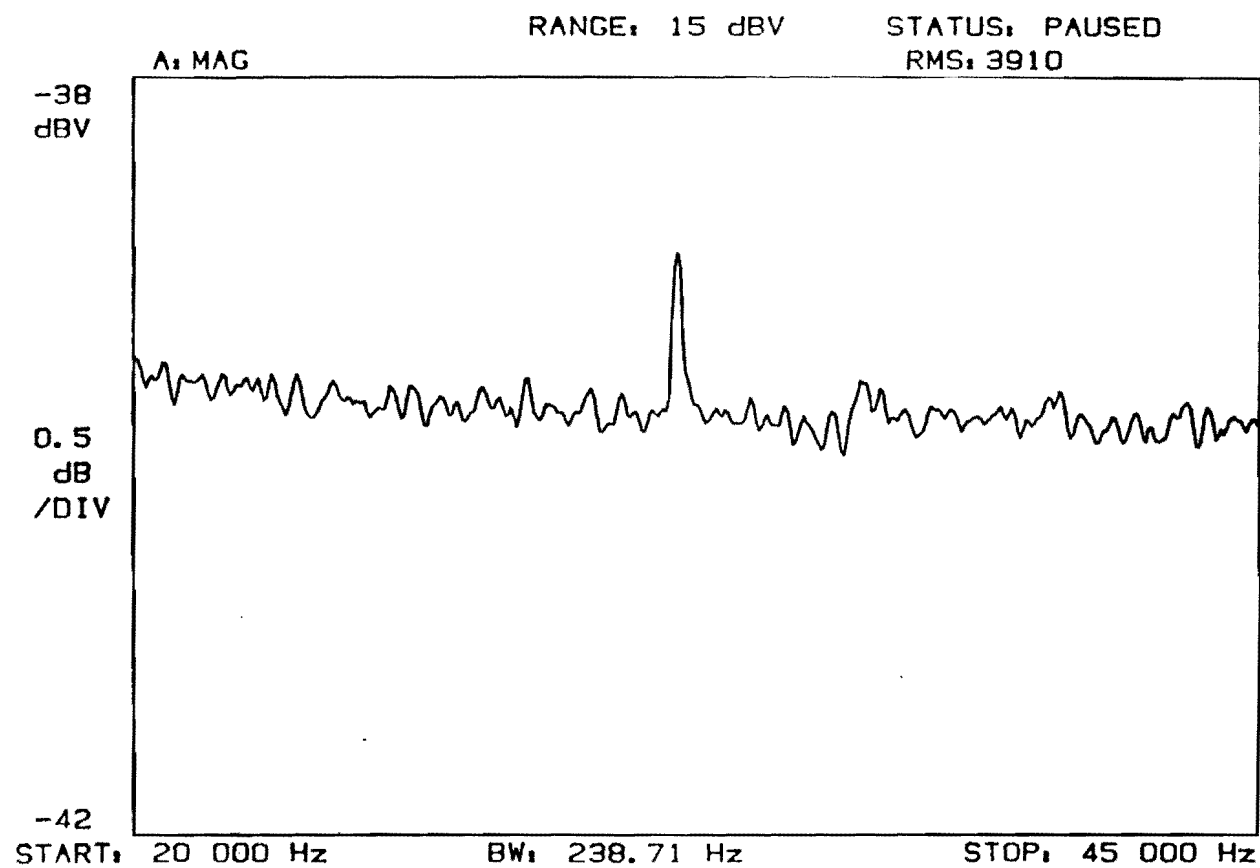
RANGE: 15 dBV   STATUS: PAUSED
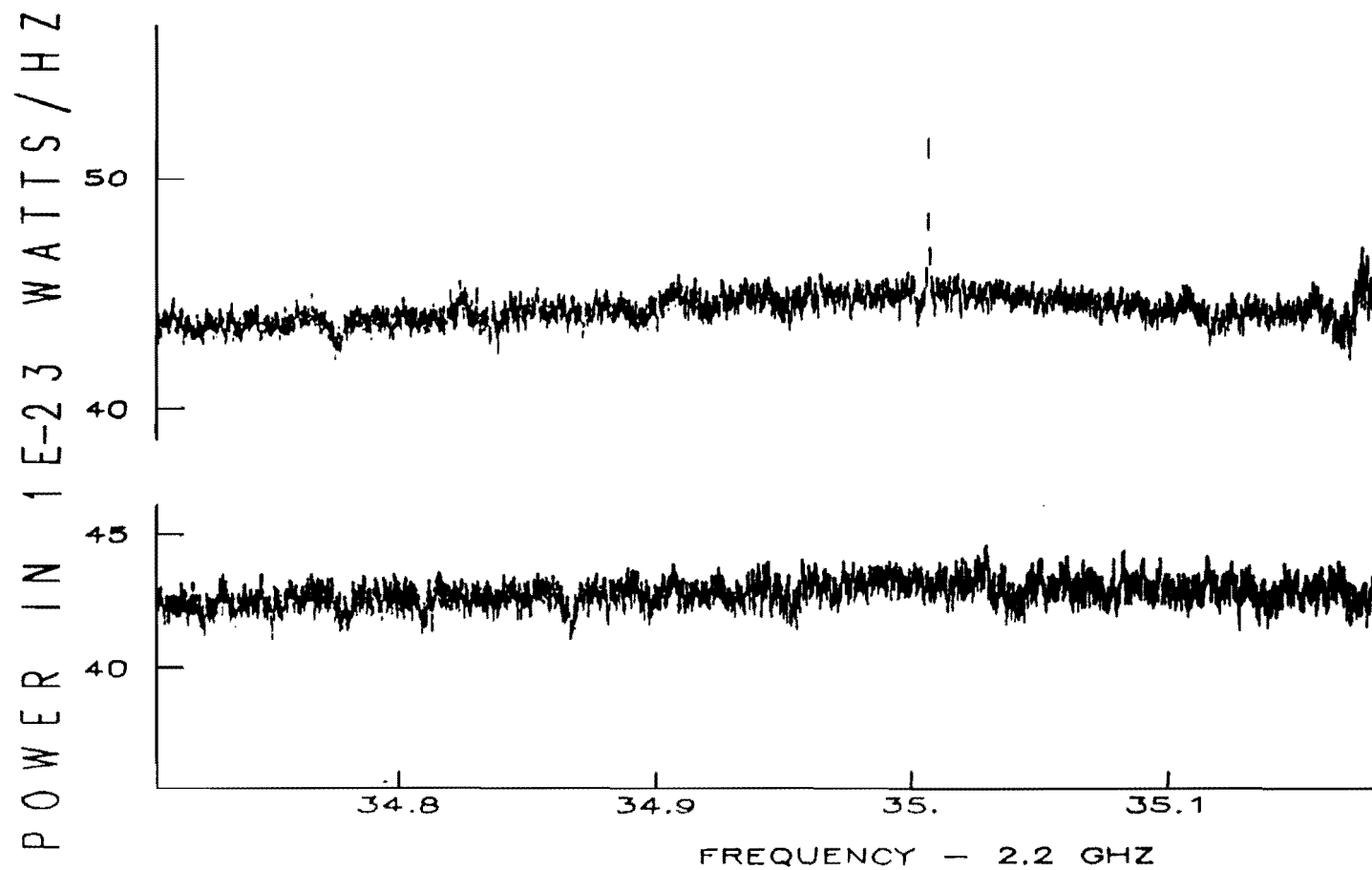
A: MAG   RMS: 3910

Figure 5.8: The 1.564 445 600 GHz signal on the FFT.

Figure 5.9: A 2.235 006 422 GHz signal which appeared in the first sweep, upper trace, but not the second, lower trace, of cavity V, .250 rod.

level corresponding to the number of standard deviations to which peaks were checked, $P = \sigma n_\sigma \Delta f$. As can be seen from table 5.2, the coincidence threshold was usually 4σ, or about 5×10^{-24} W/Hz. Such a limit has a 50% confidence level. On the other hand, if a limit is made based on a power level which is 2σ's higher then the confidence level improves to 97%[4].

5.4 Wide Axions

In the preceding arguments it was assumed that the width of the axion signal would be approximately equal to that of a single multiplexer channel. However, it may be that the axion signal width has been underestimated and may be larger than $Q_a = 3 \times 10^6$. It is possible to use the data to search for, and to place limits on, wider axion signals. This is done by combining a number of adjacent bins together and then applying the single bin analysis techniques directly. Analysis is typically performed on 1, 2, 4, and 8 multiplexer channel widths, corresponding to axion Q's of $3 \times 10^5 \leq Q_a \leq 3 \times 10^6$. The only added complication encountered when analyzing wide axions is that the analysis must be repeated with a shift in which bins are added together. For example, in the case of two-bin wide axions one can add bins 1+2, 3+4,... or bins 2+3, 4+5,... If a signal had a spectrum which covered channels 4 and 5, the latter bin combination method would show the peak more clearly because the signal would be spread over two channels in the former combination.

148

Histograms for the distribution of deviations from the mean for 800, 1600 and 3200 Hz wide bins for the data taken with cavity III are shown in figure 5.10a to c. The width of signals searched for is limited by the presence of the $\approx$ 50 bin undulations in the data which create a large background of false peaks. In addition, the limit on axion signal power becomes worse because the accumulated noise power in the many channels which are added together becomes larger, while the expected axion signal power remains constant. A listing of coincident wide axions can be found in Tables 5.2a to d. As with the single channel axions, all coincident peaks have been determined not to be due to axions. Although not actually an axion signal, figure 5.11 shows a wide signal in the data.
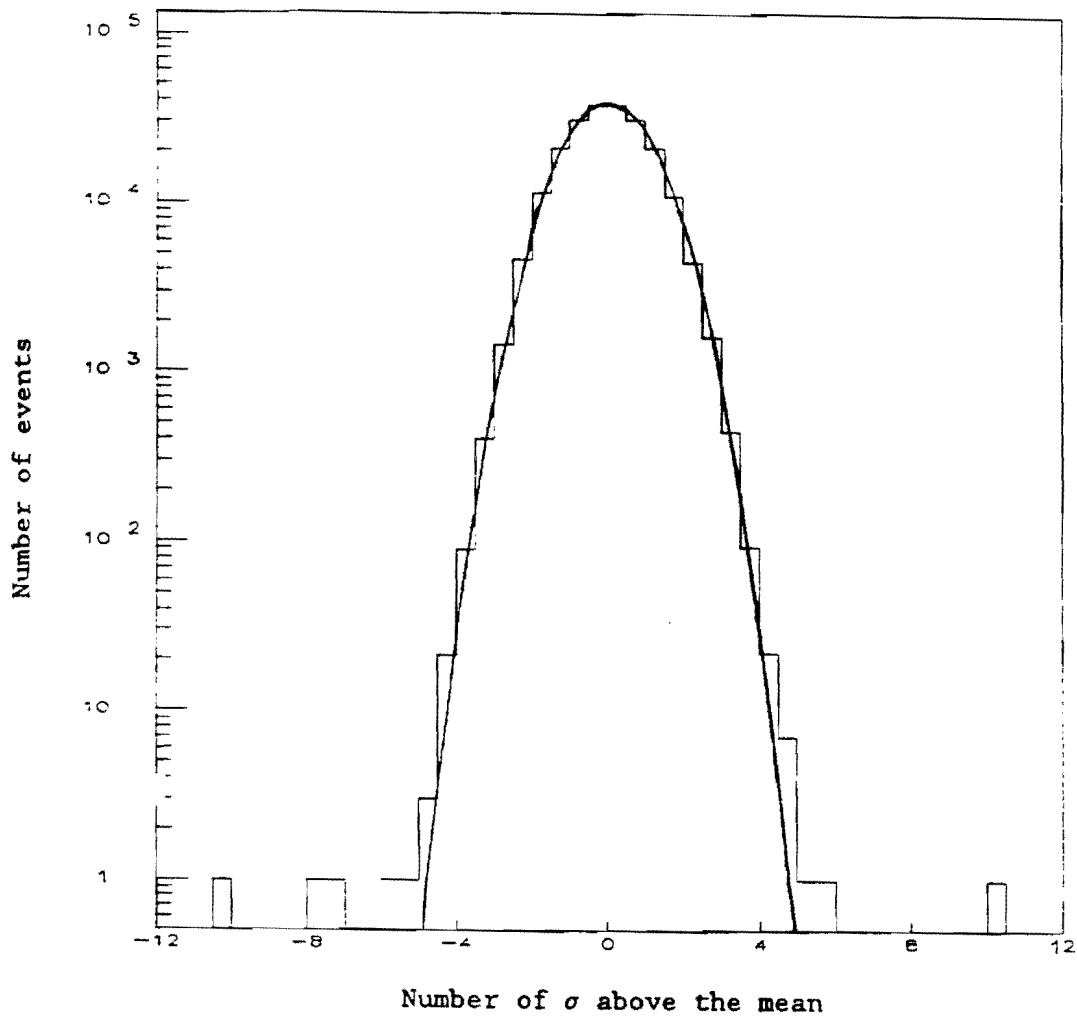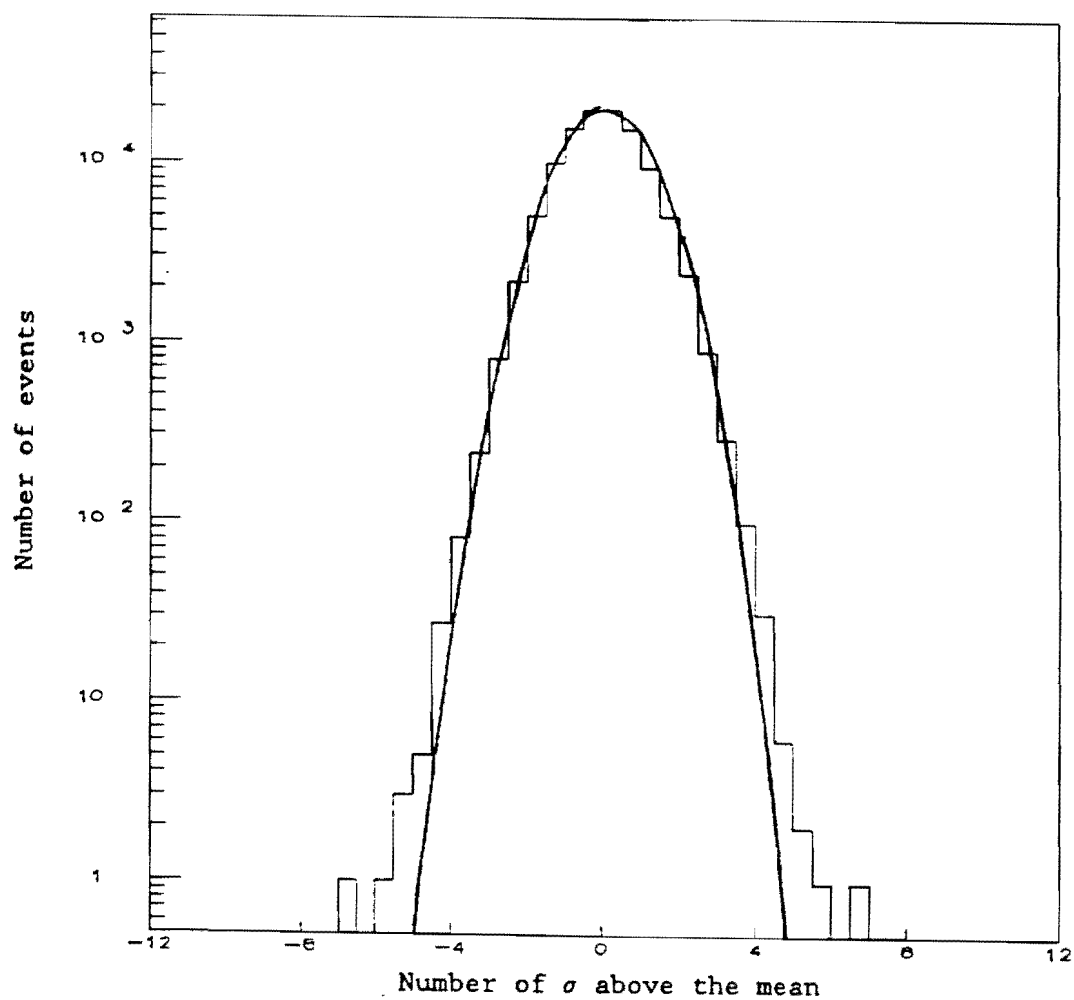
Figure 5.10a: Distribution of bin power levels in terms of a locally calculated mean an σ for cavity III, .400 rod, for 800 Hz wide bins. The superimposed curve is a Gaussian of unit width, $e^{-x^2/2}$.

Figure 5.10b: Distribution of bin power levels in terms of a locally calculated mean an σ for cavity III, .400 rod, for 1600 Hz wide bins. The superimposed curve is a Gaussian of unit width, $\sim e^{-x^2/2}$.
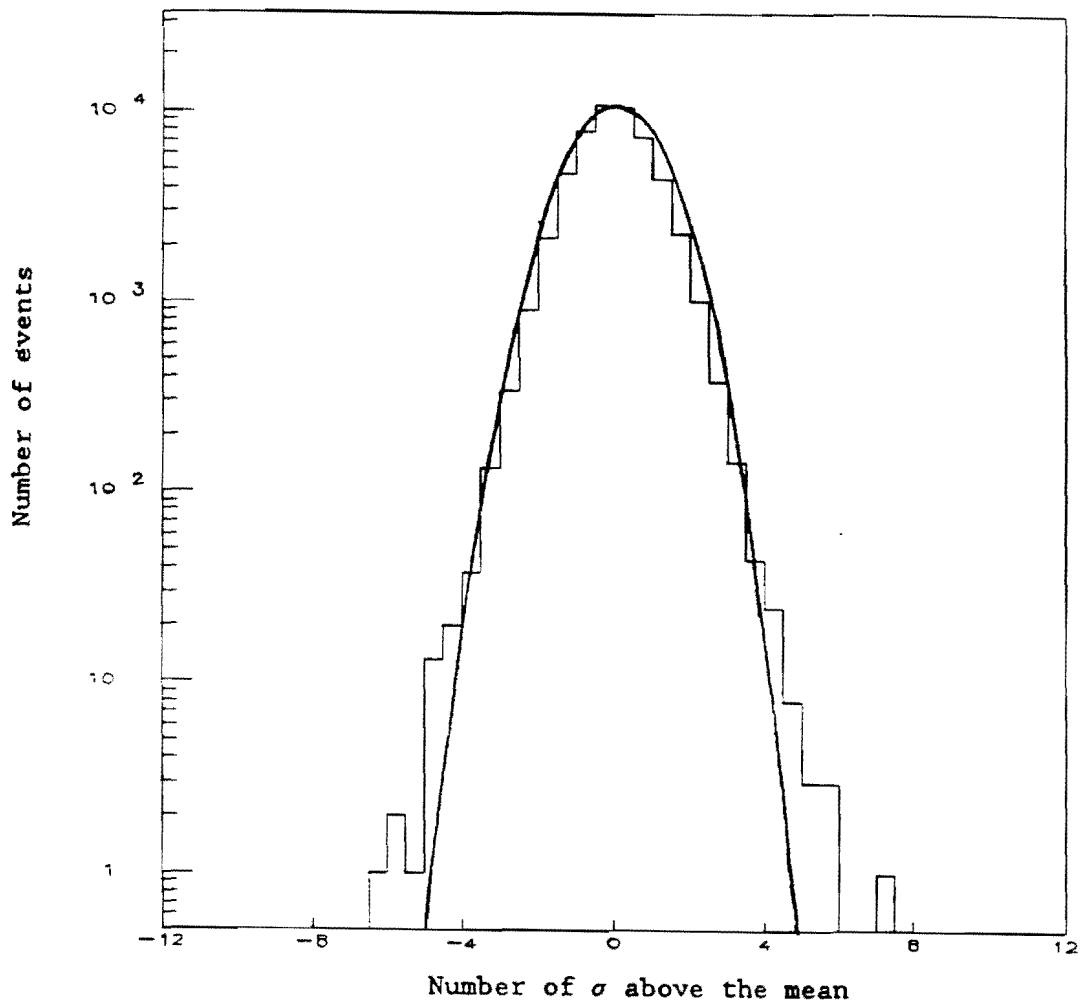
Figure 5.10c: Distribution of bin power levels in terms of a locally calculated mean an σ for cavity III, .400 rod, for 3200 Hz wide bins. The superimposed curve is a Gaussian of unit width, $\sim e^{-x^2/2}$.
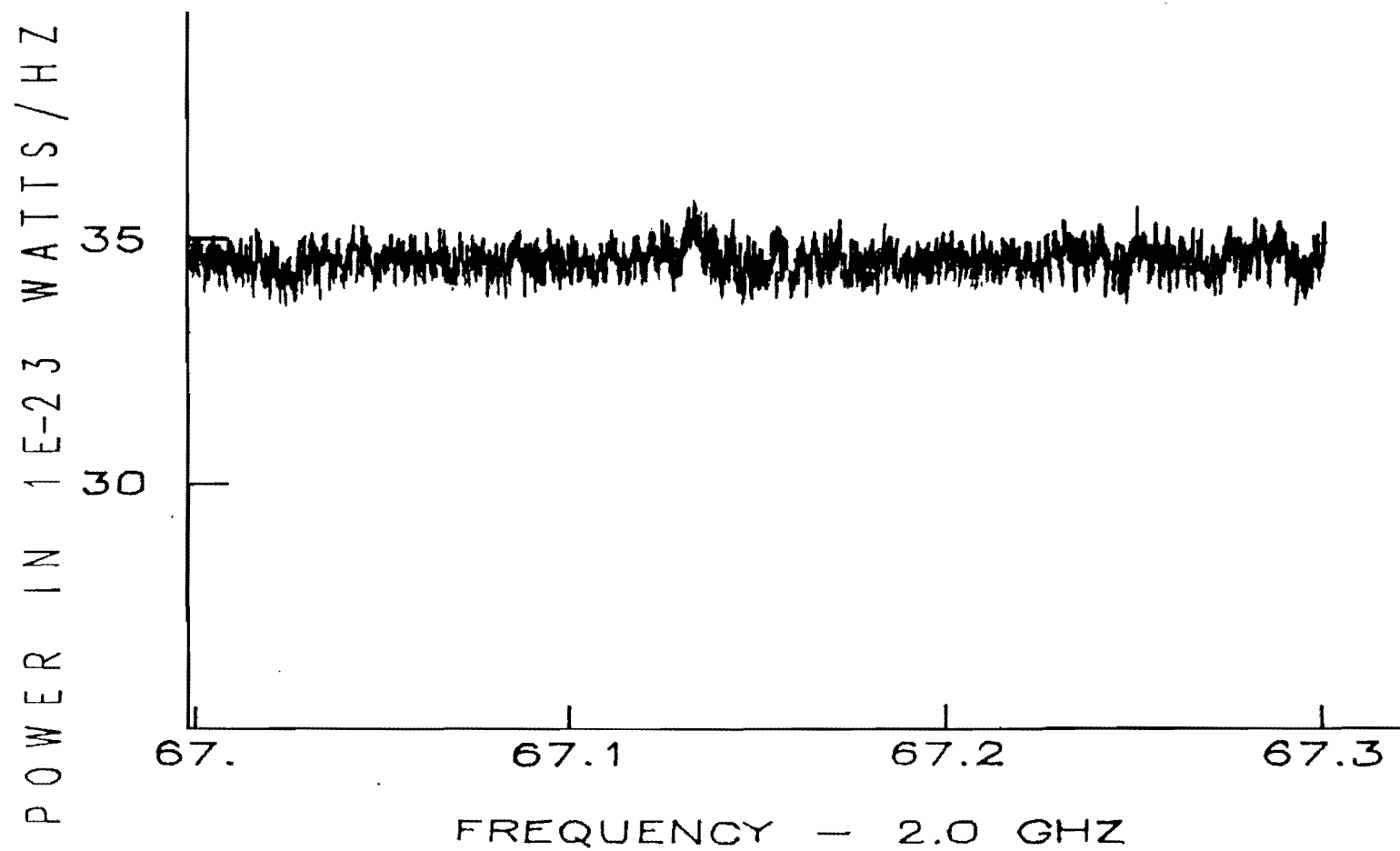
152

Figure 5.11: A wide signal in the data.

References

1. The reason for this is purely coincidental. Because the full tuning range of a cavity is approximately 15% of its untuned frequency, and the multiplexer channel widths are chosen to be about 3×10^{-7} of the untuned frequency, the sweep rate needed to cover the tuning range of a cavity in a fixed time is constant for all cavities in terms of multiplexer bandwidths per second.

2. To be precise, it is possible that the 400 Hz bins in a first sweep fell in such a way that a signal much narrower than a multiplexer channel width was really in the extreme high end of the frequency bin centered on 2 GHz. If in the second sweep the frequency bins fell slightly lower in frequency so that the peak would appear in a frequency bin with a central frequency 2 GHz + 400 Hz - ϵ (the signal would be in the extreme low end of the bin). This error can happen in both directions, thus the 2 bin-width window.

3. Only one sweep was taken with cavity II with the circulator. That sweep was so much better than the other that it did not make sense to use any coincidence criteria. Therefore only peaks above a threshold in the circulator run were used.

4. The chance that a peak with a 6σ power level would appear as a 4σ peak or less is equal to the probability that the noise has a fluctuation in excess of -2σ. The probability of this occurring is 97%.

154

Chapter 6: Results and Conclusions

6.1 Limits on Axion Coupling

The absence of an axion signal at the sensitivity level of the apparatus sets a limit on the product of the local axion density, $\langle \rho_a \rangle$, and the axion coupling, $g_{a\gamma\gamma}$, for the frequency range which has been covered. The limit on density and coupling for a given axion width is derived from the power level, $\sigma n_\sigma \Delta f$, corresponding to the number of σ's to which coincident peaks were checked plus an additional 2σ to establish a 97% confidence level. In particular, 6σ power level limits for axions 400, 800, 1600, and 3200 Hz wide were produced for the frequency ranges of cavities III, IV, and V. The data from cavity II were not checked in coincidence, instead, 7σ limits for linewidths of 200, 400, 800, and 1600 Hz were produced. The limit on $(g_{a\gamma\gamma}/m_a)^2 \langle \rho_a \rangle$, a dimensionless quantity, is given by the equation,

$$\left(\frac{g_{a\gamma\gamma}}{m_a} \right)^2 \langle \rho_a \rangle < n_\sigma \ \frac{\mu_0}{\pi} \ \frac{1}{B_0^{\,2}V} \frac{\sigma \Delta f}{CQ_Lf} \frac{1}{G^2} \tag{6.1}$$

where n_σ is the number of sigma threshold to which peaks were checked plus 2, σ is the power density of a 1σ peak (in W/Hz), and Δf is the axion width one is searching for. Through the term Δf, one can directly see how the experiment becomes less sensitive to wider axions. C is a term approximately equal to .9, which compensates for

155

the fact that axion production is less efficient when the axion frequency does not precisely coincide with the center of the cavity resonance. C is given by

$$C = \frac{\Delta f_c}{\Delta f_m} \tan^{-1}(\Delta f_m/2\Delta f_c) \qquad (6.2)$$

where Δf_m is the total width of the multiplexer (all 64 channels), and Δf_c is the cavity bandwidth. The terms of equation 6.1 vary as a function of frequency because of the use of different cavities, cryogenic preamplifiers, and external magnetic fields for runs over different frequency bands. In addition, variation in cavity Q, filling factor, preamplifier noise temperature, and sweep rate within a particular run cause variation with frequency in the limits set by equation 6.1. Thus, equation 6.1 has been evaluated for each data set using known parameters of the experiment and the measured values of σ. These results are summarized in table 6.1. As examples, the variation of the cavity Q and volume with frequency are also shown graphically in figures 6.1 and 6.2, respectively. The limit on $(g_{a\gamma\gamma}/m_a)^2\langle\rho_a\rangle$ lies in the range of 10^{-40} to a few times 10^{-40}.

Since the ratio $(g_{a\gamma\gamma}/m_a)$ is fixed by the axion model, a limit on $g_{a\gamma\gamma}$ alone can be derived from equation 6.1. If one assumes a local dark matter density, $\langle\rho_a\rangle = 300$ MeV/cm^3 for DFS axions then,

$$g_{a\gamma\gamma} = \left[\left[\frac{g_{a\gamma\gamma}}{m_a} \right]^2 \langle\rho_a\rangle \right]^{1/2} \frac{f}{1\text{GHz}} \ 2.73 \times 10^6 \ \text{GeV}^{-1}. \qquad (6.3)$$

156

Cavity II, .585 Rod

$$V = 8.01 \times 10^{-3} \text{ m}^3 \qquad \Delta f = 200 \text{ Hz} \qquad B_0 = 5.8 \text{ T}$$

7σ limits

f [GHz]	$\dfrac{\sigma \Delta f}{C Q_L f}$ [W/Hz]	C^2	Upper limit $(g_{a\gamma\gamma}/m_a)^2 \rho_a$	Upper limit $g_{a\gamma\gamma}$ [GeV^{-1}]
1.218-1.32	10×10^{-36}	.50	2.1×10^{-40}	5.0×10^{-14}
1.32-1.415	13×10^{-36}	.50	2.7×10^{-40}	5.8×10^{-14}

Cavity III, .585 Rod

$$V = 5.65 \times 10^{-3} \text{ m}^3 \qquad \Delta f = 400 \text{ Hz} \qquad B_0 = 7.5 \text{ T}$$

6σ limits

f [GHz]	$\dfrac{\sigma \Delta f}{C Q_L f}$ [W/Hz]	C^2	Upper limit $(g_{a\gamma\gamma}/m_a)^2 \rho_a$	Upper limit $g_{a\gamma\gamma}$ [GeV^{-1}]
1.414-1.45	20×10^{-36}	.45	2.2×10^{-40}	5.9×10^{-14}
1.45-1.512	14×10^{-36}	.40	1.8×10^{-40}	5.4×10^{-14}

Table 6.1: Parameters and limits.

157

Cavity III, .400 Rod

$$V = 5.65 \times 10^{-3} \text{ m}^3 \qquad \Delta f = 400 \text{ Hz} \qquad B_0 = 7.5 \text{ T}$$

6σ limits

f [GHz]	$\dfrac{\sigma\Delta f}{CQ_L f}$ [W/Hz]	G^2	Upper limit $(g_{a\gamma\gamma}/m_a)^2 \rho_a$	Upper limit $g_{a\gamma\gamma}$ [GeV^{-1}]
1.513-1.60	15×10^{-36}	.48	2.5×10^{-40}	6.3×10^{-14}
1.60-1.687	13×10^{-36}	.48	2.3×10^{-40}	6.2×10^{-14}

Cavity IV, .400 Rod

$$V = 3.72 \times 10^{-3} \text{ m}^3 \qquad \Delta f = 400 \text{ Hz} \qquad B_0 = 7.5 \text{ T}$$

6σ limits

f [GHz]	$\dfrac{\sigma\Delta f}{CQ_L f}$ [W/Hz]	G^2	Upper limit $(g_{a\gamma\gamma}/m_a)^2 \rho_a$	Upper limit $g_{a\gamma\gamma}$ [GeV^{-1}]
1.761-1.90	20×10^{-36}	.49	5.0×10^{-40}	7.9×10^{-14}
1.90-2.087	23×10^{-36}	.54	5.1×10^{-40}	10×10^{-14}

Table 6.1: continued

Cavity IV, .585 Rod

$$V = 3.72 \times 10^{-3} \, m^3 \qquad \Delta f = 400 \, Hz \qquad B_0 = 7.5 \, T$$

$$6\sigma \text{ limits}$$

f [GHz]	$\dfrac{\sigma \Delta f}{CQ_L f}$ [W/Hz]	G^2	Upper limit $(g_{a\gamma\gamma}/m_a)^2 \rho_a$	Upper limit $g_{a\gamma\gamma}$ [GeV^{-1}]
1.686-1.72	10×10^{-36}	.45	1.7×10^{-40}	6.1×10^{-14}
1.72-1.764	12×10^{-36}	.40	2.3×10^{-40}	7.2×10^{-14}

Cavity V, .400 Rod

$$V = 2.67 \times 10^{-3} \, m^3 \qquad \Delta f = 400 \, Hz \qquad B_0 = 7.5 \, T$$

$$6\sigma \text{ limits}$$

f [GHz]	$\dfrac{\sigma \Delta f}{CQ_L f}$ [W/Hz]	G^2	Upper limit $(g_{a\gamma\gamma}/m_a)^2 \rho_a$	Upper limit $g_{a\gamma\gamma}$ [GeV^{-1}]
1.952-2.10	22×10^{-36}	.50	7.0×10^{-40}	15×10^{-14}
2.10-2.250	32×10^{-36}	.50	11×10^{-40}	20×10^{-14}

Table 6.1: continued

159

Cavity V, .250 Rod

$$V = 2.67 \times 10^{-3} \text{ m}^3 \qquad \Delta f = 400 \text{ Hz} \qquad B_0 = 7 \text{ T}$$

6σ limits

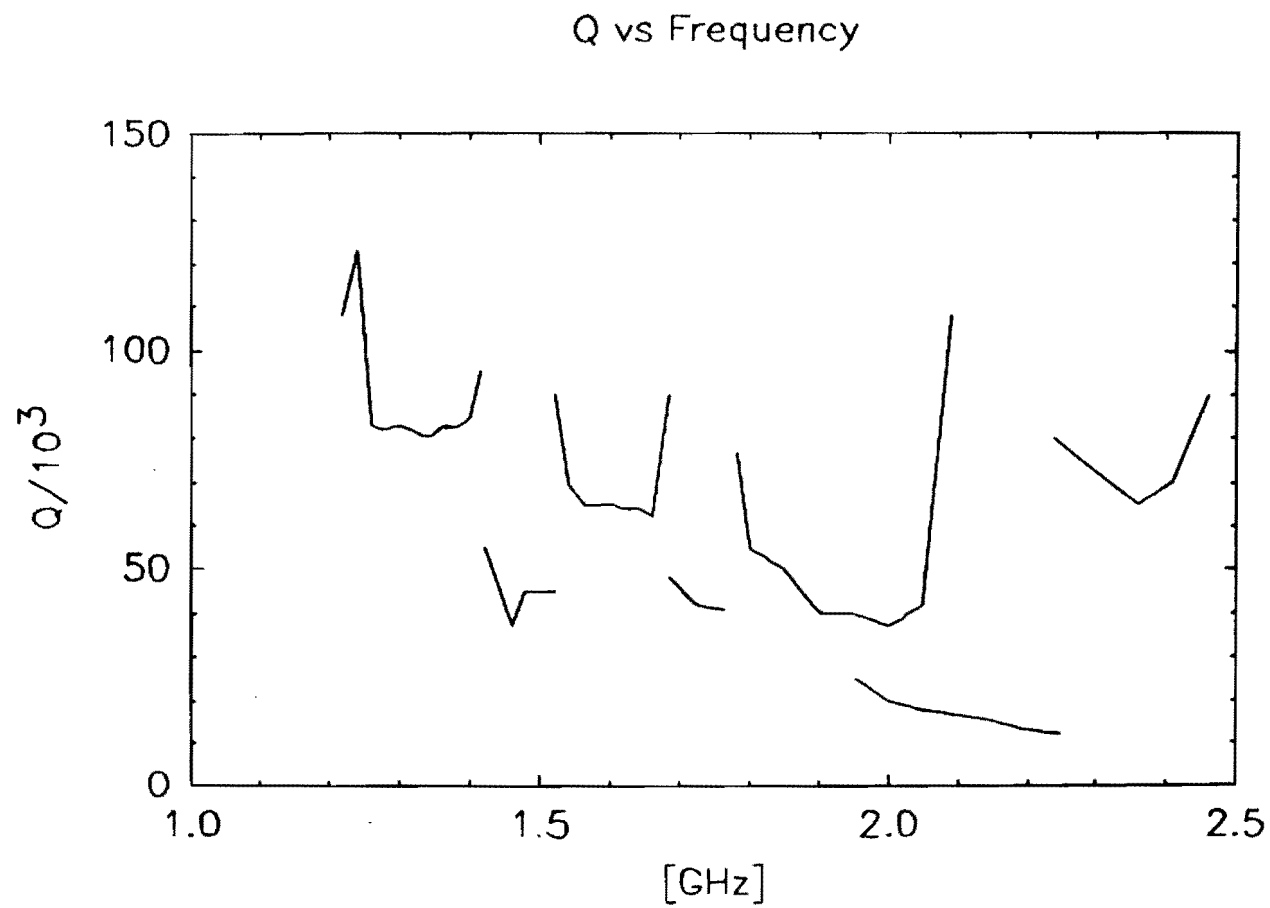| f [GHz]	$\dfrac{\sigma \Delta f}{CQ_L f}$ [W/Hz]	G^2	Upper limit $(g_{a\gamma\gamma}/m_a)^2 \rho_a$	Upper limit $g_{a\gamma\gamma}$ [GeV^{-1}]
2.239-2.36	4.7×10^{-36}	.45	1.8×10^{-40}	7.8×10^{-14}
2.36-2.460	5.5×10^{-36}	.65	1.6×10^{-40}	8.3×10^{-14}

Table 6.1: continued

Q vs Frequency

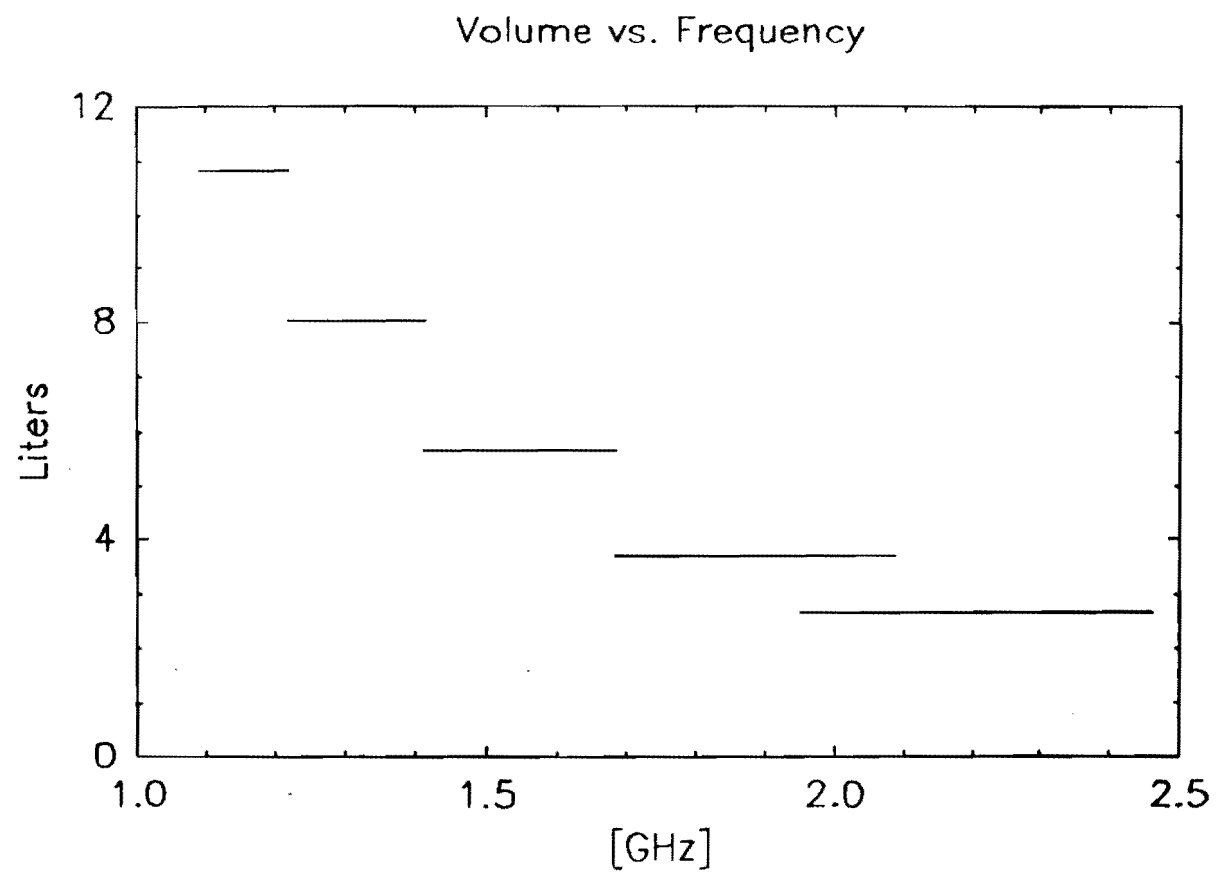Figure 6.1:   Loaded Q vs. frequency.

Volume vs. Frequency

Figure 6.2: Cavity volume vs frequency.

When all of the values in tables 6.1a to g are combined together using equations 6.1 and 6.3, a limit on coupling as a function of axion mass results, for a particular axion width. This limit can be plotted, as shown in figure 6.3[1]. Typical values of $g_{a\gamma\gamma}$ are in the range of 10^{-14} GeV^{-1}. Also included in the figure are two lines which correspond to the expected coupling of DFS and Hadronic axions respectively. From this one can see that the experiment has failed to reach the theoretically expected $g_{a\gamma\gamma}$ typically by a factor 17. However, the limit is phenomenally sensitive in terms of known couplings; for example the corresponding coupling of the weak interaction is $g_w \approx 10^{-2}$ GeV^{-1}.

6.2 Possible Improvements

In order to reach the expected coupling strength, the sensitivity of the experiment to an axion signal could be improved both by reducing the noise temperature of the receiver system, i.e. the cryogenic preamplifier, and by increasing the expected signal level by increasing any of the parameters, B_0, Q, or V of equation 2.16. One of the most desirable improvements would be an increase in the magnetic field, since the expected signal power increases as the square of the field, and since the single improvement would be effective across the entire frequency range of the search (if the dimensions of the bore could be maintained). However, current technology limits this improvement of our 8.5 T field to about 15 T.
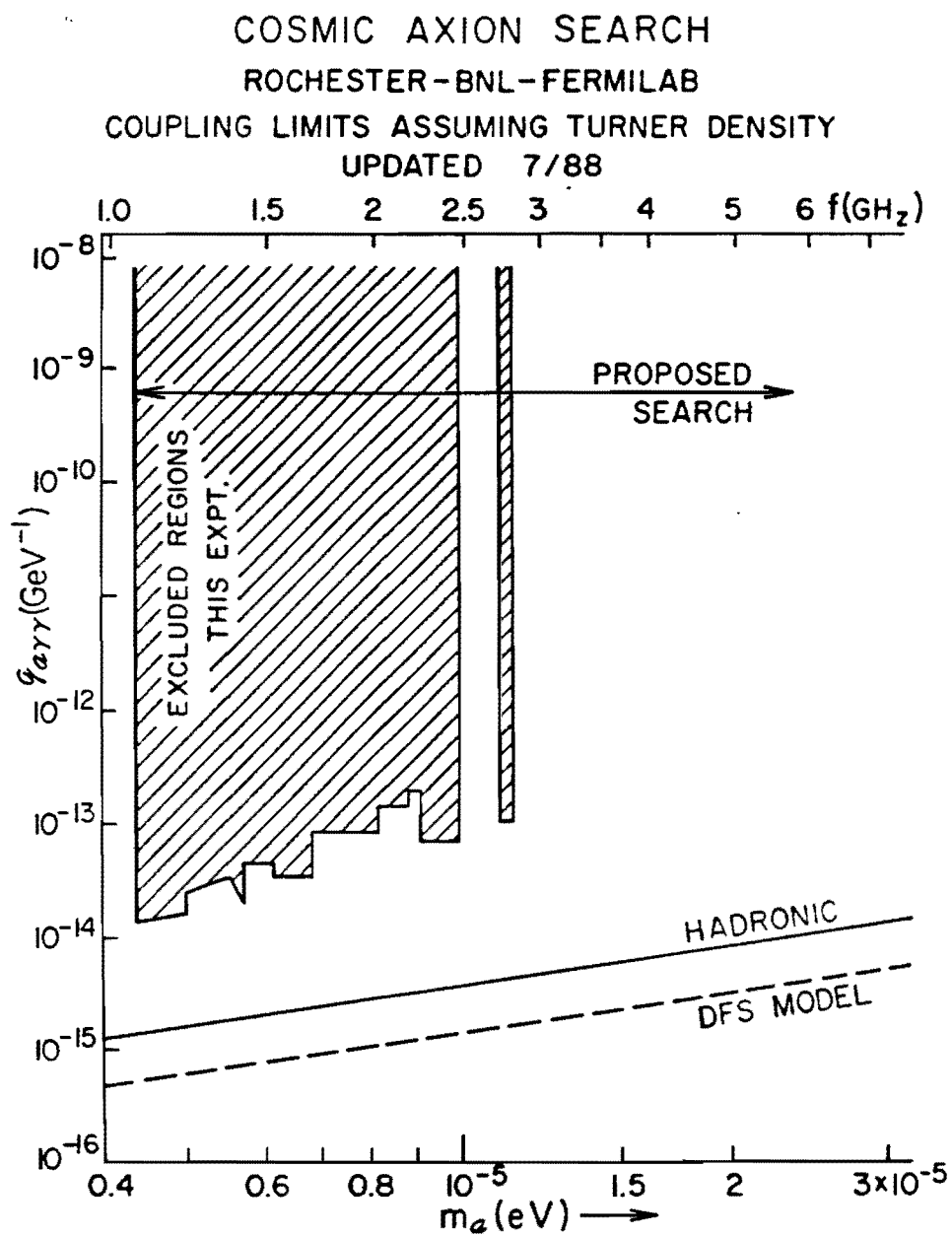
163

COSMIC AXION SEARCH
ROCHESTER-BNL-FERMILAB
COUPLING LIMITS ASSUMING TURNER DENSITY
UPDATED 7/88

Figure 6.3: The bottom line.

Improvement in the cavity Q would be possible through the use of superconducting cavities, but the cavities would have to function in a high magnetic field and would have to allow the penetration of the flux of the applied field into the cavity. Increasing the volume of the cavity without increasing the resonant frequency of an appropriate mode is possible through a variety of schemes. However, it seems that this inevitably results in an increased density of modes, since one is no longer using a fundamental mode, and all of the associated mode crossing problems. Some improvement of the noise temperature of the preamplifier is possible by using more exotic devices such as masers. However, this only results in an improvement on the order of a factor 5 and must be repeated consistently to cover the full frequency band of 1 to 30 GHz. In addition, such improvement is profitable only to the point where the noise temperature of the preamplifier is a bit less than the physical temperature of the microwave cavity, since the system noise temperature is determined by the sum of these two temperatures. A reduction in the temperature of the cavity could be accomplished either by pumping on the helium bath or by using a dilution refrigerator. However, all of the improvements which have been mentioned represent large technical challenges and are probably not worthwhile unless, perhaps, a more restrictive estimate of the axion mass could be found. In this case, an increase in sensitivity can also be accomplished by increasing the averaging time.

To avoid the difficulties of the improvements which have been

mentioned, alternative methods of probing for the existance of axions have been proposed. For example, members of our group have begun an experiment which seeks to produce axions through the interaction of an intense laser with a magnetic field. The expected sensitivity of the experiment to the coupling of axions to photons is of the order of $g_{a\gamma\gamma} \sim 10^{-8}$ GeV^{-1} but it is over a very wide mass range, up to about 10^{-3} eV, and is not dependant on the existance of halo axions.

6.3 Conclusions

A narrow axion signal has been searched for by our group in the frequency range $1.22 < f < 2.46$ GHz. Combined with previously reported results[2] we can exclude the existence of axions which make up the dark matter halo in the mass range of $.45 \times 10^{-5} < m_a < 1 \times 10^{-5}$ eV provided that there is a density $\langle \rho_a \rangle \geq 300$ MeV/cm^3 and that the coupling $g_{a\gamma\gamma} \geq 10^{-14}$ GeV^{-1}. The octave of excluded masses is narrow compared to the full 1 - 30 GHz allowed mass range shown in figure 1.4. However, as mentioned in chapter 1, it is expected that axions would have a mass of about 10^{-5} eV if they provide closure of the universe. The current experiment will continue up to ≈ 5-6 GHz (2.5×10^{-5} eV) where technical realities make the experiment much more difficult and much less sensitive.

It is the fact that the mass of the axion is only very loosely

constrained that makes the search so difficult. In contrast, if the axion is discovered in the study other phenomena and its mass is determined, then a highly sensitive experiment can be made to establish the local presence of axions. But still, the experiment is based on a mixture of theoretical speculation and purely exploratory arguments and the theory which determines the coupling is far from proven. In addition, even if axions exist, they may not compose the dark matter halo of our galaxy or close the universe. These uncertainties dictate moderation in the effort which can be applied toward axion searches. However, this search is the first for such light pseudoscalar particles and the discovery of them would yield a wealth of new information about the early universe, about physics at scales beyond what is achievable in the laboratory, and about most of the mass of the universe. Thus, such searches will always be novel and important.

References

1. Actually, figure 6.1 does not show the limits for constant axion bandwidth. The bandwidth is 200 Hz for 1.09 to 1.22 GHz and 400 Hz for 1.22 to 2.46 Ghz. These are the multiplexer channel bandwidths used when the data were taken.

2. S. De Panfilis, A. C. Melissinos, B. E. Moskowitz, J. T. Rogers, Y. K. Semertzidis, W. Wuensch, H. J. Halama, A. G. Prodell, W. B. Fowler, and F. A. Nezrick, Phys. Rev. Lett. 59, 839 (1987).

Appendix A: Magnet and Cryogenic System

A.1 The Magnet and Insert

The magnet used in this experiment was built in the 1960's[1] and was constructed as a split-pair solenoid with a bore of 8 inches diameter and 16 inch length. The two coils each have approximately 9000 ft of copper stabilized NbTi wire in 2,215 and 2,473 turns (upper and lower coils respectively). The overall dimensions can be seen in figure A.1. The magnet operated with a current of 550 amps and produced a peak field of 6.7 T, which resulted in $B_0 - 5.8$ T [2]. Data was taken for cavities I and II with the magnet in this configuration. Quench detection with this magnet takes advantage of there being two magnet coils in series. The voltage is monitored across each of the coils and if the difference between them exceeds a trip voltage of 2 volts the power supply is shut off. This difference voltage method allows the quench detection circuitry to distinguish between a quench and rapid ramping of the magnet current. It is assumed that the two coils do not quench simultaneously!

In December of 1987, after having taken data with cavities I and II, the two lowest frequency and consequently largest diameter cavities, an insert solenoid was placed inside the bore of the
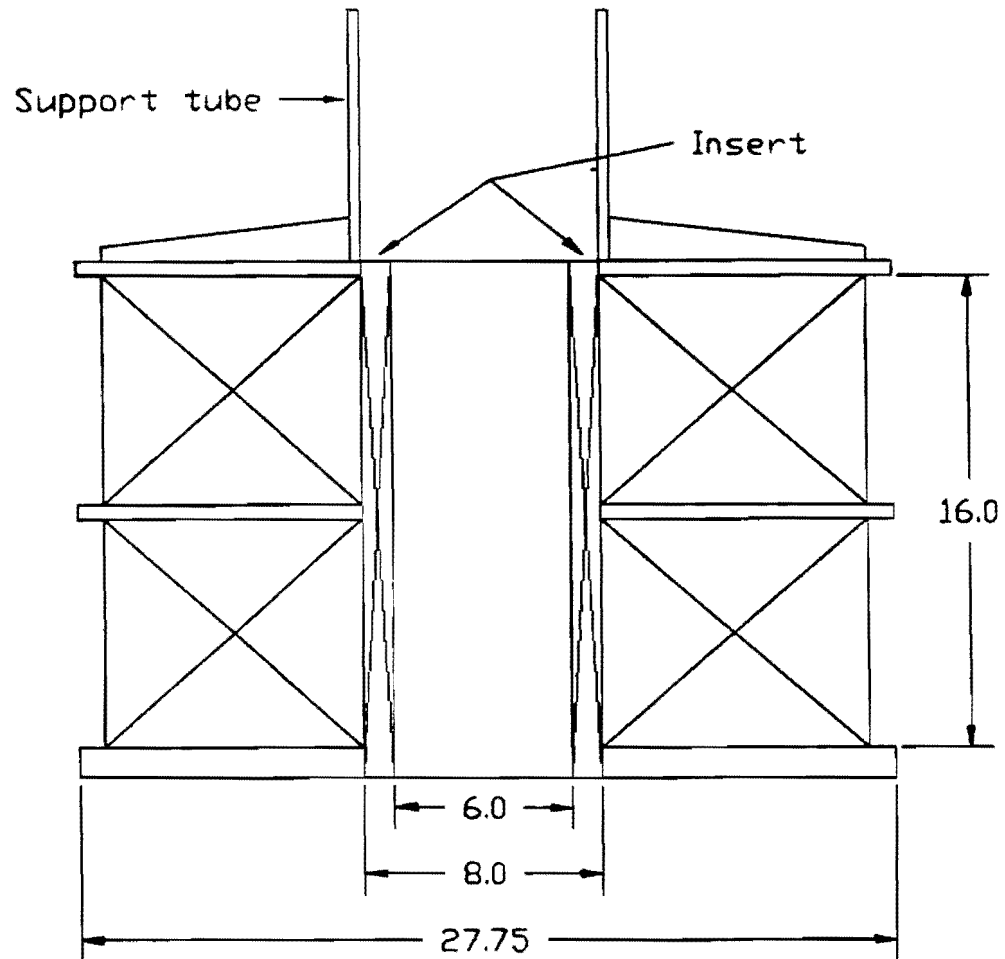
168

**Figure A.1:** A cross sectional view of the Magnet and insert.

original magnet. The insert increases the peak field to 8.5 T and is quite compact, only reducing available diameter of the bore from eight to six inches and is wound from niobium titanium monolith wrapped with kapton. Figure A.2 shows the magnetic field along the central axis of the magnet with the insert for a current of 480 amps[3]. This results in a peak field of 8.5 T and B_0 - 7.6 T. The third coil has been wired in series with the magnet's original two as shown in figure A.3. A pair of diodes have been placed across the insert for protection in the event of a quench. Current from the outer coils flows through the diodes rather than the insert in the event of a quench of the insert. In this way the energy stored in the outer coils is not dumped into the quenching inner coil. The diodes also protect the outer coils in the event that either one of them quenchs.

The magnet is powered by a Sorensen DCR20-1000A power supply and the current through the magnet is monitored by a Holec zero-flux current transformer. Feedback from the Holec is used to adjust the power supply voltage providing active regulation of the current. The power supply is protected from the high inductance load of the magnet by a free wheeling diode as shown in figure A.3. Connected in series with the magnet is a 1.5 × 10^{-3} ohm water cooled resistor which reduces the current-ramp-down time of the > 2 Henry magnet and also facilitates current regulation. The power supply is shut off automatically if a quench is detected by the method mentioned earlier. The quench protection circuitry also opens a large valve

Field vs. Position
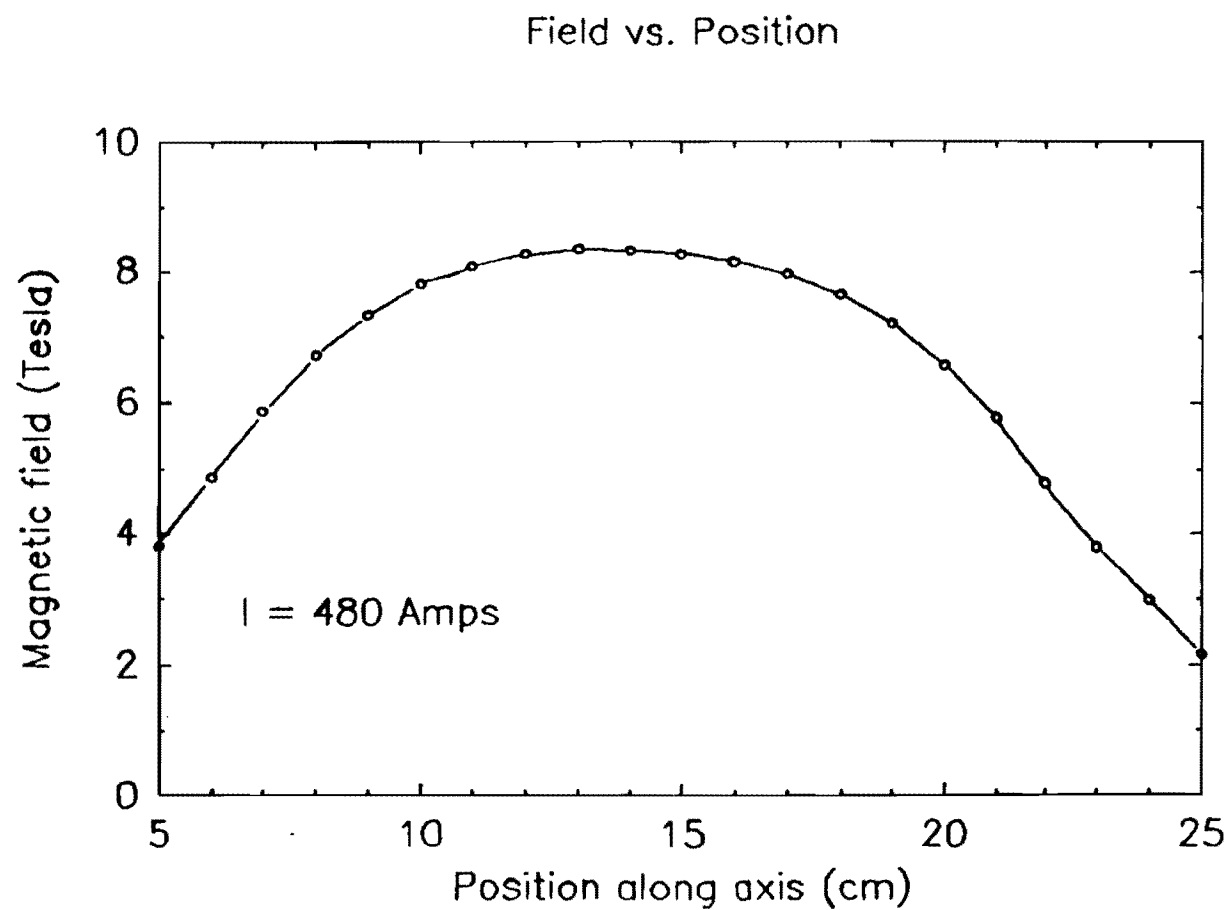
Figure A.2: Calibration of the magnetic field along the central axis of the magnet and insert for 480 amps.

Water cooled resistor

Upper coil

A

Power supply protection diode

Power Supply

Lower coil

Quench protection diodes

Insert

B
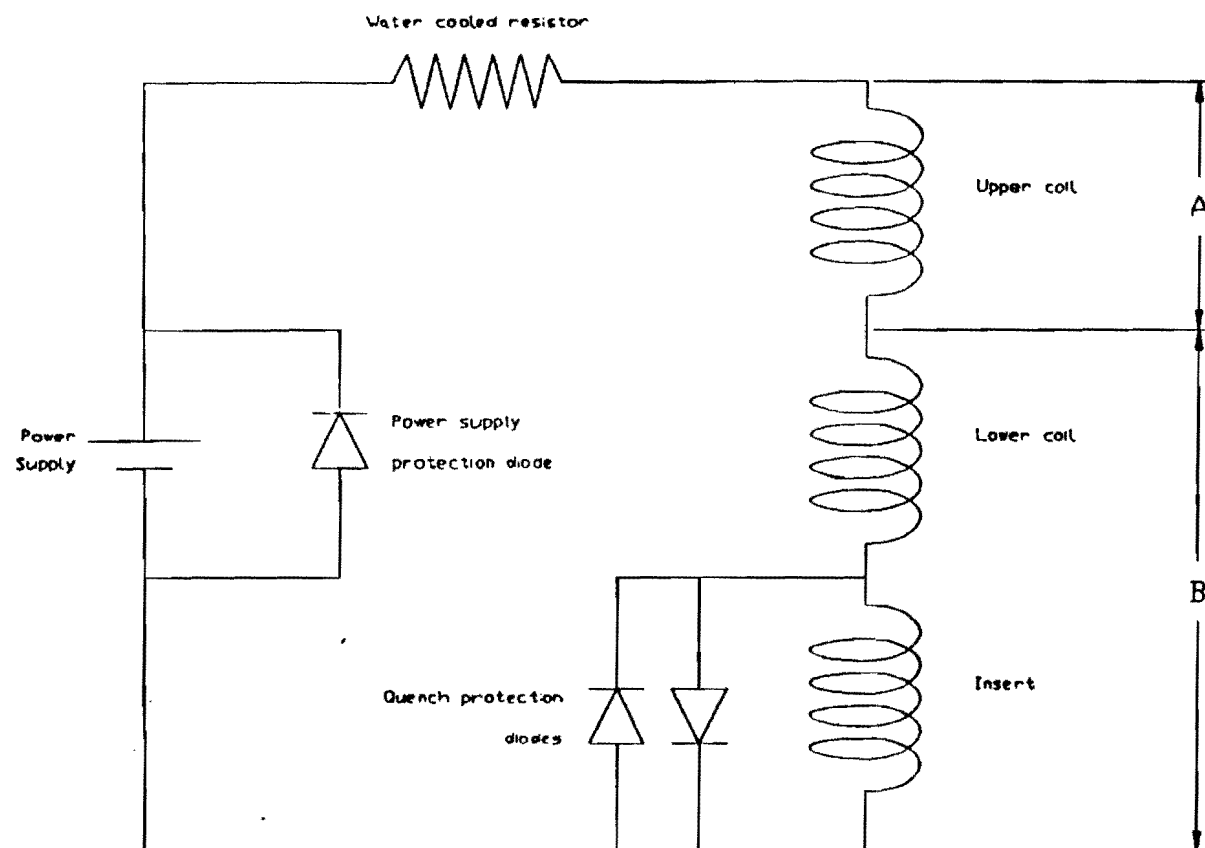
Figure A.3: Schematic of the magnet and power supply system.

on the top of the dewar which allows the large quantity of helium boiloff gas caused by a quench to be captured by the helium recovery system.

A.2 The Dewar

Due to the size of the magnet (a modern magnet of the same field would be smaller) the dewar is rather large, with a total volume of 1252 liters (98 inches long by 31.5 inches diameter). The liquid helium boiloff is directed through a copper radiation shield. In addition, boiloff gas is also directed through gas cooled current leads. The flows through the jacket and current leads are monitored by flow meters and are adjusted to extract the maximum refrigeration capacity from the boiloff gas. This design results in a four to five liter per hour liquid helium boiloff rate, although this changes with the liquid level. The boiloff gas is piped directly to the gas collecting buffer volume of the helium liquification system of the Magnet Test Facility of Brookhaven Laboratory. The liquid helium level must remain above the top of the magnet whenever the magnet is carrying current. In addition, the dewar cannot be filled above the entrance to the gas cooled leads. This restricts the difference between the high and low fill points of the dewar to 36 inches, which corresponds to a contained volume of 450 liters. Figure A.4 shows a graph of liquid helium level vs. time. Helium transfers from portable 500 liter storage dewars are necessary every two and one half days.
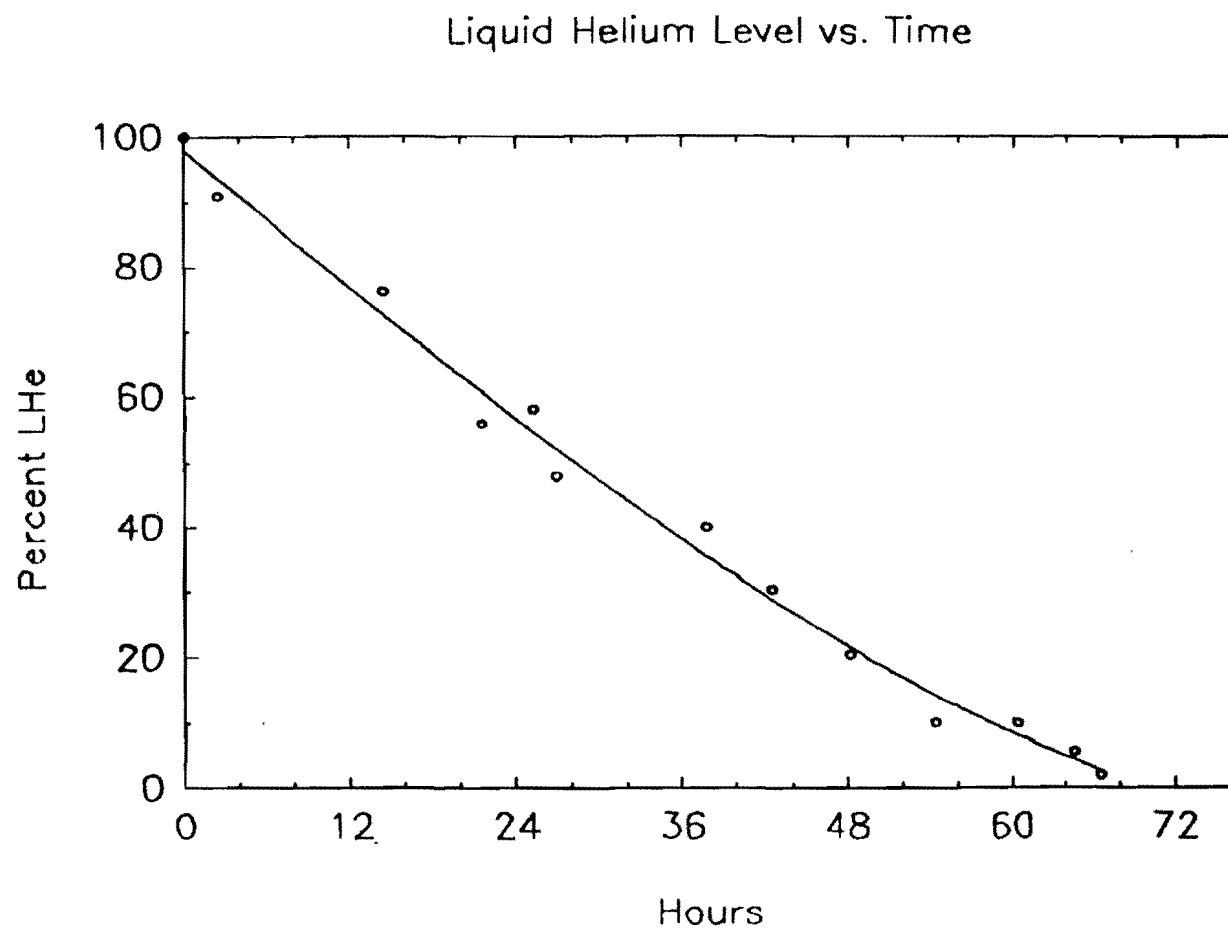
Liquid Helium Level vs. Time

Figure A.4: Liquid helium level in the dewar vs. time.

Liquid helium has a dielectric constant of $\epsilon = 1.0480$ [4]. and depends on the temperature and pressure. Small changes in these quantities produce noticeable shifts in the resonant frequency of the cavity since it is filled with liquid helium. Figure A.5 shows a graph of the change of frequency with pressure. As mentioned earlier, the dewar is directly connected to the helium liquification system. The liquification system serves a number of other users and the pressure of the helium return is subject to pressure fluctuations depending in part on their activities. A pressure regulation system has been installed in order that pressure changes in the buffer volume do not cause excessive pressure changes in the dewar and consequent frequency shifts of the cavity. The system is completely pneumatic and opens and closes the jacket flow to maintain the dewar at a fixed pressure of about 4 psi (although this value is adjustable). The return system has typically a pressure of 1.5 psi.

% Frequency change vs. pressure
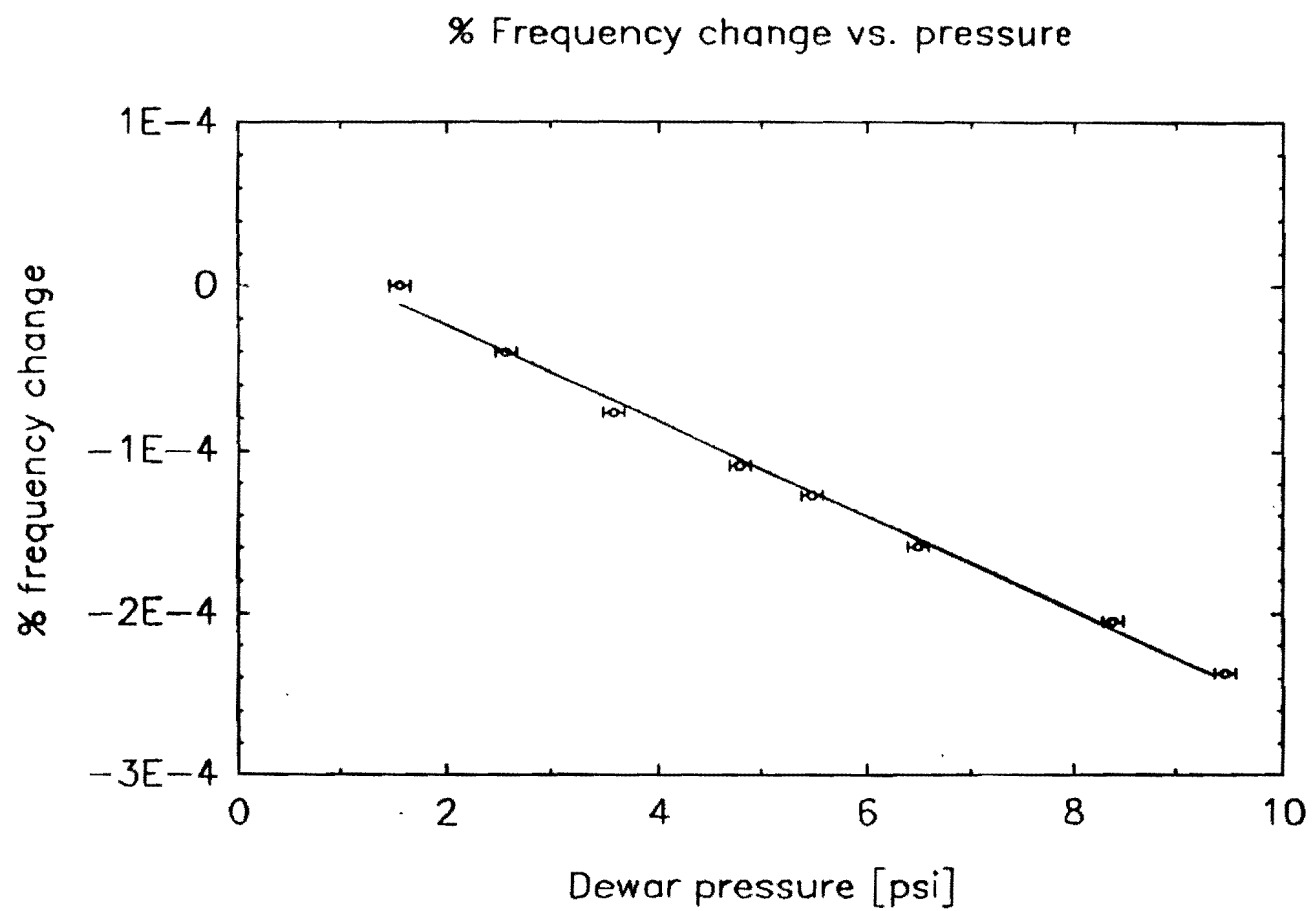
Figure A.5: Cavity frequency vs. pressure in the dewar for cavity I.

References

1. J. Bamberger, G. Mulholland, A. Prodell, H. Worwetz, and C. Whetstone, Adv. Cryog. Eng. 13, 132 (1967).

2. B_0 is defined in equation 2.11.

3. The magnet with the insert has been run at currents in excess of 500 amps without a quench, however a more conservative 480 amps is used during data taking.

4. J. Jensen, W. Tuttle, R. Stewart, H. Brechna, A. Prodell eds., *Brookhaven National Laboratory Selected Cryogenic Data Notebook*, Brookhaven National Laboratory publication BNL 10200-R (1980).